The Dissertation Committee for Colleen Marie Kaul
certifies that this is the approved version of the following dissertation:

Subfilter Scalar Variance Modeling for Large Eddy Simulation

Committee:

Venkat Raman, Supervisor

Noel T. Clemens

Robert D. Moser

Ofodike A. Ezekoye

Philip L. Varghese

Subfilter Scalar Variance Modeling for Large Eddy Simulation

by

Colleen Marie Kaul, B.S., M.S.E.

Dissertation

Presented to the Faculty of the Graduate School of

The University of Texas at Austin

in Partial Fulfillment

of the Requirements

for the Degree of

Doctor of Philosophy

The University of Texas at Austin

August 2011

Subfilter Scalar Variance Modeling for Large Eddy Simulation

Colleen Marie Kaul, Ph.D.
The University of Texas at Austin, 2011

Supervisor: Venkat Raman

Accurate models for the mixing of fuel and oxidizer at small, unresolved flow length scales are critical to the predictive skill of large eddy simulation (LES) of turbulent combustion. Subfilter scalar variance and subfilter scalar dissipation rate are important parameters in combustion modeling approaches based on a conserved scalar, but are prone to numerical and modeling errors due to the nature of practical LES computations. This work examines the errors incurred in these models using a novel method that couples LES scalar modeling with direct numerical simulation (DNS) of homogeneous isotropic turbulence and offers modeling and numerical techniques to address these errors. In the coupled DNS-LES method, DNS velocity fields are evolved simultaneously with LES scalar fields. The filtered DNS velocities are supplied to the LES scalar equations, instead of solving the LES momentum equations. This removes the effect of errors in the filtered scalar evolution from the scalar modeling analysis. Results obtained using the coupled DNS-LES approach,

which permits detailed study of physics-related and numerical errors in scalar modeling, show that widely used algebraic dynamic models for subfilter scalar variance lack accuracy due to faulty equilibrium modeling assumptions and sensitivity to numerical error. Transport equation models for variance show superior performance, provided that the scalar dissipation rate model coefficient is set appropriately. For this purpose, a new dynamic approach for nonequilibrium modeling of subfilter scalar dissipation rate is developed and validated through a priori tests in an inhomogeneous jet flow and using the coupled DNS-LES method for assessment of numerical error effects. Explicit filtering is assessed as means to control numerical error in LES scalar modeling and the scalar equations are reformulated to account for the explicit filtering technique. Numerical convergence of the mean subfilter scalar variance prediction with increasing grid resolution is demonstrated.

Table of Contents

Chapter 1

Introduction

Large eddy simulation (LES) is a valuable tool for the simulation of turbulent reacting flows. As its name suggests, LES solves for the larger length scales of a turbulent flow while small scales are eliminated through a low-pass filtering operation. Limiting the range of turbulent length scales reduces the computational expense of LES relative to direct numerical simulation (DNS). DNS achieves high accuracy by resolving all turbulent scales and is therefore not feasible for high Reynolds number flows. The success of LES is attributable to the method's ability to characterize the large scale mixing process that cannot be captured in Reynolds average simulations (RAS) of the mean flow equations [1]. Development of LES methods for reacting flows has been largely driven by interest in turbulent combustion applications. As in the past, robust simulation methods are needed to engineer combustion-based systems for high efficiency and reliability. Growing economic and environmental pressures have added emissions reduction and alternative fuel use as important design criteria. Unfortunately, present LES modeling and simulation approaches lack the sensitivity needed to address such concerns with reliable quantitative predictive ability.

A range of combustion modeling approaches are currently available for use with LES, varying in their complexity and sophistication. However, all these models ultimately require a description of small scale mixing, on which the combustion process critically depends. Because only the large scale flow is resolved in LES, parameters characterizing mixing below the filter cut-off must be modeled. In general, the predictions of combustion models are highly sensitive to errors in these parameters.

Two types of errors occur in LES computations. The first type of error is modeling error in closures for subfilter terms. Modeling error can be further broken down into a deterministic component related to faulty assumptions about flow physics and a stochastic component owing to the random nature of turbulence. The second type of error is numerical error due to the limited resolution of the computational meshes used in LES. In most LES simulations, including all known LES of turbulent combustion, the coarseness of the numerical discretization takes the place of an explicit filtering operation. This approach to filtering will be referred to as grid-based filtering and is a distinguishing feature of the prevailing practical LES methodology.

This work examines modeling and numerical errors in two small scale mixing parameters, subfilter scalar variance and subfilter scalar dissipation rate, that are fundamental to conserved scalar combustion modeling approaches [2]. Modeling and numerical error are closely interrelated but require different corrective measures and need to be distinguished from each other in analyses of simulation accuracy. A novel coupled DNS-LES approach is developed for

this purpose and used to study how numerical error affects various variance models. From this work, two key findings emerge, indicating two paths for further research. First, the combination of low order numerical schemes and grid-based filtering is shown to result in large numerical error. Explicit filtering is evaluated as a means to reduce this error. Second, closures for the subfilter scalar dissipation rate are found to have a high level of modeling error. A new dynamic model for subfilter scalar dissipation rate is formulated and tested to address this shortfall.

Before presenting these research developments in detail, the relevant background material is reviewed, beginning with a description of LES and the types of errors affecting it. Next, the basic concepts of conserved scalar combustion models are explained and linked to LES through presumed pdf methods. Finally, current models for subfilter scalar variance and subfilter scalar dissipation rate are discussed.

1.1 Fundamentals of Large Eddy Simulation

Large eddy simulation explicitly evolves large scale turbulent motions while the effects of small scale motions on the large scales are approximated using models. Removal of the small scales is accomplished by a filtering operation, which can be written as

$$\overline{\psi}(\mathbf{x},t) = \int \psi(\mathbf{x}',t)\mathbf{G}(\mathbf{x}',\mathbf{x})d\mathbf{x}', \tag{1.1}$$

where $\overline{\psi}(\mathbf{x}, t)$ is the filtered field obtained from the true field $\psi(\mathbf{x}, t)$, and $\mathbf{G}$ is the three-dimensional filter kernel [3]. Examples of filter kernels include the box filter, the Gaussian filter, and the sharp spectral filter [3, 4]. In addition to the shape of the filter, the filtering operation is defined using a characteristic length scale Δ, called the filterwidth. Length scales below the filterwidth are either eliminated or significantly attenuated through the application of the filter,

The filtering operation can be applied to each term in the Navier-Stokes, continuity, and scalar transport equations. Under the assumption that filtering and differentiation commute, a set of equations in the filtered flow variables is obtained. These equations are similar in form to the Reynolds-averaged flow equations and, like them, contain unclosed terms that are called subfilter (or subgrid, under grid-based filtering) terms in LES. In RAS, unclosed terms are higher order statistics of the flow. The goal in modeling these terms is well defined and the relationship between an exact RAS solution and the actual flow is clear. Filtering differs from Reynolds averaging as it merely smooths an instantaneous turbulent field without removing its randomness.

Not only is the filtering operation used to derive the LES equations dissimilar from Reynolds averaging used to obtain the mean flow equations, but the discretized forms of the LES equations that are used in simulations must be interpreted differently than their continuous counterparts. As mentioned above, most LES use grid-based filtering. The coarseness of the numerical discretization acts to eliminate small length scales from the flow solution without

any explicitly defined filtering operation being applied and the filterwidth Δ is assumed to be equal to the grid spacing h. Grid-based filtering has important consequences for the level of numerical error affecting LES solutions. It also plays a role in the interpretation of LES subfilter modeling. Because grid-based filtering is a non-invertible filtering operation, information about the subfilter scales of the flow is irretrievably lost through its application. A given filtered field can only be associated with a probability distribution of small scale states [5]. Thus, the unclosed terms in the LES equations are random quantities also, even given a particular filtered field. As a consequence, the goal of modeling and the relationship between an LES solution and actual turbulence become matters of some question [6].

1.1.1 Modeling Error

Since the subfilter modeling problem is not well defined, it is also difficult to precisely define modeling error and a variety of error measures and model comparison approaches have been used. It is worth noting that more systematic formulations of LES have been advanced, such as optimal LES [5] and LES using self-conditioned fields [7]. Both approaches use conditional averaging to redefine LES, thereby imparting desirable properties to the resulting solutions. Unclosed terms also appear as conditional statistics, which in theory clarifies the information that a model should represent. However, the conditioning variables for these statistics are entire fields, making their actual computation impracticable. While these alternative LES formulations are

interesting concepts, they are not practical simulation methods for complex turbulent reacting flows. Therefore, the current work follows more conventional notions of LES modeling and performs model comparisons using simpler statistics that can be readily estimated.

A useful measure of model accuracy is provided by the idea of optimal estimators [8–10]. It is well known in estimation theory [11] that the conditional mean $\langle X|Y = y\rangle$ is the minimum mean square error predictor of the value x of the random variable X given only the observed value y of the random variable Y. The magnitude of the mean square error, however, depends on the choice of the conditioning variable. For model evaluation purposes, relevant choices of conditioning variable are the input variables to subfilter models. Note that in future notation a random variable and its observed value will be indicated by the same symbol.

As an example, suppose we want to compare two models for a quantity a. Model 1 predicts a as a function of one set of variables that can be regarded as a single dimensionally consistent model input variable b, i.e. $a = M_1(b)$. Similarly, Model 2 predicts a as a function of some other input variable c, i.e. $a = M_2(c)$. Abstracting a bit from the turbulence modeling case, simply assume we have a large number of independent, identically distributed samples of these values. Each model has two aspects, one being the input variable and the other, the model's functional form. To assess the models we consider the

errors

$$\varepsilon_{i,1} = \left\langle (a - \langle a|b\rangle)^2 \right\rangle \tag{1.2}$$

$$\varepsilon_{i,2} = \left\langle (a - \langle a|c\rangle)^2 \right\rangle \tag{1.3}$$

$$\varepsilon_{t,1} = \left\langle (a - M_1(b))^2 \right\rangle \tag{1.4}$$

$$\varepsilon_{t,2} = \left\langle (a - M_2(c))^2 \right\rangle \tag{1.5}$$

Eqs. 1.2 and 1.3 give the irreducible error of the models related to the random variation of a that cannot be explained by the variation of b or c. Lower irreducible error indicates a stronger relationship between the model input variable and the quantity to be predicted. Eqs. 1.4 and 1.5 are the total errors of the models and include the irreducible error and the error due to the functional form of the model. Fig. 1.1 shows how a model's total error can be high although the irreducible error of its input variable is low when there is a discrepancy between the shape of the conditional mean and the functional relationship postulated by the model. It should be mentioned that the statistics of subfilter quantities generally depend on the specific flow configuration and filter being considered and can exhibit spatial variation in inhomogeneous flows.

1.1.2 Numerical Error

Solutions to the LES equations are well known to be sensitive to the choice of numerical scheme and the precise formulation of the discretized equations. For example, analytically equivalent expressions for the convective terms

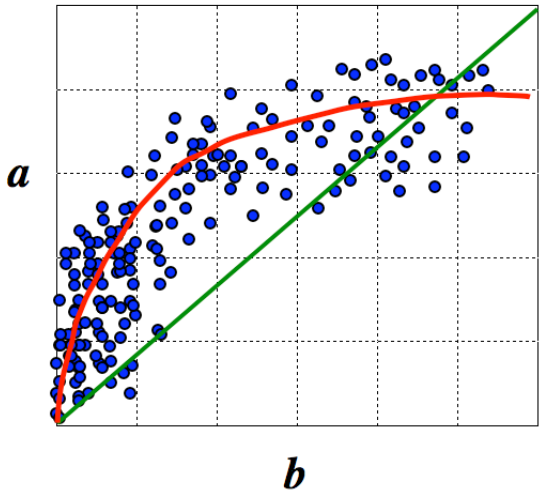

Figure 1.1: Schematic illustrating difference between the conditional mean $\langle a|b\rangle$ (red) and a model $a = M(b)$ (green), shown as linear relationship between a and b, superimposed on a scatter plot of realizations of a and b.

in the incompressible momentum equations yield far from equivalent results when evaluated by finite differences [12–14]. When grid-based filtering is used, the LES solution is inherently dependent on the computational grid and its numerical error cannot be effectively controlled by grid refinement until the DNS limit is reached. Before that level of refinement, any decrease of grid spacing introduces shorter length scales into the solution [12]. For grid-filtered LES, the value of grid refinement lies chiefly in reducing the magnitude of subfilter terms and hence lessening the effect of model errors.

Grid refinement reduces numerical error when explicit filtering is used to hold the filterwidth constant as the spatial resolution is increased. Explicit filtering is discussed in Ch. 4. The greater numerical accuracy provided by

explicit filtering is accompanied by significantly higher numerical expense for a fixed filterwidth, which has limited the popularity of this approach to LES in the past.

The other option for reducing numerical error is to perform LES using high order of accuracy finite different schemes. The range of length scales in an LES solution corresponds in the spectral domain to modes of varying wavenumber. This suggests that the effects of these schemes can best be understood through their modified wavenumber representation.

The ability of a finite difference scheme to approximate the analytical derivative of a mode ϕ with wavenumber k, $\phi = e^{ikx}$ is expressed by the scheme's modified wavenumber $g(k)$. The exact value of the first derivative of ϕ is given by $d\phi/dx = ike^{ikx}$, but a finite difference scheme gives the value

$$\frac{d\phi}{dx}^{\mathrm{fd}} = ig(k)e^{ikx}. \tag{1.6}$$

Clearly, the approximation becomes more accurate as the value of $g(k)$ approaches that of k [15].

Fig. 1.2 shows the modified wavenumbers of second and fourth order central schemes and a sixth order Padé scheme [13]. An ideal scheme would fall along the diagonal. For grid-filtered LES, $k_{\max}h \approx \pi$. Therefore, using a more accurate scheme improves the estimation of the derivative over a range of intermediate wavenumbers, but all schemes considered here fail to numerically resolve scales just above the filter scale. Because many variance models are

explicitly or implicitly highly dependent on these scales, numerical error is an important aspect of variance prediction.

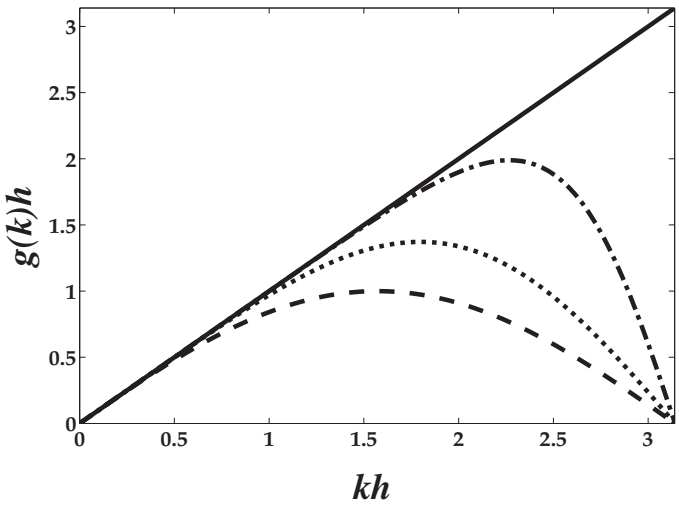

Figure 1.2: Modified wavenumbers of second (- - -) and fourth (·····) order central schemes and a sixth order central Padé (-·-·) scheme.

1.2 Conserved Scalar Approaches for LES

In conserved scalar models, a non-reactive scalar called the mixture fraction relates fuel and oxidizer mass fractions at a point in the flow. For example, a simple definition of mixture fraction, denoted by Z, for a two-feed system is

$$Z = \frac{\nu Y_F - Y_{O_2} + Y_{O_2,2}}{\nu Y_{F,1} + Y_{O_2,2}}. \tag{1.7}$$

The symbol ν represents the stoichiometric mass ratio of oxygen to fuel. The mass fraction of fuel in the fuel stream is $Y_{F,1}$ and $Y_{O_2,2}$ is the mass fraction of oxygen in the oxidizer stream [16].

If binary diffusion fluxes with equal diffusivities for all species are assumed, a conservation equation for the mixture fraction in an incompressible flow can be written as

$$\frac{\partial Z}{\partial t} + \frac{\partial u_i Z}{\partial x_i} = \frac{\partial}{\partial x_i}\left[D\frac{\partial Z}{\partial x_i}\right]. \tag{1.8}$$

where D denotes the common value of molecular diffusivity [17]. An incompressible flow approximation is only valid in cases with low heat release, such as occurs for dilute mixtures [18]. This work is focused on modeling of mixing, apart from reaction, so a variable density formulation is not required. Additionally, this study uses a pseudospectral simulation method that is only applicable to constant density flows. For the same reason, incompressible flow equations have even been used to study reacting flows when the phenomena of interest are expected to be dominated by flow dynamics rather than heat release effects [19].

The mixture fraction is valuable because it can be linked to the thermochemical state of the flow by a combustion model. Different modeling assumptions lead to different model forms. The simplest models assume infinitely fast reactions and the mapping based on Z is pointwise. More realistically, the reactions are treated as finite-rate, so also they depend on the instantaneous

scalar dissipation rate,

$$\chi_Z = 2D\frac{\partial Z}{\partial x_i}\frac{\partial Z}{\partial x_i} \tag{1.9}$$

However, the chemical time scale remains short relative to the turbulence time scale, so the reaction zone is thin and can be treated as lying within a Kolmogorov-scale eddy. Thus the flow immediately surrounding the flame surface is laminar. This representation of turbulent combustion is known as the laminar flamelet model [20, 21]. It allows the derivation of flamelet equations, which are partial differential equations for temperature T and species mass fractions Y_i. In these equations, χ_Z appears as a solution parameter and Z has the role of a spatial coordinate normal to the reaction surface. Steady state solutions to the flamelet equations can be pre-tabulated apart from any particular flow scenario by prescribing various values of χ_Z. Representative solutions are depicted in Fig. 1.3. Given a detailed mixture fraction field (i.e., a DNS solution), χ_Z can be computed and values of T and Y_i found from the look-up table. Knowledge of Z thereby allows the entire composition field to be constructed.

LES provides a filtered mixture fraction field $\overline{Z}(\mathbf{x}, t)$ rather than the full mixture fraction field $Z(\mathbf{x}, t)$. By applying the filtering operation of Eq. 1.1 to Eq. 1.8, a transport equation for $\overline{Z}$ can be developed. This can be written as

$$\frac{\partial \overline{Z}}{\partial t} + \frac{\partial \overline{u_i}\overline{Z}}{\partial x_i} = \frac{\partial}{\partial x_i}\left[(D + D_T)\frac{\partial \overline{Z}}{\partial x_i}\right] \tag{1.10}$$

with the filtered velocity denoted by $\overline{u_i}$ and the turbulent diffusivity (used to close the subfilter scalar flux) by D_T. The turbulent diffusivity is modeled

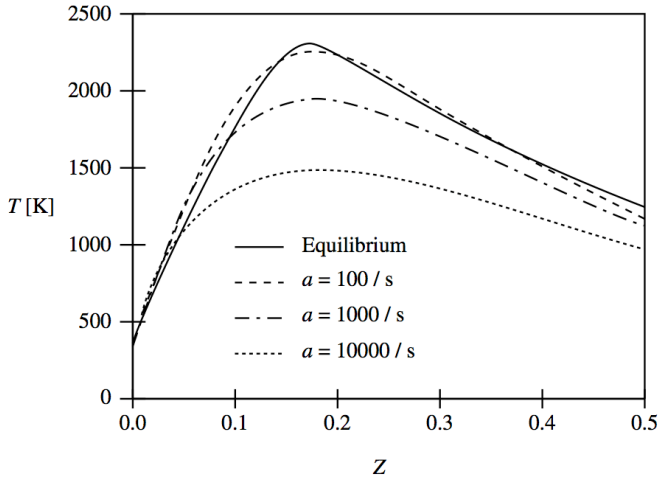

(a)

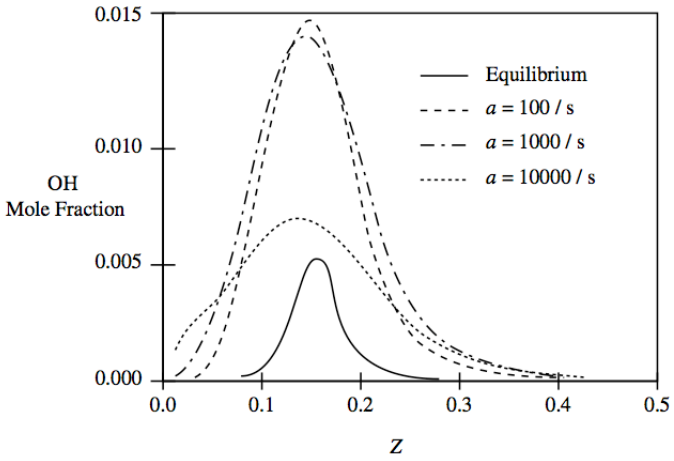

(b)

Figure 1.3: Comparison of flamelet solution at three different strain rates a (which is linearly related to χ_Z) to equilibrium chemistry results for (**a**) temperature and (**b**) OH mole fraction of H_2 in air flame. Reproduced from [17].

using the filterwidth Δ and characteristic strain rate $|\overline{S}| = \left(2\overline{S}_{ij}\overline{S}_{ij}\right)^{1/2}$ as

$$D_T = \mathcal{C}_Z \Delta^2 |\overline{S}|. \tag{1.11}$$

The coefficient $\mathcal{C}_Z$ is determined dynamically [22].

Because the mixture fraction transport equation contains no chemical source terms, its filtered version, Eq. 1.10, is easily handled in the LES framework. However, the filtered mixture fraction fields evolved by LES provide no information on the extent of small scale fuel-oxidizer mixing, which is required for reaction to occur. Further modeling is needed to characterize values of the mixture fraction at subfilter scales. In one-point statistical closures for the mixture fraction, the subfilter probability density function (pdf) is presumed to be a beta distribution that is parameterized by the filtered mixture fraction and subfilter mixture fraction variance.

The subfilter variance Z_v is defined as

$$Z_v(\mathbf{x}, t) = \int \left(Z(\mathbf{x}', t) - \overline{Z}(\mathbf{x}, t)\right)^2 \mathbf{G}(\mathbf{x}', \mathbf{x}) d\mathbf{x}' = \overline{Z^2}(\mathbf{x}, t) - \overline{Z}^2(\mathbf{x}, t). \tag{1.12}$$

It can be shown that Z_v is the variance, in the usual statistical sense, of the filtered density function (FDF) [23], which has the properties of a probability density function [24]. However, the filtered density function is a property of a particular turbulence realization [1], so Z_v is still a random quantity in LES. The appearance of the second moment of the FDF, $\overline{Z^2}$, makes the variance unclosed.

The presumed pdf of Z is completed once a model for the variance is supplied. When combustion is modeled using the steady laminar flamelet approximation, a model for the filtered scalar dissipation rate and its subfilter distribution are also required, because they depend on mixture fraction gradient values which cannot be inferred from a one-point pdf. Typically, subfilter variability of $\overline{\chi}_Z$ is neglected [25, 26] . Filtered species and temperature values can be determined from the relationship

$$\overline{Y_i}\left(\mathbf{x},t\right)=\int\int M\left(Z,\chi_Z\right)P_Z(\overline{Z}\left(\mathbf{x},t\right),Z_v\left(\mathbf{x},t\right))\delta(\chi_Z-\overline{\chi}_Z\left(\mathbf{x},t\right))dZd\chi_Z \tag{1.13}$$

where M represents the flamelet solution. This information can be retrieved at LES run-time from precomputed look-up tables indexed by values of $\overline{Z}$, Z_v, and $\overline{\chi}_Z$ [25].

Although the mixture fraction-based approach is not valid in all turbulent combustion scenarios, it has been widely used due to its relative simplicity and has been found to yield fairly satisfactory results in flames without signficant extinction [19]. Numerous studies, employing a variety of approaches, have sought to test the suitability of the beta pdf description of subgrid scale mixing, since it cannot be justified by rigorous theoretical arguments. For example, empirical subfilter pdfs determined using temperature measurements in a nonreacting jet were found to exhibit behavior essentially consistent with the beta pdf assumption [27]. In another study involving a priori tests on DNS of a reacting jet, the beta subfilter closure halved the error in predicting a filtered reaction rate proxy, $\overline{g}\left(Z\right)$, over the no model case $g\left(\overline{Z}\right)$ [28]. More

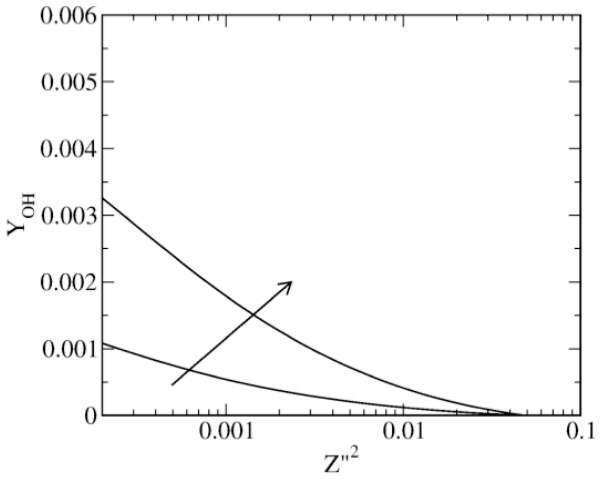

Figure 1.4: Mass fraction of OH as a function of Z_v (here denoted by $\widetilde{Z''^2}$ for given $\overline{Z}$ at high (upper curve) and low (lower curve) scalar dissipation rates for a methane-hydrogen flame in air. Reproduced from Ref. 29.

recently, the optimal estimator concept was used to show that the error associated with the beta pdf assumption compares favorably with the minimum error of any subfilter pdf model based on just two moments [8].

However, the accuracy of the presumed pdf model is contingent on accurate specification of the subfilter variance. This fact is illustrated in Fig. 1.4, which shows how flamelet model predictions of OH mass fraction vary with Z_v for a single value of Z at both high and low values of χ_Z. Noting that variance is plotted on a logarithmic scale, it is clear that small changes in Z_v can lead to large errors in the predicted thermochemistry, especially for minor species like the OH radical [29].

1.3 Description of Variance Models

The subfilter beta pdf closure was proposed in analogy with a well-established methodology in Reynolds-averaged simulations, but it was realized early on that LES allows a broader array of variance modeling approaches, such as models based on scale similarity arguments [30], which are not applicable in RAS. The problem of variance closure was sidestepped by using experimental or DNS data in some initial applications of the presumed pdf method to equilibrium chemistry [30] and flamelet models [25, 31], but other early studies dealt directly with the variance modeling issue [32, 33] and new models were proposed which remain widely used [24, 34].

Currently, subfilter variance modeling follows two basic lines of approach. The first uses scaling assumptions to obtain algebraic expressions for the variance [34]. This category includes variants of the widely-used dynamic model, which relates the variance to the magnitude of filtered scalar gradients. The second approach requires solution of an additional scalar transport equation [24]. While models in this category can account for the transport of subfilter variance at resolved scales, the equations contain dissipation terms that must be closed.

A transport equation for the variance can be derived by analytically manipulating the transport equations for Z (Eq. 1.8) and $\overline{Z}$ (Eq. 1.10) to develop equations for $\overline{Z^2}$ and $\overline{Z}^2$. Then, using Eq. 1.12, the variance transport

equation (VTE) follows from

$$\frac{dZ_v}{dt} = \frac{d\left(\overline{Z^2} - \overline{Z}^2\right)}{dt} = \frac{d\overline{Z^2}}{dt} - \frac{d\overline{Z}^2}{dt} \tag{1.14}$$

After introducing eddy diffusivity models for the scalar flux terms, the LES VTE can be written as [24]

$$\frac{\partial Z_v}{\partial t} + \frac{\partial \overline{u_i} Z_v}{\partial x_i} = \frac{\partial}{\partial x_i}\left[\left(D + D_T\right)\frac{\partial Z_v}{\partial x_i}\right] + \mathcal{P} - \bar{\epsilon}_Z \tag{1.15}$$

where $\mathcal{P}$ and $\bar{\epsilon}_Z$ represent, respectively, production and dissipation of variance. In exact form, the production term is given by

$$\mathcal{P}_{\text{exact}} = 2\left(\overline{u_i}\overline{Z} - \overline{u_i Z}\right)\frac{\partial \overline{Z}}{\partial x_i} \tag{1.16}$$

which, again using an eddy diffusivity closure for the subfilter scalar flux, becomes

$$\mathcal{P} = 2D_T \frac{\partial \overline{Z}}{\partial x_i}\frac{\partial \overline{Z}}{\partial x_i} \tag{1.17}$$

The resulting form of the production model is undesirable from a numerical perspective because it relies on the magnitude of the filtered scalar gradient, which may not be computed accurately by finite difference methods.

The remaining modeling issue for the VTE is the subfilter dissipation rate $\bar{\epsilon}_Z$,

$$\bar{\epsilon}_{Z,\text{exact}} = 2D\overline{\frac{\partial Z}{\partial x_i}\frac{\partial Z}{\partial x_i}} - 2D\frac{\partial \overline{Z}}{\partial x_i}\frac{\partial \overline{Z}}{\partial x_i} \tag{1.18}$$

which is unclosed due to the first term on the right hand side. This quantity, the filtered scalar dissipation $\overline{\chi}_Z$, was mentioned previously in Sec. 1.2 in the

context of flamelet modeling. A common form of closure for $\bar{\epsilon}_Z$ is

$$\bar{\epsilon}_Z = \mathcal{C}_\tau \frac{Z_v}{\tau_Z} \tag{1.19}$$

where τ_Z is a scalar mixing time scale and $\mathcal{C}_\tau$ is a model coefficient. Several expressions for this time scale are available. It should be noted that in some modeling approaches, a mechanical time scale τ is used and the model constant provides the ratio between scalar and mechanical time scales. One option for the scalar time scale, formed from the filterwidth Δ and total diffusivity as

$$\tau_Z = \frac{\Delta^2}{D + D_T} \tag{1.20}$$

is widely used in the LES/FDF approach [35–37]. The optimal value for $\mathcal{C}_\tau$ depends on the flow being simulated and the location of the filter cut-off in the scalar energy spectrum and is therefore typically unknown a priori.

Together, the modeling challenge posed by $\bar{\epsilon}_Z$ and the numerical difficulties associated with $\mathcal{P}$ are the major issues in solving the VTE. The latter obstacle can avoided by returning to Eq. 1.14 and noting that it suffices to solve a transport equation for $\overline{Z^2}$,

$$\frac{\partial \overline{Z^2}}{\partial t} + \frac{\partial \overline{u_i} \overline{Z^2}}{\partial x_i} = \frac{\partial}{\partial x_i} \left[(D + D_T) \frac{\partial \overline{Z^2}}{\partial x_i} \right] - \overline{\chi}_Z \tag{1.21}$$

then use Eq. 1.12 to calculate the subfilter variance. This modeling approach will be referred to as the second moment equation (STE) model. Closure of $\overline{\chi}_Z$ remains a stumbling block for the STE as well as the VTE. Here $\overline{\chi}_Z$ will be modeled by rearranging the model for $\bar{\epsilon}_Z$ to yield

$$\overline{\chi}_Z = \mathcal{C}_\tau \frac{Z_v}{\tau_Z} + 2D \frac{\partial \overline{Z}}{\partial x_i} \frac{\partial \overline{Z}}{\partial x_i} \tag{1.22}$$

with the same choices for τ_Z and $\mathcal{C}_\tau$ available.

A class of algebraic models can be developed from the VTE by assuming that, on average, the production and dissipation of variance are equal. This approximation is usually referred to as the local equilibrium assumption [34]. The posited equivalence can, at best, hold only in a mean sense since both production and dissipation are random fields.

Equating the closures introduced above for $\overline{\epsilon}_Z$ (Eqs. 1.19 and 1.20) and $\mathcal{P}$ (Eq. 1.17) under the local equilibrium assumption and solving for Z_v gives

$$Z_v = \mathcal{C}_v \Delta^2 \frac{\partial \overline{Z}}{\partial x_i} \frac{\partial \overline{Z}}{\partial x_i} \tag{1.23}$$

where $\mathcal{C}_v$ is a model coefficient. Dynamic modeling procedures [38] are usually used to determine $\mathcal{C}_v$. A common feature of these approaches is the use of a second filtering operation at a test filterwidth $\widehat{\Delta} > \Delta$ to isolate the smallest length scales of the filtered scalar field, followed by an assumed similarity between those scales and the subfilter scales. The first dynamic procedure to be developed for variance modeling determined $\mathcal{C}_v$ as a ratio between a Leonard term, denoted $\mathcal{L}_v$, and a gradient-based term $\mathcal{M}_v$ [34]. To avoid large local fluctuations, the coefficient is typically calculated using some averaging procedure suitable for the particular flow configuration. Letting $\widehat{(\cdot)}$ denote a test filtered variable and $\langle \cdot \rangle$ indicate an averaged quantity, the coefficient estimation procedure for the classic dynamic model (CDM) can be written in full as

$$\mathcal{L}_v = \widehat{\overline{Z}^2} - \widehat{\overline{Z}}^2 \tag{1.24}$$

$$\mathcal{M}_{v,\mathrm{CDM}} = \widehat{\Delta}^2 \frac{\partial \widehat{\overline{Z}}}{\partial x_i} \frac{\partial \widehat{\overline{Z}}}{\partial x_i} - \Delta^2 \widehat{\frac{\partial \overline{Z}}{\partial x_i} \frac{\partial \overline{Z}}{\partial x_i}} \tag{1.25}$$

$$\mathcal{C}_v = \frac{\langle \mathcal{L}_v \mathcal{M}_v \rangle}{\langle \mathcal{M}_v \mathcal{M}_v \rangle} \tag{1.26}$$

For the isotropic flow that is considered in this work, a volume average over the entire computational domain is appropriate. Thus, a single value of $\mathcal{C}_v$ is predicted at each time step.

Recently, Balarac *et al.* [9] proposed a modification to the $\mathcal{M}_v$ term of the CDM closure based on a Taylor series expansion of the Leonard term. In this alternative model (henceforth, BPR model) only the first term of $\mathcal{M}_{\sqsubseteq,\mathrm{CDM}}$ is retained, that is

$$\mathcal{M}_{v,\mathrm{BPR}} = \widehat{\Delta}^2 \frac{\partial \widehat{\overline{Z}}}{\partial x_i} \frac{\partial \widehat{\overline{Z}}}{\partial x_i} \tag{1.27}$$

Despite the availability of other algebraic variance models [30], dynamic models are preferred in combustion modeling because they eliminate the need to predetermine a model coefficient and perform well in a priori (DNS-based) tests [28, 34]. However, a weakness of the coefficient estimation procedure is its reliance on the highest wavenumber components of the filtered scalar field, which are most affected by finite difference error. Additionally, the gradient-based scaling law (Eq. 1.23) has the same numerical shortcoming as the production model from which it originates. On the other hand, the advantages of the VTE and STE models in accounting for the transport of variance on the large scales are countered by the difficulties of modeling dissipation terms

and accurately evolving the model equations. These challenges are examined more deeply in the following chapters, which present results from a priori and a posteriori (LES-based) tests of the variance models just described.

Chapter 2

A Priori Analysis of Variance Modeling Errors

The a posteriori model tests which are the major focus of this work form the sequel to a set of a priori tests using data from pseudospectral DNS of homogeneous isotropic turbulence (HIT) with $\mathrm{Re}_\lambda = 135$. These results are also reported in Ref. 39. A priori tests are attractive for several reasons. Prominent among these is the fact that, once a suitable DNS database has been generated, additional models can be evaluated at a range of filterwidths with low marginal cost. Furthermore, a priori tests allow direct comparison between exact subfilter quantities computed from the DNS data with subfilter model predictions, providing insight into the ways that subfilter modeling assumptions depart from the realities of small-scale turbulence. However, a priori tests have some significant limitations, as described in Sec. 2.3, making a posteriori testing an indispensable step in model validation. The coupled DNS-LES method, presented in Ch. 3 was developed to combine valuable features of a priori and a posteriori analysis methods.

These a priori tests focused on the effects of numerical error on variance prediction for various model model forms computed over a range of filterwidths, Finite difference evaluation of derivatives was emulated within the

pseudospectral computational framework through the modified wavenumber representation of second order central (C2), fourth order central (C4) and sixth order Padé (P6) schemes [13] and compared to model evaluations using the true wavenumber as well as to exact values of subfilter quantities.

2.1 Dynamic Models

The most overt source of numerical error in algebraic dynamic models for subfilter scalar variance is the evaluation of the gradient term in Eq. 1.23. It is well known that finite difference approximations grossly underpredict the gradients in a turbulent flow. This suggests that the dynamic model underpredicts the variance. However, the dynamic procedure used to compute the model coefficient also incurs numerical errors. These errors lead to an overprediction of the model coefficient relative to the value determined by exact evaluation of the dynamic closure. Fig. 2.1 shows the original and modified dynamic model coefficients evaluated from DNS using the three different finite difference approximations plotted against the filterwidth nondimensionalized by the Kolmogorov scale, Δ/η. It can be seen that the second order central scheme, which is the least accurate of the schemes, predicts the highest model coefficient for all filter sizes considered. This overprediction partially offsets the error in the gradient estimation, thereby reducing the errors in the prediction of variance (Fig. 2.2). It should be noticed that for the original dynamic model the use of finite differences actually changes the trends exhibited by the coefficient, while the effect on the modified dynamic model is limited to a

scaling of the coefficient value. In a priori tests, a common measure of model error is the mean square error [9, 28], which is defined here as

$$\text{error} = \frac{\left\langle \left(Z_v^{\text{model}} - Z_v^{\text{DNS}} \right)^2 \right\rangle}{\left\langle Z_v^{\text{DNS}} \right\rangle^2} \tag{2.1}$$

that is, it sums the pointwise differences between exact instantaneous variance values and model predictions over the entire flow domain. Over a significant range of filter widths, the presence of numerical error actually improves the predictions of the original dynamic model. The modified dynamic model shows a more consistent behavior, in that increasing the accuracy of the numerical scheme increases the accuracy of the model over the full range of filter widths.

2.2 Transport Equation Models

The second portion of a priori tests focused on transport equation based models. Recall that VTE is derived from the STE by performing product rule manipulations on the transport equation for $\overline{Z}$ to develop an equation for $\overline{Z}^2$. While this approach is analytically valid, it can be numerically problematic. For this discussion, we define the quantities

$$\begin{aligned} P_1 &= 2\overline{Z}\frac{\delta \overline{u}_j \overline{Z}}{\delta x_j} \\ P_2 &= \frac{\delta \overline{u}_j \overline{Z}^2}{\delta x_j} \end{aligned} \tag{2.2}$$

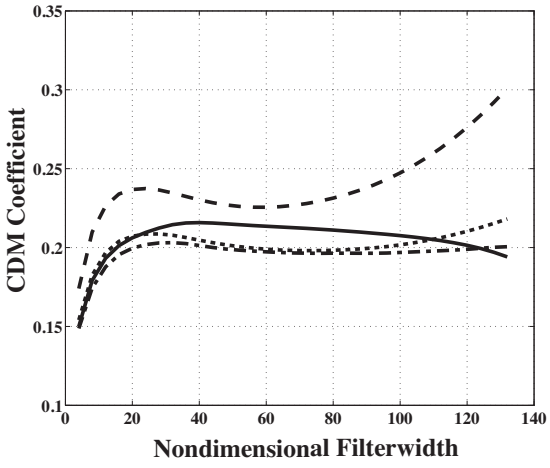

(a)

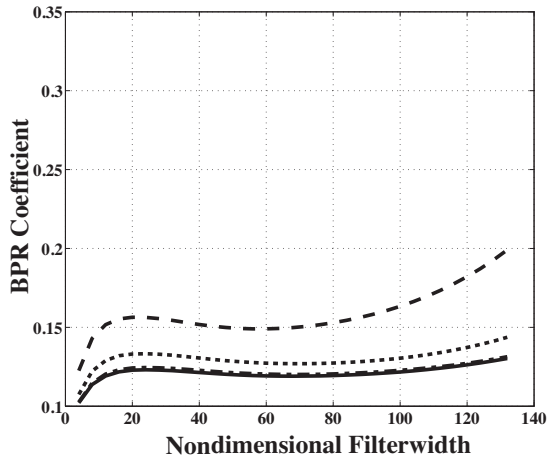

(b)

Figure 2.1: Dynamic model coefficient of (**a**) CDM model (**b**) BPR model, computed using ensemble averaging over the entire domain, as a function of filter size for spectral (———), C2 (- - - -), C4 (·····), and P6 (-·-·) schemes.

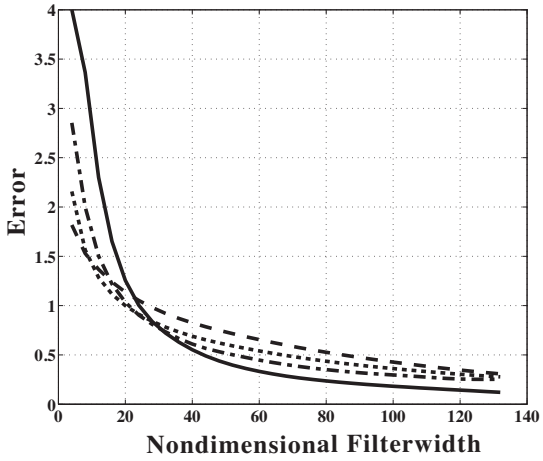

(a)

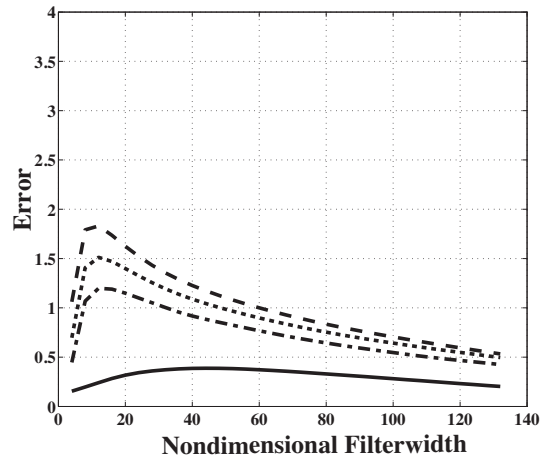

(b)

Figure 2.2: Quadratic error, Eq. 2.1, of (**a**) CDM model (**b**) BPR model for spectral (———), C2 (- - - -), C4 (·····), and P6 (-·-·) schemes.

and

$$Q_1 = 2\overline{Z}\frac{\delta}{\delta x_j}\left[\left(D + D_T\right)\frac{\delta\overline{Z}}{\delta x_j}\right]$$
$$Q_2 = \frac{\delta}{\delta x_j}\left[\left(D + D_T\right)\frac{\delta\overline{Z}^2}{\delta x_j}\right] - 2\left(D + D_T\right)\frac{\delta\overline{Z}}{\delta x_j}\frac{\delta\overline{Z}}{\delta x_j} \tag{2.3}$$

where $\delta/\delta x_j$ refers to numerical approximation of the derivatives. Using these definitions, the transport equations for $2\overline{Z}\delta\overline{Z}/\delta t$ and $\delta\overline{Z}^2/\delta t$ can be written in semi-discretized form as

$$2\overline{Z}\frac{\delta\overline{Z}}{\delta t} = -P_1 + Q_1 \tag{2.4}$$

and

$$\frac{\delta\overline{Z}^2}{\delta t} = -P_2 + Q_2 \tag{2.5}$$

Ideally, $P_1 = P_2$ and $Q_1 = Q_2$. Since it is well known that these discrete representations do not follow the calculus of continuous variables, we at least expect small differences between the two representations when implementing the VTE. Instead, the errors associated with these approximations have a strong bias, as evidenced by the conditional means $\langle P_2|P_1\rangle$ and $\langle Q_2|Q_1\rangle$. For all three schemes considered, the amount of error is quite similar. Fig. 2.3(a) shows that the magnitude of P_1 is always underpredicted by representation in the form P_2. This implies that the large scale redistribution of variance is underpredicted by the VTE model. Turning to the Q terms, it can be seen that the conditional mean $\langle Q_2|Q_1\rangle$ lies above the diagonal, indicating that Q_2 is overpredicted. This finding holds for both a constant or dynamically modeled value of D_T; the latter case is depicted in Fig. 2.3(b). Higher values

of Q_2 lead to higher values of $\overline{Z}^2$ and, consequently, lower values of variance as predicted by the VTE.

2.3 Shortcomings of a Priori Analysis

These results show that standard a priori analysis techniques can be expanded to incorporate some of the effects of numerical error on subfilter modeling, and in particular, on subfilter scalar variance modeling. While such static tests on DNS data are useful in isolating specific sources of error in subfilter variance estimation, they are not necessarily indicative of the errors encountered in LES simulations because they do not account for the interaction of the variance model with an LES-evolved filtered scalar field nor for the persistence of errors across timesteps as occurs in transport equation models. In Chapter 3, the importance of these additional factors is confirmed using an a posteriori approach.

A second reason why a priori tests may lack extensibility to LES results is that a DNS field provides only one sample of the small scale turbulence field that could correspond to a given filtered field. Typically, a priori tests focus on error measurements, such as Eq. 2.1 that are essentially approximations to one-point statistics, and spatial averages over homogeneous directions are used in place of ensemble averages over many distinct DNS realizations. Most methods for estimating one-point statistics assume independent and identically distributed data. While the latter criterion is satisfied by a homogeneous isotropic DNS soluton, the former is not. Both real and simulated turbulence

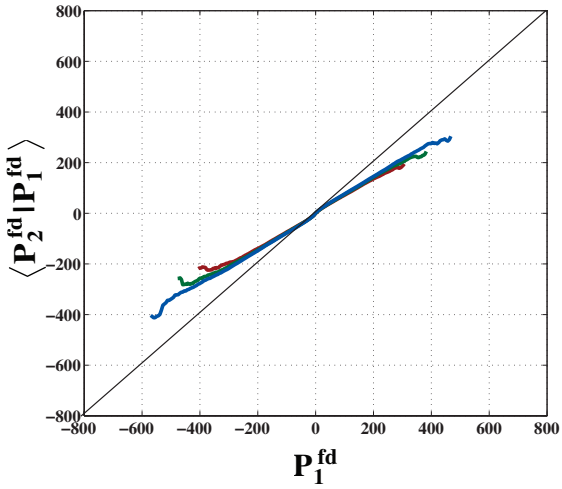

(a)

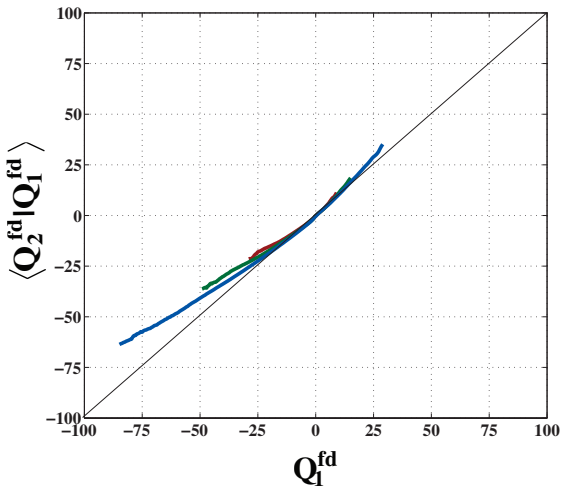

(b)

Figure 2.3: Conditional means of variance transport terms (**a**) $\langle P_2|P_1\rangle$ (**b**) $\langle Q_2|Q_1\rangle$ computed at a filter width of 32η using spectral (——) C2 (——), C4 (——), and P6 (——), schemes.

fields exhibit correlation in space and time. If methods based on independent samples are applied to correlated data, it should be with the awareness that the effective sample size is significantly reduced [40]. With a smaller sample, it becomes more important to distinguish between sample estimates and the actual population value of a statistic and to provide some quantification of the uncertainty of the estimate before generalizing the result.

This point holds in particular for computing conditional means, which have attracted much recent attention as a yardstick of best-case modeling outcomes [5, 8–10]. In the most simplistic approach, the data is subdivided into bins based on the value of the conditioning variable. It is likely that some bins will have a very limited sample. Additionally, if the conditioning variable is known to exist in small, intense structures, then some bins will have samples that come from just a few of these structures. The conditional variance of these bins could appear low, not only because a strong relationship exists between the conditioned and conditioning variables, but also because of a high spatial correlation within each bin's set of samples. This is an issue that requires further exploration before more specific comments can be made. For now, it suffices to note that too much importance should not be attached to estimated statistics associated with the outlying values of a single data set. For example, Fig. 2.4 shows the conditional variance of the exact production term, Eq. 1.16 conditioned on Z_v as evaluated at a single instant from two different DNS realizations belonging to the same ensemble. At low Z_v values the conditional variance appears to be estimated consistently, but at high Z_v

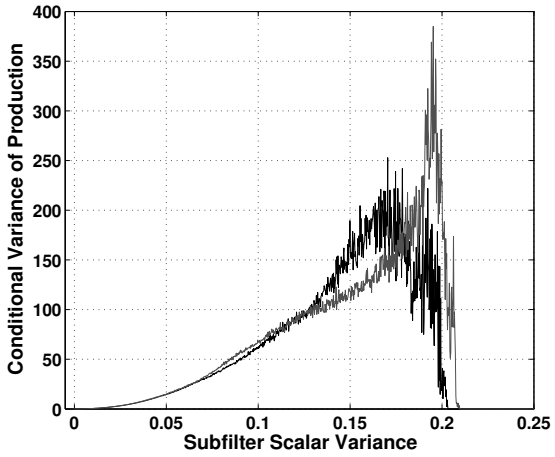

Figure 2.4: Comparison of estimated conditional variances of production from two distinct but equivalent DNS realizations.

values the estimates show little agreement.

Chapter 3

A Posteriori Analysis of Variance Modeling Errors

Because static, DNS-based tests can only partially address the sources of variance modeling error encountered in practical LES, a novel a posteriori approach was developed to further assess model performance. Portions of this work also appear as Ref. 41.

3.1 Motivation

LES subfilter models are prone to numerical errors due to the unique nature of practical LES computations. The formulation of LES proceeds by first filtering the flow and scalar transport equations, leading to a set of partial differential equations for the filtered variables. The filtering operation essentially removes all scales below a cut-off length, the filterwidth. These partial differential equations are then discretized on a numerical grid and solved. Theoretically, the filterwidth characterizes the LES solution while the grid spacing determines the accuracy of its numerical approximation. In most practical applications of LES, the filterwidth and grid spacing are equal. As a result, solutions to the LES equations are well-known to be highly dependent on the

choice of numerical discretization [12–14]. The error introduced by numerical discretization is wavenumber dependent and increases with wavenumber. Consequently, the length scales of the LES solution near the filterwidth are severely contaminated by numerical errors.

It should be noted that this disproportionate error in small scale information affects all subfilter models, including those for the residual stress and subfilter scalar flux. Furthermore, many subfilter models require the evaluation of spatial derivatives and therefore have their own discretization error. However, subfilter variance modeling has some unique aspects because the variance is needed to parameterize a combustion model, not to close an LES governing equation. Unlike a residual stress model that directly affects the resolved velocity input to it, a variance model is used to predict quantities such as temperature that only indirectly influence subsequent variance predictions. Therefore, conclusions about numerical effects on variance modeling, and the implications of those effects for a simulation's predictive value, cannot be inferred from analyses of other subfilter quantities. Since combustion is highly sensitive to the level of mixing at the small scales, LES predictions are critically dependent on the accuracy of variance models and it is important that the role of numerical error be understood.

Previously, most evaluations of variance modeling accuracy have been conducted using a priori tests on DNS data and have not analyzed model discretization error [9, 24, 28, 30, 34, 42, 43]. A more limited number of studies have also included a posteriori tests using LES [24, 43]. These studies note

modeling error in the filtered scalar evolution as a factor in variance prediction, but do not specifically characterize its effects and also do not account for numerical error in the filtered scalar evolution.

In this study, we consider three impacts of numerical error on variance modeling in the context of grid-based filtering, which is by far the dominant filtering approach in combustion LES. First, numerical discretization errors alter the evolution of the filtered fields that serve as input variables for the models. Second, the variance model itself may require numerical discretization, leading to additional errors. Third, model coefficients may be computed by dynamic estimation procedures [22] that incur numerical error. Ch. 2 summarized a prior study, Ref. 39, which used an a priori analysis technique to show that the second and third types of error listed above can have significant and non-obvious consequences for variance prediction by combining to either magnify or partially cancel the total error of the model evaluation. Here the analysis accounts for all three types of errors by using a novel coupled DNS-LES method for a posteriori model evaluation. A description of the method can be found in Sec. 3.2. Filtered scalar evolution error is found to be an important factor in variance modeling accuracy, especially affecting dynamic algebraic models for variance as explained in Sec. 3.3.2.

Considering numerical errors wholly apart from physics-based modeling errors would have imposed an artificial disjunction in our analysis as both types of errors depend on and in turn influence the simulated flow dynamics. Because the analysis method allowed comparisons to both DNS and numeri-

cally accurate LES results, modeling error was an easily observed aspect of the results. In particular, it was necessary to address the dissipation rate modeling problem of transport equation models for variance, which are covered in Sec. 3.3.3, because the consequences of dissipation rate modeling error can far outweigh numerical error effects. In this work, the dissipation rate model was calibrated using DNS scalar information. A dynamic modeling approach is currently being developed based on the variance transport equation. Complete characterization of numerical error in transport equation models will require this dynamic approach to be analyzed also. Here it is assumed that the numerical error of the dynamic procedure will be in keeping with the discretization error of the variance transport equation on which the new dynamic model is based.

3.2 DNS-LES a Posteriori Method

Since the objective of this work is to assess the role of numerical errors on variance model performance, a posteriori tests have to be designed carefully. Often, spatially inhomogeneous flows such as round jets that are closer to realistic applications are used to assess model performance. However, such tests are not useful for our purpose. First, in such spatially inhomogeneous systems, it is difficult to separate the errors due to closures for the momentum equations from the scalar variance closures. Secondly, it can be challenging to obtain the highly numerically accurate solution required for comparison when spectral methods are not applicable. In addition, the range of filterwidths that

can be used is limited by the need to resolve the shear layers. These issues can be avoided by using homogeneous isotropic turbulence (HIT) as the testbed case within the coupled DNS-LES method we propose for evaluation of scalar modeling. Because this analysis examines both causes and effects of variance prediction error, its findings provide useful guidance for diagnosing variance model performance in more complex geometries.

Exclusion of turbulence modeling errors and careful attention to the effects of filtered scalar evolution error distinguish the methodology used here from other a posteriori analyses of variance modeling, even those also using HIT [24]. Only by controlling for these factors can transport equation models, algebraic models, and DNS variance results be compared in an informative manner.

3.2.1 Computational Method

Our simulation method is built upon a pseudospectral code for direct numerical simulation of homogeneous isotropic turbulence [44, 45]. This DNS solver was modified to additionally solve the LES filtered scalar equation (Eq. 1.10), STE model (Eq. 1.21), and VTE model (Eq. 1.15). The accuracy of the equations' discretizations could be varied from spectral (SP) numerical accuracy by replacing true wavenumber values with modified wavenumbers corresponding to second order central (C2), fourth order central (C4), and sixth order Padé (P6) schemes [13, 15]. The code's DNS functionality was retained, allowing fully resolved velocity and scalar fields to be simulated alongside the

LES quantities.

To clarify the subsequent discussion, we introduce some conventions for our notation. First, a symbol without additional superscripts represents a quantity that has been computed from DNS in exact form. For example, a plain $\mathcal{P}$ denotes production values obtained by applying Eq. 1.16. Second, a symbol accompanied by a superscript indicates a modeled quantity. The superscript itself denotes the numerical accuracy used to evaluate the model and any of its input variables. Thus, $\mathcal{P}^{\mathrm{C2}}$ is calculated from Eq. 1.17 with second order discretization and the input variables $\overline{Z}^{\mathrm{C2}}$ (the solution to Eq. 1.15 with second order discretization) and D_T^{C2}. A superscript 'DNS' indicates a modeled quantity computed from DNS inputs with spectral numerical accuracy. Third, variance results are distinguished by a model and an order of accuracy. For instance, $Z_v^{\mathrm{VTE}-2}$ is the VTE model value obtained from second order discretization of Eq. 1.15 and and its closures.

Prior to beginning the variance model tests, the code was run in DNS-only mode until a statistically stationary, randomly forced [46] velocity field was obtained. Next, a DNS resolution scalar field was initialized [44] and used to generate four identical initial filtered scalar fields ($\overline{Z}^{\mathrm{SP}}$, $\overline{Z}^{\mathrm{C2}}$, $\overline{Z}^{\mathrm{C4}}$, $\overline{Z}^{\mathrm{P6}}$). The initial Z field was also used to produce four copies of the initial condition of $\overline{Z^2}$ for the STE evolutions or of Z_v for the VTE evolutions. The simulation was then resumed in DNS-LES mode. Rather than solving LES momentum equations, filtered DNS velocities were used for advancing all the LES scalar, second moment, and variance equations. The filtered velocities were also required for

computing the eddy diffusivity (Eq. 1.11 using a dynamic model [22]). Because no eddy viscosity model was required, the dynamic coefficient $\mathcal{C}_d$ was determined directly rather than found using a turbulent Schmidt number. At each iteration, $\mathcal{C}_d$ was estimated and eddy diffusivity values were computed for each of the four filtered scalars. For example, D_T^{C2} was found from $\overline{Z}^{\mathrm{C2}}$ and the filtered velocities using second order finite differencing, and so on. Likewise, a subfilter dissipation and production value were computed for each of the four VTE evolutions and a filtered dissipation rate was found for each of the four STE evolutions. Finally, the BPR and CDM dynamic variance models were computed from each of the filtered scalars using the corresponding numerical scheme.

The simulation procedure is summarized in Fig. 3.1. As it shows, four variance models are evaluated at four levels of nominal numerical accuracy. At each level of accuracy, the four variance models' predictions are linked by a shared filtered scalar field but the variance models have no effect on each other. No interactions occur across numerical schemes as the scalars have no effect on the DNS velocity information that they share.

3.2.2 Model Comparison Approach

A typical approach to a priori subfilter model evaluation is to make pointwise comparisons between exact and modeled values of a given subfilter quantity, both having been computed from the same DNS-evolved fields, and then gauge model accuracy on the basis of correlation coefficients [47], mean

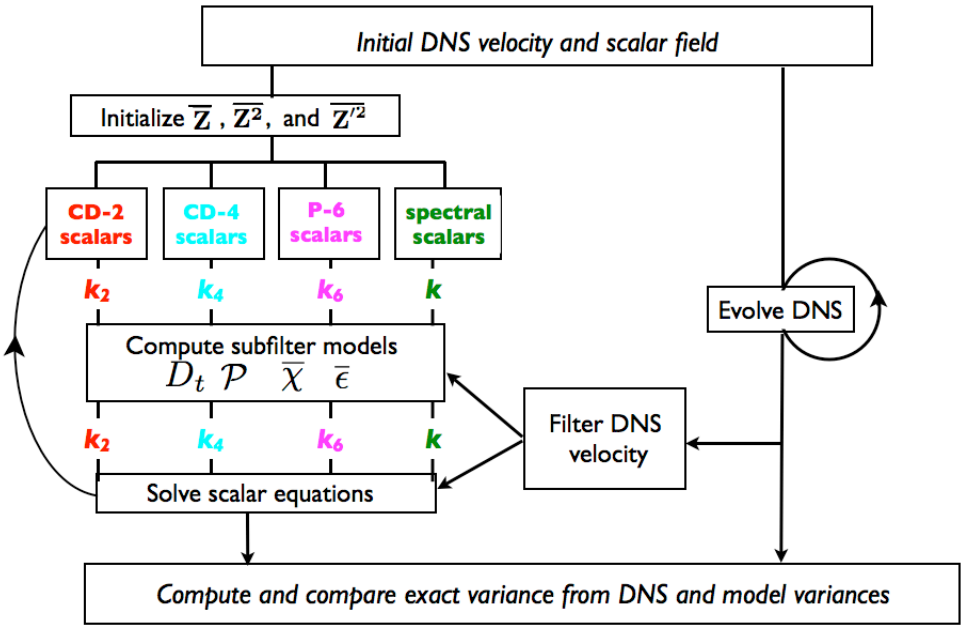

Figure 3.1: Schematic of the coupled DNS-LES simulation method.

square error [48], or similar statistics. In the current analysis, even though fields of the fully resolved, DNS-evolved scalar Z are available for computing "exact" subfilter variance values, these values are not expected to be in direct correspondence with the modeled variances. In practical LES, a given filtered field cannot be uniquely associated with a particular state of small scale turbulence [5]. Instead, models try to represent an average subfilter effect on the filtered scales due to the entire set of possible small scale conditions. The DNS fields evolved here represent just one of these subfilter states, so the filtered DNS results cannot be tracked instantaneously by any LES closure. Furthermore, the LES evolutions can be expected to diverge from point-wise comparability over time due to even slight numerical error effects at each time

step. Therefore, this analysis evaluates variance modeling outcomes by comparing the statistics of the predicted variance fields, and not by computing the statistics of pointwise comparisons between those fields, or between those fields and DNS results.

Since the flow being considered is isotropic, a subfilter variance field at a given time step is readily recast as an approximate one-point, one-time pdf. While moments of these pdfs can be easily computed, allowing concise comparisons between models, the comprehensive information provided by the pdf is valuable, especially for providing qualitative insights to model performance. However, subfilter variance pdfs are often highly skewed, making them difficult to adequately depict using histograms and causing comparisons between model results to be too dependent on ad hoc bin selection. Quantile-quantile (q-q) plots are used in this work as an alternative method for comparing model predictions. The interpretation of q-q plots is described in the Appendix.

3.3 Results

A computational domain of 256^3 grid points was used for all simulations presented here. The DNS velocity field was forced at the large scales to maintain $\mathrm{Re}_\lambda = 80$. The DNS scalar field had a unity Schmidt number and was decaying. The evolutions of the scalar fields were carried out over periods up to about 2.5τ, where τ is the eddy turn-over time as calculated from the DNS velocity field. By this point, mean variance values were near zero. The grid spacing h was set equal to the filterwidth Δ in the modified wavenumber ex-

pressions to emulate the grid-based filtering approach. Models were tested at filterwidths of 8η, 16η, and 32η, where η is the Kolmogorov length, except for the final two transport equation modeling cases (Sec. 3.3.3.2 and Sec. 3.3.3.3) which were tested at 16η only. For all test filtering performed, $\widehat{\Delta}/\Delta = 2$.

3.3.1 Filtered Scalar Evolution

As described in Sec. 3.2, central schemes are used for all finite difference evaluations. Preferably, upwind schemes are used for scalar convection because central schemes lead to accumulation of energy at the small scales and numerical instability in the absence of a diffusion term [49]. However, when a diffusion term is present, as it is here, it acts to remove excess small scale energy and maintain stability. Therefore, it was elected to use central schemes in wavenumber space for all terms rather than employ upwinding for the convection term in physical space.

Typically, the equation for the filtered scalar is solved in the form given by Eq. 1.10, with the diffusion term evaluated using two applications of a first derivative finite difference operator. As a result, the diffusion term is underpredicted at high wavenumbers, even when a sixth-order accurate scheme for the first derivative is used. The consequences of this lack of accuracy are clear when the spectra of the filtered scalars are compared, as in Fig. 3.2(a). More energy persists at high wavenumbers for scalars evolved with lower order schemes, although the numerically exact subfilter scalar flux closure is actually overdissipative. Further tests showed this to be due, at least in part, to over-

prediction of the model's coefficient caused by lack of scale invariance between the filter and test scales. To test the effect of convective term error, filtered scalars were also evolved with exact treatment of the convection operator but finite difference evaluation of their diffusion terms. Scalars evolved with lower order schemes still had greater energy at high wavenumbers, indicating that the differences between schemes are not due solely to convection term errors.

A simple means to partially remedy this problem consists in expanding the diffusion operator as

$$\frac{\partial}{\partial x_i}\left[\left(D+D_T\right)\frac{\partial\left(\cdot\right)}{\partial x_i}\right]=\frac{\partial(D+D_T)}{\partial x_i}\frac{\partial\left(\cdot\right)}{\partial x_i}+\left(D+D_T\right)\frac{\partial^2\left(\cdot\right)}{\partial x_i^2} \tag{3.1}$$

allowing a second derivative finite difference operator to be used for part of the diffusion term. The spectra of filtered scalars evolved using the diffusion term in the form given on the right hand side of Eq. 3.1, shown in Fig. 3.2(b), testify to the improved accuracy of this representation. However, the effects of finite difference error are still obvious and are not compensated by the dynamically-modeled eddy diffusivity because its energy content is almost uniform across the resolved scales.

3.3.2 Dynamic Models

The a priori tests of Chapter 2 show that implementation of either the CDM or BPR dynamic closures (Eqs. 1.23-1.27) using finite differences leads, on average, to underprediction of the subfilter variance compared to numerically exact modeling. When acting upon the same filtered DNS scalar fields,

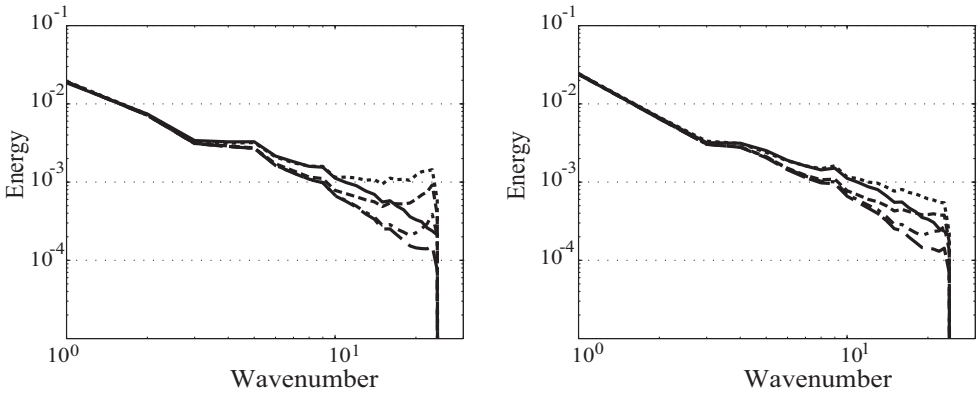

Figure 3.2: Filtered scalar $\overline{Z}$ spectra at $t = 0.7\tau$ for filtered DNS (———) and LES evolved with spectral (— —), C2 (·····), C4 (- - - -), and P6 (—·—) schemes using diffusion term as given by (**a**) Eq. 3.1, LHS (**b**) Eq. 3.1, RHS.

lower order finite difference schemes generally underestimate the gradient-based quantity $\mathcal{M}_v$ (in both its BPR and CDM forms) in the denominator of the expression for the model coefficient $\mathcal{C}_v$, while the Leonard term $\mathcal{L}_v$ is unaffected. Consequently, the value of $\mathcal{C}_v$ decreases as more accurate schemes are used. In the dynamic model, the model coefficient multiplies $|\nabla\overline{Z}|^2$, which increases in value when approximated by more accurate schemes. Thus, the numerical error observed in the modeled variance depends on the degree of error cancellation occurring between $\mathcal{C}_v$ and $|\nabla\overline{Z}|^2$.

When dynamic models are evaluated within an LES, the filtered scalar field input to the model includes modeling and numerical errors. Clearly, changes in model input lead to changes in model output. A side effect is that the numerical error within the variance model computation can also be modified if the errors in the LES filtered scalar evolution produce a field that

is more or less smooth than that obtained by filtering DNS of the same flow.

As shown in Fig. 3.2, filtered scalars evolved using finite differences are left with a greater amount of energy at high wavenumbers as the simulation progresses. Since $\mathcal{L}_v$ is a measure of scalar energy between the test and LES filter scales, higher values of $\mathcal{L}_v$ result as lower accuracy centered differences are used. As in the a priori case, $\mathcal{M}_v$ is underestimated by finite differences relative to its actual value for a given scalar field. The difference here is that each scheme acts on a different scalar field, so scalar evolution error competes with gradient evaluation error in determining $\mathcal{M}_v$. A similar competition between these two sources of error occurs in the determination of $|\nabla\overline{Z}|^2$.

Fig. 3.3 shows how the distributions of predicted variance values change as the simulation proceeds. Results are shown for $\Delta = 16\eta$ only, but are representative of the results at 8η and 32η. The nearly linear shape of the quantile-quantile plots, found for each filterwidth considered across a range of times, indicates that both models and all finite difference schemes produce distributions of subfilter variance values that are similar in shape to the pdf of the true variance, which is strongly left-skewed with a long right tail. Although values in the tail occur relatively infrequently, they are significant because they signal the presence of a fuel-air interface. For times less than half an eddy turn over time (not shown), both models predict distributions of variance values with right tails that are too short. This result is manifested in underprediction of the 0.8 and higher quantiles. Variance values peak at about 0.6τ, the time depicted in Fig. 3.3(a). Subsequently, as shown in Figs. 3.3(b)-(c) lower order

schemes predict more extreme values of Z_v than higher order schemes due to the error of the filtered scalar evolution counteracting gradient underprediction. At all times, CDM model values are higher than the corresponding BPR model values, which is easily explained by comparing the models' expressions for $\mathcal{M}_v$.

Mean variance values $\langle Z_v \rangle$ are tracked in Fig. 3.4. A mean value is determined as the arithmetic average of the variance values associated with each grid point in the domain. These results are consistent with the quantile comparisons. Average modeled variances are generally too low.

In summary, q-q plots indicate that the scaling relationship proposed by the dynamic model manages to capture the distributional form of variance values for this flow. However, model results are very sensitive to the smallest scales of the filtered scalar solution, which are most susceptible to model and numerical error. Numerical error in computing $|\nabla \overline{Z}|^2$ is insufficiently compensated for by overprediction of $\mathcal{C}_v$, resulting in underprediction of variance.

3.3.3 Transport Equation Models

Transport equation models present an attractive alternative to algebraic dynamic models because they avoid the assumption of local equilibrium between production and dissipation. However, it then becomes necessary to specify the dissipation rate model constant $\mathcal{C}_\tau$, which had been conveniently subsumed by the dynamic variance model coefficient $\mathcal{C}_v$. The results obtained from the STE and VTE depend strongly on the way in which dissipation is

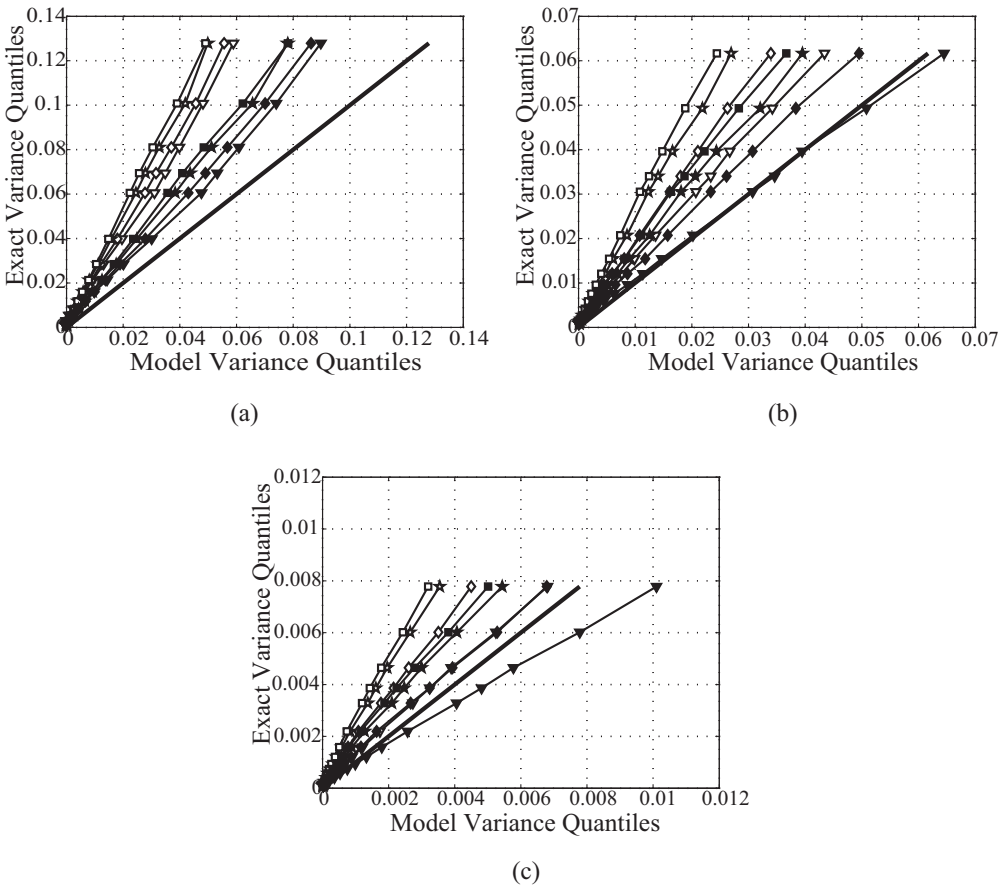

Figure 3.3: Quantile-quantile comparison of dynamic variance model predictions to DNS results (——). Shown are CDM (filled symbols) and BPR (open symbols) model results at filterwidth $\Delta = 16\eta$ and times of (**a**) 0.6τ (**b**) τ and (**c**) 2τ. Schemes used for filtered scalar evolution and variance model implementation are spectral (square), C2 (triangle), C4 (diamond), and P6 (star).

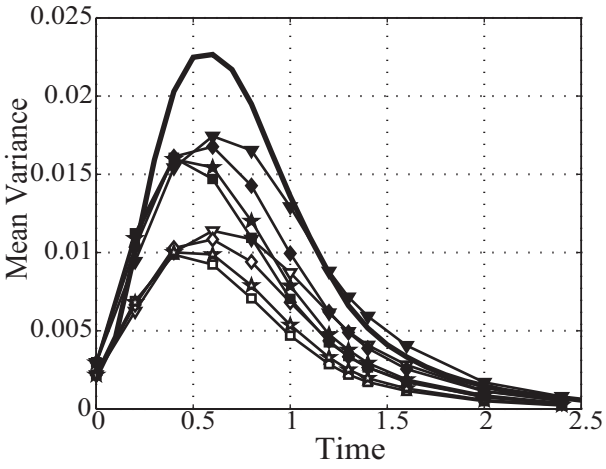

Figure 3.4: Evolution of volume mean of subfilter variance predictions by DNS (——) and CDM (filled symbols) and BPR (open symbols) dynamic models for $\Delta = 16\eta$. Schemes used for filtered scalar evolution and variance model implementation are spectral (square), C2 (triangle), C4 (diamond), and P6 (star).

modeled. In fact, dissipation modeling error can be far more severe than numerical error. Variance modeling results using three different dissipation closure methods are discussed below and shown in Fig. 3.5. In the first case, the usual approach in practical LES was followed by setting $\mathcal{C}_\tau$ to an assumed constant value. The selected value proved to be too low, causing the VTE and STE to predict excessively high variance values [Fig. 3.5(a)]. The next two cases exploited DNS scalar information to aid in dissipation modeling. These approaches allow the overall potential of transport equation-based variance modeling to be assessed pending further developments in dissipation rate modeling. The second case fitted a linear model to values of $\overline{\epsilon}_Z$ and Z_v/τ_Z from DNS [Fig. 3.5(b)]. In the third case, no model form was assumed. In-

stead, mean values of $\overline{\epsilon}_Z$ and $\overline{\chi}_Z$ conditioned on Z_v were computed from the DNS scalar field, then supplied as models to the VTE and STE evolutions [Fig. 3.5(c)].

3.3.3.1 Constant $\mathcal{C}_\tau = 2$

Fig. 3.6 shows q-q plots of variance predictions made using the second moment equation. The STE model results for $\Delta = 16\eta$ at $t = \tau$ are compared to DNS values in Fig. 3.6(a)-(b). Clearly, the STE model results are not a good match to the values obtained from DNS or, for that matter, from one of the dynamic models. They differ in both magnitude and distributional form. Where the true variance has a left skewed distribution, the STE model produces variance values that are more broadly and almost symmetrically distributed around the mean value, which, as shown in Fig. 3.5(a), is too high. In Fig. 3.6(b), the predictions of the STE solved using finite difference methods are compared to the spectral solution. Reducing the accuracy of the finite difference scheme lengthens both tails of the predicted variance distribution. The left tail extends to negative variance values, which are not physically realizable. The zero values of the lowest quantiles result from clipping these negative variance values to zero.

The main reason for the discrepancy between the STE results and the true variance is the performance of the model for $\overline{\chi}_Z$. From the quantiles plotted in Fig. 3.7(a), it can be seen that the model fails to replicate the full range of $\overline{\chi}_Z$ values observed from DNS. On the other hand, model quantiles exceed

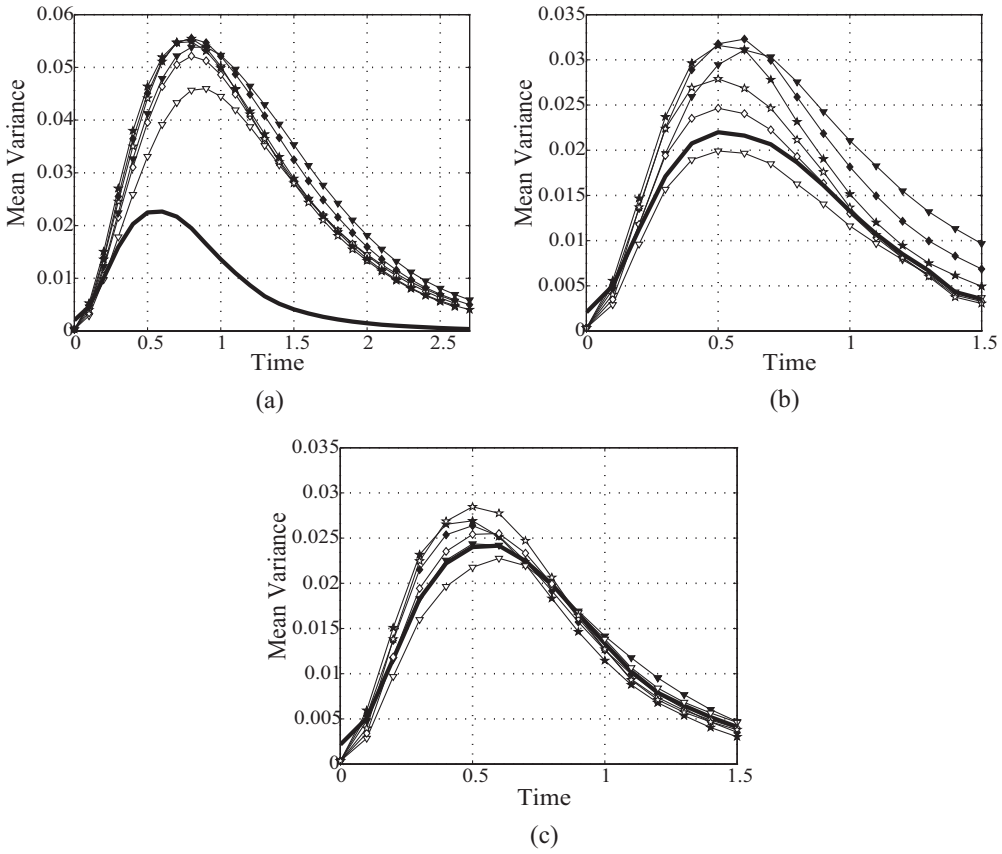

Figure 3.5: Evolution of volume mean of subfilter variance predictions by DNS (——), STE (filled symbols), and VTE (open symbols) for (**a**) Case 1, $\mathcal{C}_\tau = 2$ (**b**) Case 2, linear fit (**c**) Case 3, conditional mean. Schemes used are C2 (triangle), C4 (diamond), and P6 (star).

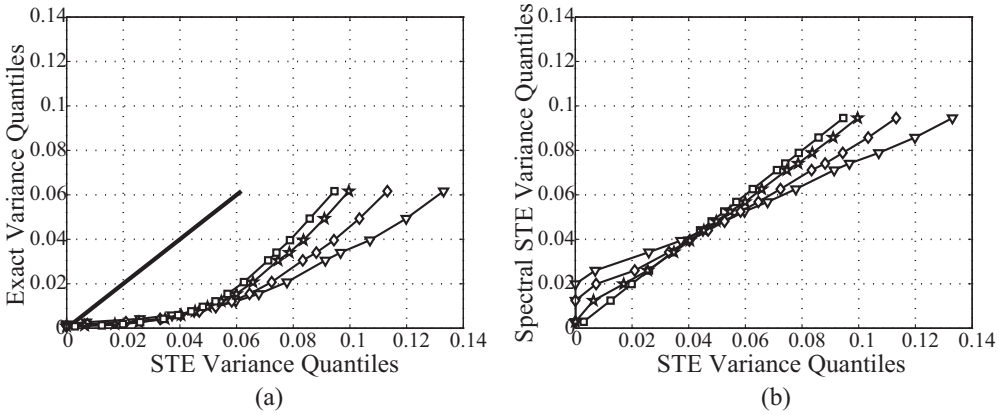

Figure 3.6: Quantile-quantile comparison of STE variance model predictons in Case 1. Predictions for filterwidth $\Delta = 16\eta$ at $t = \tau$ are plotted against (**a**) DNS variance (——) and (**b**) spectral STE results. Schemes used are spectral (square), C2 (triangle), C4 (diamond), and P6 (star).

DNS quantiles over an interval corresponding to about 60 percent probability due to overprediction of Z_v^{STE}. This trend is explained by examining the conditional means of filtered scalar dissipation rate predictions conditioned on the subfilter variance value, denoted by $\langle\overline{\chi}|Z_v\rangle$ and depicted in Fig. 3.7(b). The model mean values are nearly linear, since the average contribution of the second term ($2D\nabla\overline{Z}\cdot\nabla\overline{Z}$) is small relative to that of the first term ($\mathcal{C}_\tau Z_v/\tau$) and values of τ are not strongly correlated to those of Z_v. In comparison to the DNS results, the choice $\mathcal{C}_\tau = 2$ is clearly too low. While the relationship between DNS values of $\langle\overline{\chi}|Z_v\rangle$ and Z_v is not purely linear, it seems that the current functional form of the model is less problematic than the setting of model parameters. This issue will be taken up again in Sec. 3.3.3.2.

Fig. 3.8 shows the predictions of the variance transport equation at

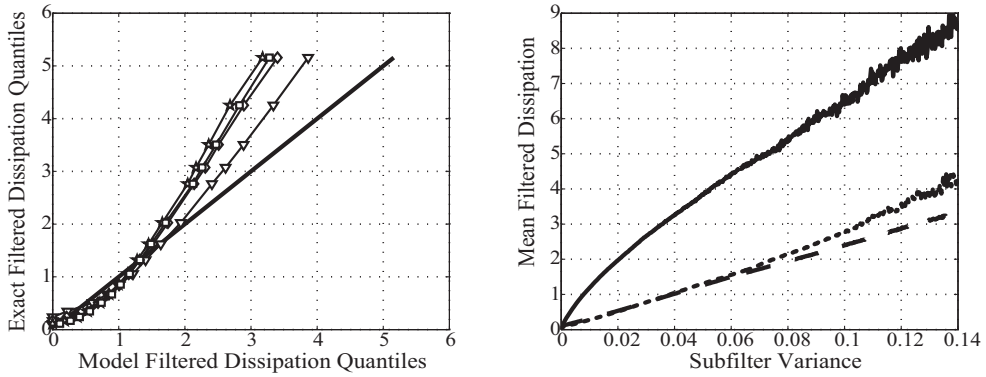

Figure 3.7: Filtered scalar dissipation rate $\overline{\chi}_Z$ results for STE with $\Delta = 16\eta$ at $t = \tau$ in Case 1. (**a**) quantile-quantile comparison of $\overline{\chi}_Z^{\mathrm{SP}}$ (square), $\overline{\chi}_Z^{\mathrm{C2}}$ (triangle), $\overline{\chi}_Z^{\mathrm{C4}}$ (diamond), and $\overline{\chi}_Z^{\mathrm{P6}}$ (star) values with exact $\overline{\chi}_Z$ from DNS (———) and (**b**) mean filtered dissipation conditioned on the variance, showing exact DNS $\langle \overline{\chi}_Z | Z_v \rangle$ (———), and model results $\langle \overline{\chi}_Z^{\mathrm{SP}} | Z_v^{\mathrm{STE-SP}} \rangle$ (▪▪▪▪▪▪), and $\langle \overline{\chi}_Z^{\mathrm{C2}} | Z_v^{\mathrm{STE-2}} \rangle$ (▬ ▬). The variance range extend to the 0.99 quantile of $Z_v^{\mathrm{STE-2}}$ values.

$t = \tau$ with $\Delta = 16\eta$. As for the STE, the VTE model predicts a roughly symmetrical distribution of variance values, rather than the highly skewed distribution followed by DNS and dynamic model values. Predicted values are generally too high, although the overprediction is slightly improved over the STE due to numerical errors in the production term.

As already discussed in Sec. 3.3.2, numerical error in evaluating $|\nabla\overline{Z}|^2$ can be large when the filterwidth and grid spacing are equal. It was verified that underprediction of the production term was not a result of modeling error in Eq. 1.17. Fig. 3.9 presents an a priori evaluation of the model using the fully resolved Z from DNS. Conditioned on the exact subfilter variance, the models yields higher production values on average. In fact, the true production term can act as a sink for variance. At the time depicted ($t = \tau$), about twenty percent of the actual production values were negative. The mean modeled production, conditioned on the true production, shows that the model is quite good at predicting the magnitude of energy transfer but can only allow transfer in one direction.

3.3.3.2 Fitted Dissipation Model Coefficients

The modeling error encountered in predicting the subfilter scalar dissipation rate is a primary source of error for both the VTE and STE approaches. However, within this testing framework, the accuracy of the dissipation rate model can be significantly increased by using information from the concurrent DNS scalar evolution. The viability of transport equation based variance

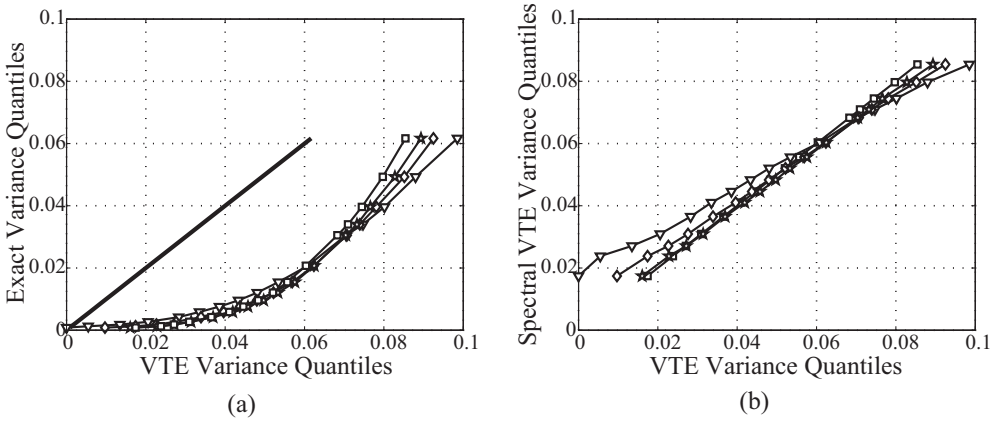

Figure 3.8: Quantile-quantile comparison of VTE variance model predictions in Case 1 with $\Delta = 16\eta$ at $t = \tau$. Quantiles of $Z_v^{\mathrm{VTE-SP}}$ (square), $Z_v^{\mathrm{VTE-2}}$ (triangle), $Z_v^{\mathrm{VTE-4}}$ (diamond), and $Z_v^{\mathrm{VTE-6}}$ (star) are plotted against quantiles of (**a**) exact Z_v (———) and (**b**) $Z_v^{\mathrm{VTE-SP}}$.

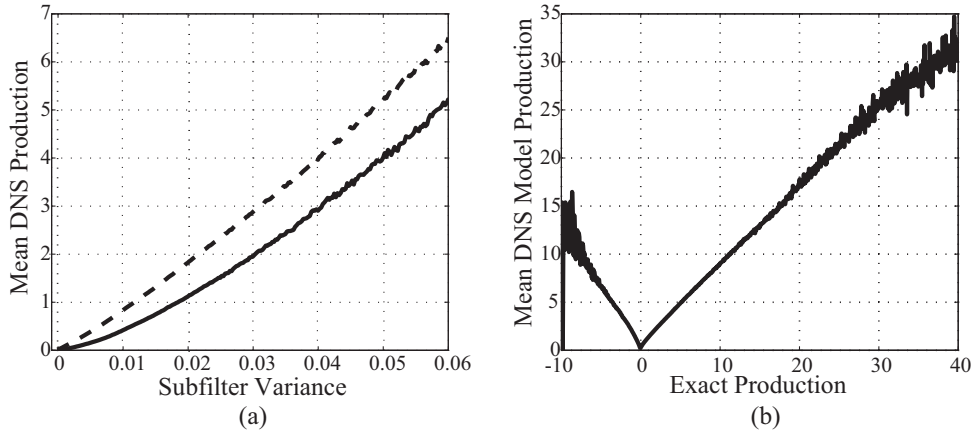

Figure 3.9: Conditional means of variance production $\mathcal{P}$ from DNS with $\Delta = 16\eta$ at $t = \tau$ comparing exact and model results. (**a**) $\langle \mathcal{P} | Z_v \rangle$ where Z_v is the exact variance and $\mathcal{P}$ is from Eq. 1.16 (———) and $\langle \mathcal{P}^{\mathrm{DNS}} | Z_v \rangle$ from production model Eq. 1.17 (– – –) and (**b**) $\langle \mathcal{P}^{\mathrm{DNS}} | \mathcal{P} \rangle$.

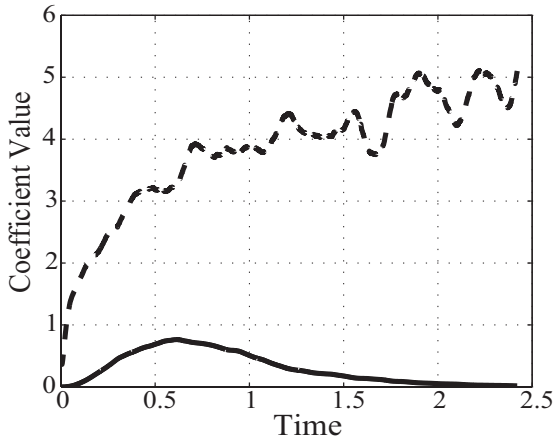

Figure 3.10: Time history of linear fit dissipation model constants c_0 (——) and c_1 (– –) in Case 2.

modeling in terms of numerical error effects can then be assessed without overwhelming errors in dissipation rate modeling. In this section, the current modeling form for $\overline{\epsilon}_Z$ is retained, but model constants are determined from the DNS scalar evolution. Specifically, at each time step, values of $\overline{\epsilon}_Z$ and Z_v/τ_Z are computed from the DNS scalar field and a least squares linear fit is made to the data. The least squares coefficients are then used to determine modeled dissipation values according to

$$\overline{\epsilon}_Z = c_0 + c_1 \frac{Z_v}{\tau_Z}. \tag{3.2}$$

Ideally, $c_0 = 0$ to avoid the occurrence of negative variance values, but this value was not prescribed. Non-zero c_0 indicate nonlinearity in the relationship between $\overline{\epsilon}_Z$ and Z_v/τ_Z.

A sample time history of the fitted coefficients is shown in Fig. 3.10 to illustrate general trends. The exact behavior varies somewhat between DNS

realizations. The value of c_1 is initially low, but as the mean variance reaches its peak, c_1 attains a value of about four, more than twice the previously used value $\mathcal{C}_\tau = 2$. Afterward, c_1 fluctuates but continues to show an increasing trend out to 2.5τ. The constant term, c_0, peaks at about the same time as the mean variance. These changes can be explained by examining the shape of the conditional mean of $\langle \overline{\epsilon}_Z | Z_v/\tau_Z \rangle$, which has a similar shape to $\langle \overline{\epsilon}_Z | Z_v \rangle$ [Fig. 3.12(a)]. Notably, the portion of the curve associated with small variance values is steeper than the rest of the curve. Therefore, the value of c_1 increases as the variance decays because it is being fit to the steep part of the curve.

With this new expression for $\overline{\epsilon}_Z$, the predictions of both the VTE and STE are markedly improved. Fig. 3.5(b) depicts the evolution of the volume averaged mean variance. In general, the VTE appears more accurate than the STE due to error in the gradient-squared term of the model for $\overline{\chi}$. Since the gradient-squared quantity is multiplied by the molecular diffusivity, D, its contribution to $\overline{\chi}_Z$ can be expected to decrease for higher Reynolds number flows with D_T much greater than D. It can also be observed from Figure 3.5(b) that using a less accurate finite difference scheme lowers the mean variance prediction of the VTE. This is due to underestimation of the modeled production, which also contains the gradient-squared quantity, but multiplied by D_T instead of D. Thus, the production term is likely to become more problematic at increased Reynolds number.

3.3.3.3 Conditional Mean Dissipation Modeling

The second DNS-based modeling option uses conditional mean values to predict the dissipation rate at a point in the flow as a function of the local variance value. It is well known that the conditional mean of X conditioned on Y, $\langle X|Y\rangle$, is the most accurate predictor, in terms of mean square prediction error, of X given knowledge only of Y [11]. This fact suggests using conditional statistics computed at each timestep from the DNS as dissipation rate "models."

For the VTE, this approach gives

$$\overline{\epsilon}_Z^{\mathrm{VTE}} = f(Z_v^{\mathrm{VTE}}) \tag{3.3}$$

where

$$f(\xi) = \left\langle \overline{\epsilon}_Z^{\mathrm{exact}} | \xi = Z_v^{\mathrm{exact}} \right\rangle . \tag{3.4}$$

Similarly, the STE uses

$$\overline{\chi}_Z^{\mathrm{STE}} = g(Z_v^{\mathrm{STE}}) \tag{3.5}$$

where

$$g(\xi) = \left\langle \overline{\chi}_Z^{\mathrm{exact}} | \xi = Z_v^{\mathrm{exact}} \right\rangle . \tag{3.6}$$

The conditional means are computed based on the DNS scalar field but are applied to the modeled variance fields, and so are not necessarily the best predictor for those fields because they evolve under modeled equations. This procedure does not guarantee a correct unconditional mean dissipation unless the distribution of variance values from DNS and the model are the

same, which requires that the entire transport equation model be accurate. However, these dissipation models should show good accuracy compared to other models based on the variance value at each point. Results from these models can be compared to the results of the previous section to gain a sense of the effectiveness of the existing dissipation model formulation.

In terms of mean variance prediction, the accuracy of the STE using Eq. 3.5 more nearly approaches that of the VTE using Eq. 3.3, as shown in Fig. 3.5(c). Comparing Fig. 3.5(c) to Fig. 3.5(b), the VTE shows smaller gains in accuracy, indicating that the timescale relationship model reasonably approximates the conditional mean model provided the proper model coefficients can be specified. Means of the P6 and spectral evolutions are almost equivalent for both transport equation models, so only the P6 results are shown in these figures.

Quantiles are plotted in Fig. 3.11. The STE shows less disparity between schemes than the VTE as the variance values reach their peak around $t = 0.5\tau$. By $t = \tau$, as the variance values are decaying, this finding is reversed. This could be due to the combined effect of filtered scalar and second moment evolution error on the STE. On the other hand, C4, P6, and spectral VTE results have nearly collapsed, although the C2 VTE result shows poor agreement because of numerical error in the production term. It can also be observed from Fig. 3.11 that many of the q-q plots have an initial vertical segment. These vertical segments result from clipping unphysical negative model variance values to zero. In general, the STE requires more clipping of negative

values than does the VTE due to the subtraction step required to evaluate the variance.

While the conditional mean models improve the prediction of mean variance values, their accuracy is limited. This is a concern given the scalar dissipation rate's role in combustion modeling. The conditional standard deviation, conditioned on variance, of both the filtered and subfilter scalar dissipation rates is quite high, indicating that large fluctuations about the mean values occur even at low scalar variance values. Note that the conditional standard deviation, defined as

$$\mathrm{sdev}\left(\overline{\epsilon}_Z|Z_v\right) = \left\langle \left(\overline{\epsilon}_Z - \langle\overline{\epsilon}_Z|Z_v\rangle\right)^2 |Z_v\right\rangle^{1/2} \tag{3.7}$$

is related to the irreducible error [8–10] associated with the predictor variable Z_v by

$$\left\langle \left(\overline{\epsilon}_Z - \langle\overline{\epsilon}_Z|Z_v\rangle\right)^2\right\rangle = \left\langle \mathrm{sdev}\left(\overline{\epsilon}_Z|Z_v\right)^2\right\rangle. \tag{3.8}$$

The conditional mean of $\overline{\epsilon}_Z$ is compared to its standard deviation for three different times in Fig. 3.12, which shows that the variability of the dissipation rate persists even after the scalar is fairly well mixed. This error in dissipation rate modeling can be dealt with in two different ways. In the first approach, we can directly formulate a model for the standard deviation of the dissipation rate through a presumed pdf approach or through a stochastic model. Here, it is assumed that the standard deviation arises from the lack of a model that characterizes the fluctuations in the dissipation rate. Alternately, we can take the view that this standard deviation is the irreducible error that arises from

the random nature of the subfilter scalar disitribution. Based on stochastic estimation theory [11] it is then possible to reduce this error by choosing a model that uses additional input variables.

3.4 Summary

This chapter presents a new approach to a posteriori analysis of scalar modeling that removes the effect of turbulence modeling errors through a coupled DNS-LES simulation method. The analysis approach was used to assess four subfilter scalar variance models, with a focus on numerical error effects in the context of practical LES using grid-based filtering. Dynamic models were found to be sensitive to filtered scalar modeling and discretization error as well as numerical error in discretizing the models, which are based on the magnitude of the filtered scalar gradient. The models generally underpredicted the variance. Because central schemes were used to discretize the filtered scalar transport equation, numerical error in the filtered scalar evolution somewhat counteracted the model discretization error. However, when the filtered scalar equation is solved using dissipative upwind schemes it is likely that the two errors will compound.

Two transport equation models were considered, the second moment transport equation (STE) and variance transport equation (VTE) models. Although these models are equivalent at the level of their continuous equations, they yield different results when discretized. The greatest effect of numerical error was observed in the VTE model through its production term. Like the

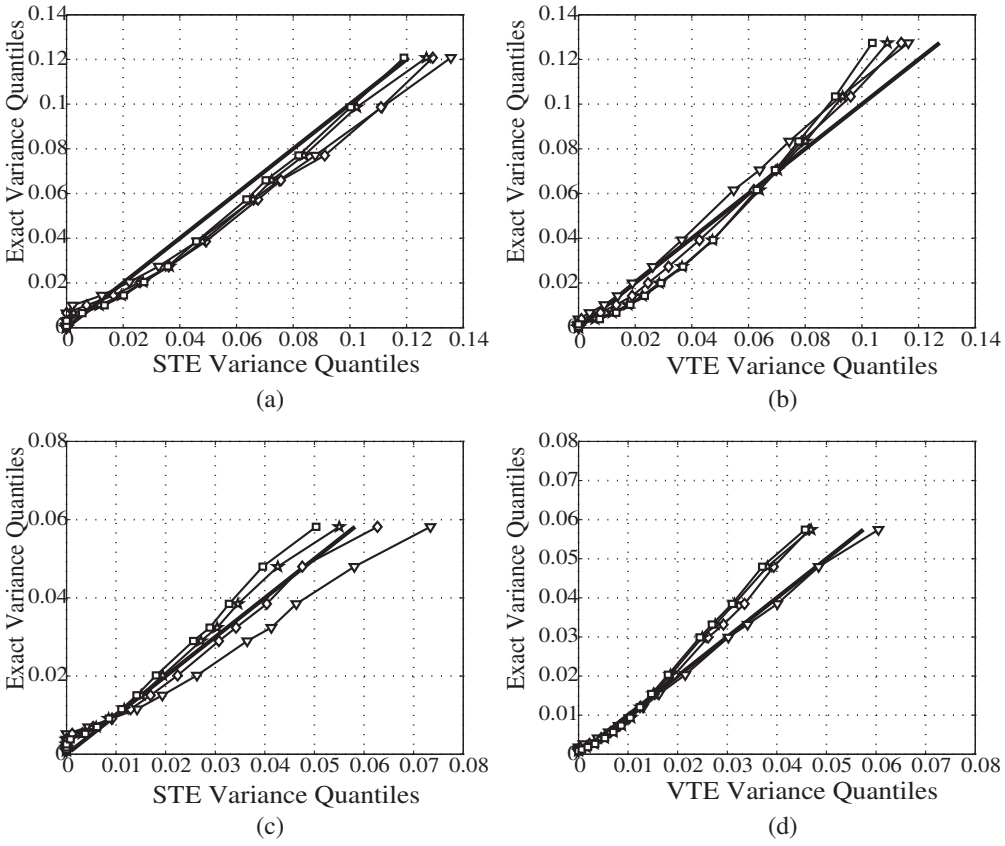

Figure 3.11: Quantile-quantile comparison of variance model predictions from Case 3. Results with filterwidth $\Delta = 16\eta$ are plotted for (**a**) STE, $t = 0.5\tau$ (**b**) VTE, $t = 0.5\tau$ (**c**) STE, $t = \tau$ and (**d**) VTE, $t = \tau$. Schemes used are spectral (square), C2 (triangle), C4 (diamond), and P6 (star).

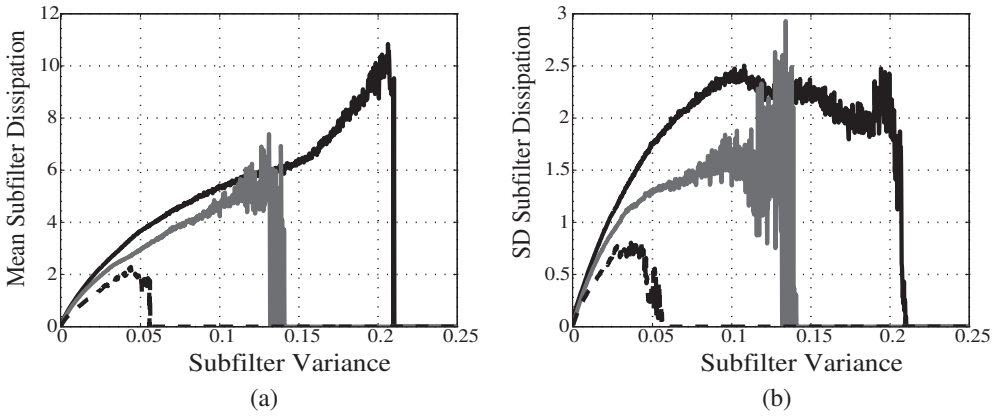

Figure 3.12: Conditional statistics of subfilter scalar dissipation evaluated from DNS with filterwidth $\Delta = 16\eta$ including (**a**) conditional mean $\langle \overline{\epsilon}_Z | Z_v \rangle$ and (**b**) conditional standard deviation $\mathrm{sdev}(\overline{\epsilon}_Z | Z_v)$ at times 0.5τ (——), τ (——), and 1.5τ (– –).

dynamic models, the production model depends on the magnitude of the filtered scalar gradient and is underpredicted by finite differences. The resolved dissipation term in the STE model was underpredicted for the same reason, but is typically a less significant term than production in high Reynolds number flows. Additionally, the use of higher order schemes was effective in reducing the numerical error in both models' predictions. Mean variances from the sixth-order Padé scheme implementations of the STE and VTE showed very close agreement with mean variances from the spectral accuracy model implementations.

Closure of the subfilter scalar dissipation rate was found to be the major issue for both transport equation models. Modeling strategies were tested by calibrating dissipation rate models using the fully resolved scalar

fields available from the DNS portion of the simulation. The results show that variance can be predicted fairly accurately using dissipation models based on the local variance value and a mixing timescale, despite the random error of variance-based prediction of dissipation. A dynamic estimation procedure to set the model coefficient $\mathcal{C}_\tau$ has been developed in light of these results and is presented in Ch. 5.

Chapter 4

Explicit Filtering for Numerically Accurate Scalar Modeling

The results of Ch. 3 explored the effects of numerical error on scalar modeling by varying the order of finite difference scheme used in the discretization of the LES scalar equations while holding the resolution of the computational mesh constant relative to the filterwidth. For transport equation models , a sixth-order accurate Padé (P6) scheme was accurate enough to yield good agreement with the mean subfilter variance predictions from spectral implementation of the models. In contrast, P6 results did not converge to spectral results in the case of algebraic dynamic models because these models are strongly dependent on the smallest scales of the filtered scalar field. Variance prediction was strongly affected by numerical error when second and even fourth order accurate schemes were used. Nevertheless, only such lower order schemes are practicable in many LES computations. The explicit filtering methodology is an alternative means of controlling numerical error in LES. Additionally, it makes the filter that effectively operates on the discretized LES equations more consistent with the filtering operation that is used to derive the continuous LES equations [50]. This aspect of explicit filtering is explained in more detail in Sec. 4.1. However, explicit filtering increases the cost of a

simulation for a fixed filterwidth and also affects the formulation of subfilter models, so the benefits of explicit filtering need to be evaluated carefully.

In this chapter, the explicitly filtered scalar equations and subfilter models are formulated and the coupled DNS-LES method is modified to examine the numerical convergence of these equations in homogeneous isotropic turbulence as the ratio Δ/h (filter-to-grid ratio, or FGR) is increased from 1 to 8 by fixing Δ while refining the computational mesh. An indication of the modeling complications that arise in the explicit filtering approach is given by the fact that the variance transport equation cannot be written in a convenient form, although the second moment transport equation remains available as a modeling choice. Nonetheless, increasing the FGR leads to numerically converged results for the filtered scalar and subfilter variance.

4.1 LES Equations and the Filtering Operation

As described in Sec. 1.1, most large eddy simulations and all known LES of combustion use a form of filtering that is referred to in this work as grid-based filtering. In this approach to filtering, the coarseness of the computational mesh, combined with discrete evaluation of derivatives, takes the place of a well-defined filter operator to eliminate small length scales from the flow solution [51]. In one dimension, the relationship between discrete differentiation and filtering can be easily demonstrated [51]. However, the system of partial differential equations to be solved in LES involves a mix of first and second derivatives in all three coordinate directions and cannot be

linked to a single filter operator. In effect, a different filter acts on each term of the equation [52, 53]. Furthermore, the filter acting on a particular term varies spatially and temporally when numerical schemes employing adaptive stencils, such as WENO schemes [54], are used and different discretizations are frequently employed for the filtered momentum and scalar transport equations, leading to an effective filter that depends on the variable type. Undoubtedly, a coarse numerical discretization limits the length scales present in the flow solution but the precise way in which those length scales have been removed is impossible to characterize. It is important to note that some type of filtering of the LES solution is required because nonlinear terms in the equations generate smaller scales. In Chapters 2 and 3, the choice of numerical scheme was treated as a separate layer on top of the filter effect attributed to the mesh resolution. This was possible because spectral methods were available for solving the LES equations and the filter-like effects of finite differencing could be separated from those of limited mesh resolution. However, these two effects are inextricably bound in most flow simulations, leading to grid-based filtering sometimes being described as a combined product of grid spacing and numerical methods.

The basic idea of the explicit filtering approach is to use a grid spacing which is smaller than the filterwidth so that the filtered solution is numerically well resolved. The wavenumber content of the filtered fields is controlled by filtering the nonlinear terms of their evolution equations. A fundamental question in the explicit filtering approach is the nature of the filtering operation and its implications for the filtered flow equations to be solved. Explicitly

defined filters already see use in grid-filtered LES, where they accomplish the test filtering operation required in dynamic modeling approaches. Typically, box filters are used under the assumptions that the grid-based filter is approximately a box filter and that the test and LES filter should be of the same type, as well as for their convenience. Clearly, no such constraint applies when the LES filter itself is explicitly defined. While conventional filter forms, such as the box filter, remain available, other formulations have been proposed with specific desirable properties. In particular, when the filter-width varies throughout the domain, commutation error between filtering and differentiation occurs. For purposes of deriving the LES equations from the Navier-Stokes and scalar transport equations, a commutation error operator can be defined as [52]

$$\left[\frac{\partial \psi}{\partial x_i}\right] = \overline{\frac{\partial \psi}{\partial x_i}} - \frac{\partial \overline{\psi}}{\partial x_i} \tag{4.1}$$

A method for constructing discrete filters which commute with differentiation up to some order of accuracy was presented in Ref. 52, and filters of this type were recently used in LES of channel flow [55]. Commutation error is not an issue for the simulations performed here. Nonetheless, the procedure developed for discrete commuting filters is still useful because it allows a filter transfer function to be defined independently of the computational mesh. Therefore, increasing computational resolution through mesh refinement does not alter the physical resolution of turbulence imposed by the filter.

4.2 Discrete Commutative Filters

This section provides a brief overview of the method used for defining discrete commutative filters. More details can be found in Refs. 52 and 55. The method is applicable to a stretched Cartesian grid that can be mapped to a uniformly spaced mesh in a computational space. Three-dimensional filtering is achieved by applying a one-dimensional discrete filter in each coordinate direction. Restricting our attention to the one-dimensional case for simplicity, consider a variable $\psi^d(x)$ defined on a discrete mesh with constant mesh spacing h in the mapped computational coordinate ξ, where $x = f(\xi)$. The superscript 'd' is introduced to emphasize that ψ^d is a discrete variable. Then the filtering operation at grid point x_j (here j indicates the grid point location, rather than a vector component as in Einstein notation) can be written as [52]

$$\overline{\psi^d}(x_j) = \sum_{l=-K_j}^{L_j} w_l^j \psi^d(f(\xi_j + lh)) \tag{4.2}$$

or, more compactly, as

$$\overline{\psi}_j^d = \sum_{l=-K_j}^{L_j} w_l^j \psi_{j+l}^d \tag{4.3}$$

In these equations, j is the index of the grid point and l indexes the location of a point within the filter stencil relative to the grid point. The extent of the filter stencil is given by the integers K_j and L_j and may vary over the domain to cope with boundaries. Corresponding to each point in the stencil is a weight, w_l^j, which must be determined by prescribing certain properties of the filter. One such property is order of commutation error. For m-th order

accuracy in commutation error, the moments of the filter function M^k must be zero for $k = 1, 2..., m-1$ [52]. As for all LES filters, it is necessary that $M^0 = 1$. These constraints on the values of the filter moments can used in a constrained minimization procedure to produce filters whose transfer functions closely match a desired shape, usually an approximation to a sharp spectral filter [52]. This approach to setting filter weights is used here, following the procedure developed in Ref. 55 and, as in that work, specifying nominal fourth order accuracy in commutation error and the filter transfer function shape shown in Fig. 4.2. The filterwidth Δ is set by forcing the value of the filter transfer function $\widehat{G}(\pi/\Delta) = 0.5$.

It should be noted that the prescribed level of commutation error may not be observed in a simulation because the relevant definition of commutation error is no longer in terms of continuous filtering and differentiation, as in Eq. 4.1, but rather in terms of discrete filtering and differentiation. This discrete commutation error can be written as

$$\left[\frac{\delta\psi^d}{\delta x}\right] = \overline{\frac{\delta\psi^d}{\delta x}} - \frac{\delta\overline{\psi^d}}{\delta x} \tag{4.4}$$

where $\delta/\delta x$ indicates a finite difference operator. In Ref. 52, an expression for the order of commutation error is found using the calculus of continuous variables, which especially relies on the Taylor series representation of ψ and involves derivatives of ψ and of the filter moments M^k. No discrete analog to this expression is developed in Ref. 52. Instead, the expression for continuous variables and continuous filter functions is assumed to hold in the discrete case.

However, it will be shown here that in the discrete case, the magnitude of the commutation error depends on the details of the finite difference scheme as well as the filter. This can easily be seen by writing a generic finite difference operator as

$$\frac{\delta\psi^d}{\delta x}(x_j) = \sum_{i=-M_j}^{N_j} v_i^j \psi_{j+i}^d \tag{4.5}$$

Substituting Eq. 4.5 and Eq. 4.3 into Eq. 4.4 gives the discrete commutation error as

$$\left[\frac{\delta\psi^d}{\delta x}(x_k)\right] = \sum_{j=-K_k}^{L_k} w_j^k \sum_{l=-M_{k+j}}^{N_{k+j}} v_l^{k+j} \psi_{k+j+l}^d - \sum_{i=-M_k}^{N_k} v_i^k \sum_{j=-K_{k+i}}^{L_{k+i}} w_j^{k+i} \psi_{k+j+i}^d \tag{4.6}$$

Under the definition of commutation error for continuous variables (Eq. 4.1), no commutation error occurs if the filter function does not depend on the filtering location, but only on the displacement from that location. For the discrete filter, this lack of spatial variation simplifies Eq. 4.6 to

$$\left[\frac{\delta\psi^d}{\delta x}(x_k)\right] = \sum_{j=-K}^{L} w_j \left(\sum_{l=-M_{k+j}}^{N_{k+j}} v_l^{k+j} \psi_{k+j+l}^d - \sum_{i=-M_k}^{N_k} v_i^k \psi_{k+j+i}^d \right) \tag{4.7}$$

and zero commutation error is not guaranteed unless the finite difference scheme is also non-varying. In that case, we have

$$\left[\frac{\delta\psi^d}{\delta x}(x_k)\right] = \sum_{j=-K}^{L} w_j \left(\sum_{l=-M}^{N} v_l \psi_{k+j+l}^d - \sum_{i=-M}^{N} v_i \psi_{k+j+i}^d \right) = 0 \tag{4.8}$$

The commutation error of discrete filters will not be investigated further here, but it is worth pointing out that what is true in the mathematics of continuous variables may not carry over to the discrete case. Another example of this,

already encountered in this work, is the difference in the computational results of the STE and VTE despite the equivalence of their continuous equations.

Commutation error is not an issue in these simulations, where the periodic domain allows uniform filtering and finite difference operators to be applied at all grid points and in each of the three coordinate directions. Rather, three vanishing moments (M^1, M^2, and M^3) were specified to generate filters that are similar to what may be used in more practical computations. As a rule of thumb, the nominal order of commutation error should be at least as high as the order of truncation error [52]. Weights were computed for $\Delta/h = 2, 4, 8, 16$ to account for both the LES explicit filter and the test filter used in dynamic modeling procedures and are listed in Appendix B.

A disadvantage to filters of this kind is the large stencil size required to obtain nicely shaped filters. For example, the test filter corresponding to the $\Delta/h = 4$ case has a stencil of 29 points. Large stencil size increases the cost of filtering in terms of the number of arithmetic operations and amount of interprocessor communication required and results in a larger region where the filter must be modified to account for domain boundaries. If filter size varies slowly or only second order accurate numerical schemes are used, it may be preferable to use a more compact box filter, as all filters that are symmetric in the computational coordinate, including the standard box filter, commute to at least second order [50].

Another shortcoming of the current form of the discrete commuting filter method is that it is not applicable to structured meshes in cylindrical

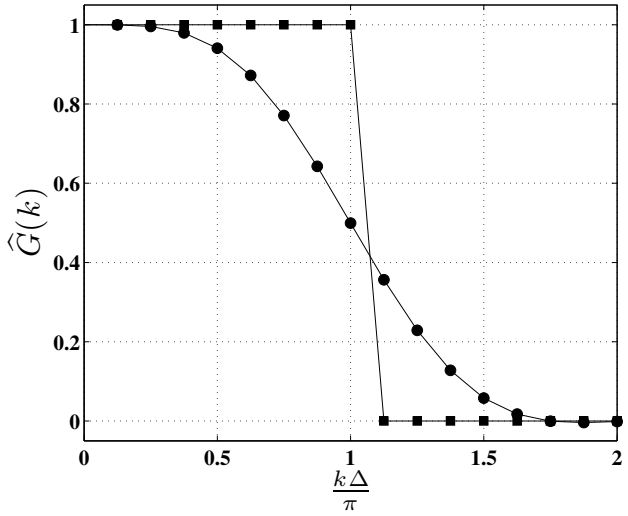

Figure 4.1: Transfer functions of one-dimensional filters. The discrete commuting filter (●) used in the present work is compared to a sharp spectral filter (■). Note that $\widehat{G}\,(\pi/\Delta) = 0.5$ for the discrete commuting filter.

coordinates, which are frequently employed in simulations of round jet flames. Further investigation of this issue is planned as an area of future work.

4.3 Scalar Equations in Explicit LES

The use of explicit filtering invalidates some of the assumptions used in deriving a transport equation for subfilter scalar variance. Here, we provide the explicitly filtered scalar equation and second-moment transport equation. The incompressible flow formulation is used for the reasons given in Sec. 1.2.In LES using explicit filtering, the filtered scalar transport equation is given by

$$\frac{\partial \overline{Z}}{\partial t} + \frac{\partial \overline{u_i}\,\overline{Z}}{\partial x_i} = \frac{\partial}{\partial x_i}\left[\ \overline{D\frac{\partial \overline{Z}}{\partial x_i}}\ \right] - \frac{\partial M_{Z,i}}{\partial x_i} \tag{4.9}$$

and $M_{Z,i}$ denotes the subfilter scalar flux term that is now defined as $\overline{u_i Z} - \overline{\overline{u_i}\overline{Z}}$. Substituting an eddy diffusivity model closes the explicitly filtered scalar equation as

$$\frac{\partial \overline{Z}}{\partial t} + \frac{\partial \overline{\overline{u_i}\overline{Z}}}{\partial x_i} = \frac{\partial}{\partial x_i}\left[\overline{(D + D_T)\frac{\partial \overline{Z}}{\partial x_i}} \right] \tag{4.10}$$

This should be compared to Eq. 1.10, written for the grid-based filtering approach. Note that in contrast to some implementations of explicit filtering, no distinction is made between subfilter scales and subgrid scales [56] and deconvolution modeling techniques [57] are not employed. This approach is taken to maintain a clear distinction between modeling and discretization in developing the closed form equations and ensures that the subfilter models are themselves numerically resolved.

No modification of the algebraic dynamic variance models (Eqs. 1.23-1.27) is required under explicit filtering, Only the CDM form of the dynamic closure [34] is implemented here as it showed superior performance to the BPR form [9] in Ch. 3.

In grid-filtered LES, the variance transport equation can be derived in a straightforward manner from the second moment transport equation (Eq. 1.21) and the equation for $\overline{Z}^2$, which is obtained by multiplying Eq. 1.10 for the filtered scalar by $2\overline{Z}$ and applying the product rule. The resulting LES variance transport equation is identical in form to the variance transport equation used in Reynolds averaged simulations [17]. Eq. 4.10 cannot be manipulated to yield a transport equation for $\overline{Z}^2$ in the expected form for deriving the variance transport equation. However, no new complications arise in writing the

explicitly filtered equation for $\overline{Z^2}$,

$$\frac{\partial \overline{Z^2}}{\partial t} + \frac{\partial \overline{u_i}\,\overline{Z^2}}{\partial x_i} = \frac{\partial}{\partial x_i}\left[\overline{(D + D_T)\frac{\partial \overline{Z^2}}{\partial x_i}} \right] - \overline{\chi}_Z \tag{4.11}$$

This equation is identical to the equation for $\overline{Z}$ except for the appearance of the unclosed filtered scalar dissipation term $\overline{\chi}_Z$.

Substituting the solutions of Eq. 4.11 and Eq. 4.10 into Eq. 1.12 completes the explicitly filtered second moment transport equation (exSTE) model for Z_v.

4.3.1 Subfilter Closures

Closure of Eq. 4.11 and Eq. 4.10 requires models for the eddy diffusivity D_T and the filtered scalar dissipation rate $\overline{\chi}_Z$. The dynamic model of Ref. 22 is used for D_T, taking the form

$$\left[\widehat{\overline{u_i}\overline{Z}} - \widehat{\overline{u}_i}\,\widehat{\overline{Z}} \right] = \mathcal{C}_Z \left[\widehat{\overline{\Delta^2 |\overline{S}| \frac{\partial \overline{Z}}{\partial x_i}}} - \widehat{\Delta}^2 |\widehat{\overline{S}}| \frac{\partial \widehat{\overline{Z}}}{\partial x_i} \right] \tag{4.12}$$

after accounting for the altered form of the nonlinear terms. In this expression, $\widehat{(\cdot)}$ indicates spatial test filtering at a filterwidth $\widehat{\Delta}$. The ratio $\widehat{\Delta}/\Delta = 2$ is used for computing the model.

Letting $\mathcal{L}_{Z,i}$ and $\mathcal{M}_{Z,i}$ denote, respectively, the bracketed quantities on the left- and right-hand sides of Eq. 4.12, the model coefficient is estimated by $\mathcal{C}_Z = \langle \mathcal{L}_{Z,i} \mathcal{M}_{Z,i} \rangle / \langle \mathcal{M}_{Z,i} \mathcal{M}_{Z,i} \rangle$. Brackets $\langle \cdot \rangle$ indicate volume averaging operation whose precise definition depends on the flow configuration. A volume average is appropriate for homogeneous isotropic turbulence.

Finally, the filtered scalar dissipation rate is closed using the two term expression

$$\overline{\chi}_Z = \overline{\mathcal{C}_\tau \frac{(D + D_T)\, Z_v}{\Delta^2} + 2D \frac{\partial \overline{Z}}{\partial x_i} \frac{\partial \overline{Z}}{\partial x_i}} \tag{4.13}$$

This model form is identical to that used in LES with grid-based filtering, Eq. 1.22, except that the entire quantity is filtered to make its wavenumber content consistent with the definition of $\overline{\chi}_Z$. The first term on the right hand side represents the subfilter contribution to the dissipation rate and is modeled as proportional to the variance and inversely proportional to a mixing timescale that is formed from the filterwidth and total diffusivity as in Eq. 1.20. The model coefficient $\mathcal{C}_\tau$ is usually set to an assumed constant value. Here, the value $\mathcal{C}_\tau = 5$ is used based on previous experience with this flow configuration in Ch. 3. The second term is the resolved dissipation, for which no modeling is required.

4.3.2 Multiple Grid Coupled DNS-LES Method

The coupled DNS-LES method of Ch. 3 must be modified to be compatible with explicit filtering by discrete commuting filters. Previously, the LES grid spacing was enforced through the value of h used in the modified wavenumber expressions. Spectral cut-off filtering was used to remove Fourier modes higher than those the allowed by nominal LES grid resolution while solving for both DNS and LES quantities on the DNS mesh. Discrete commuting filters are designed under the assumption that the data sampling intervals match the grid spacing. Therefore, it is necessary to use separate LES

meshes for each level of resolution. FGRs of 1, 2, 4, and 8 were used, holding the filterwidth fixed while increasing the fineness of the mesh. With a 256^3 DNS grid and filterwidth of 16 times the DNS grid spacing (equal to 24 times the Kolmogorov scale η), these ratios correspond to LES meshes of 16^3, 32^3, 64^3, and 128^3, respectively. Note that no explicit filtering of nonlinear terms is performed in the case with FGR = 1. This case corresponds to to the usual grid-based filtering interpretation of LES where filtering of nonlinear terms occurs implicitly through the limited mesh resolution.

A special technique was developed to transfer information from the DNS mesh to the LES mesh without interpolation and without disruption to the parallel data structure. First, a full turbulent field is filtered in place. Next, the filtered field is Fourier transformed to the DNS spectral domain using the fast Fourier transfer package FFTW [58]. The Fourier modes are arranged on the grid so that the lowest magnitude wavenumbers are at the corners of the domain and are typically stored in only a few processors The appropriate subset of Fourier coefficients, corresponding to wavenumbers up to the LES grid frequency, are identified and redistributed among the processors for efficient parallel computations, embedding the data in arrays sized for the partitioned DNS spectral domain. The inverse transform is performed only on this subset of coefficients and the result is similarly embedded in arrays sized for the partitioned DNS physical domain. This process is repeated for each FGR and is carried out at the start of the simulation to generate the initial LES scalar quantity fields and at each timestep to produce filtered velocity

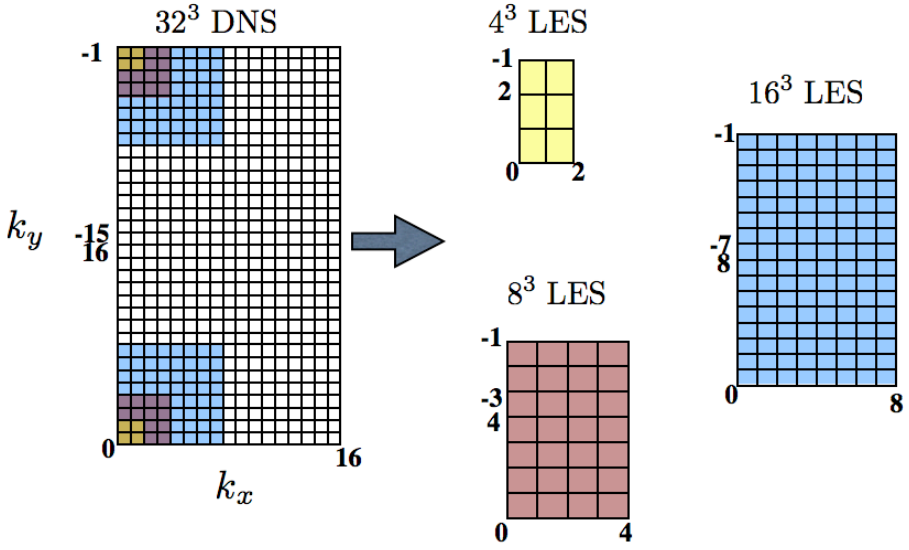

Figure 4.2: Selection of Fourier mode subsets in grid reduction method for a 32^3 DNS grid to three LES grids. A k_x-k_y plane in the three dimensional spectral domain is shown.

fields corresponding to each mesh.

Fig. 4.2 depicts the selection of Fourier modes step in the grid reduction process for a 32^3 DNS grid to three LES grids. Note that the grids shown in Fig. 4.2 are k_x-k_y planes of the spectral domain computational meshes. Processor boundaries form k_x-k_z planes. However, these are omitted from the figure for clarity.

4.3.3 Scalar Modeling Results

The second moment equation (Eq. 4.11) and dynamic variance model (Eq. 1.23) were implemented in the multiple grid coupled DNS-LES method

using second order central (C2) and fourth order central (C4) finite difference schemes. Results of the C2 and C4 cases are qualitatively similar, but the C4 case exhibits more rapid convergence as the filter-to-grid ratio is increased. The scalar fields are initialized in an unmixed state, then become increasingly well mixed as the simulation proceeds. The accuracy of mixing prediction is quantified by examining the temporal evolution of the resolved scalar energy and mean (volume averaged) subfilter scalar variance, computed from the DNS scalar field as well as the two variance models. The mean subfilter variance $\langle Z_v \rangle$ exhibits a peak as mixing proceeds from large to small scales while the resolved scalar energy $\langle \overline{Z}^2 \rangle$ decays from its initial maximum value.

Fig. 4.3 shows the numerical convergence of the resolved scalar energy. Using second order schemes, the grid-based filtering (FGR = 1) case underpredicts the rate of mixing at resolved scales. For second order schemes, increasing the FGR to 2 yields a major increase in numerical accuracy. The results for filter-to-grid ratios of 4 and higher are nearly indistinguishable. With fourth order schemes, an FGR of 2 or higher yields close agreement with spectral numerical accuracy. The converged results indicate that the eddy diffusion model for subfilter scalar flux tends to be overdissipative. This is interesting because values of the diffusivity model coefficient $\mathcal{C}_Z$ (Eq. 4.12) are highest for the least numerically accurate cases and decrease as the grid is refined. It should be recalled that the eddy diffusivity also depends on the magnitude of the filtered strain rate, $|\overline{S}|$, which is underpredicted by finite difference methods. Therefore, numerical error tends to camouflage the modeling error of the

subfilter scalar flux closure.

Numerical convergence of the mean predicted variance values occurs for both variance models, but the variance values predicted by the two models are not in agreement. The results of the explicitly filtered second moment equation model are shown in Fig. 4.5. The rates of convergence are similar to those observed for $\langle \overline{Z}^2 \rangle$, which is reasonable because the exSTE model subtracts $\overline{Z}^2$ from the result of Eq. 4.11 to find Z_v. Additionally, Eq. 4.5 has a parallel structure to Eq. 4.10 apart from the filtered scalar dissipation term, $\overline{\chi}_Z$. In Fig. 4.6, the mean value of the subfilter scalar dissipation rate converges similarly to the mean subfilter variance value. This outcome is to be expected, given the form of the subfilter scalar dissipation rate model and the use of a constant model coefficient. The resolved dissipation, shown in Fig. 4.7 manifests a stronger effect of numerical error due to its dependence on the squared magnitude of the filtered scalar gradient, which is severely underpredicted by finite difference methods [39, 41]. However, the resolved dissipation is about one-tenth the magnitude of the subfilter dissipation.

The results of the CDM dynamic variance model are shown in Fig. 4.8. This model shows a higher level of modeling error than the exSTE, tending to overpredict variance when the scalar field is primarily mixing at large scales and to underpredict variance as the scalar field becomes more finely mixed. It should be noted that the better agreement of the exSTE model with the DNS variance value is achieved by having a priori knowledge of an appropriate value of the dissipation model coefficient $\mathcal{C}_\tau$. In contrast, the model coefficient

$\mathcal{C}_v$ is estimated dynamically. Since the variance computed by the dynamic model is proportional to the squared magnitude of the filtered scalar gradient, it might be expected that the results would show a larger effect of numerical error. However, numerical error in the estimation of $\mathcal{C}_v$ has been found to compensate for gradient computation error [39, 41] and, as shown in Fig. 4.9, this tendency persists in explicitly filtered LES. Faster convergence is seen for the mean variance value predicted by the dynamic model than for the dynamic model coefficient.

4.4 Summary

This chapter discussed the application of explicit filtering methods to LES scalar modeling. The major benefit of explicit filtering lies in controlling numerical error through grid refinement while holding the filterwidth fixed, allowing grid independent LES solutions to be obtained. Explicit filtering also resolves some inconsistencies between the continuous and discrete LES equations that occur under grid-based filtering.

The multiple grid coupled DNS-LES method was to study the effects of explicit filtering on subfilter scalar variance using an algebraic dynamic model and the second moment transport equation in the form of Eq. 4.11, which is slightly modified from the STE (Eq. 1.21) used in previous chapters. A useful explicitly filtered variance transport equation cannot be written. The results showed that even lower order finite difference methods can yield numerically accurate variance predictions when combined with the explicit filtering tech-

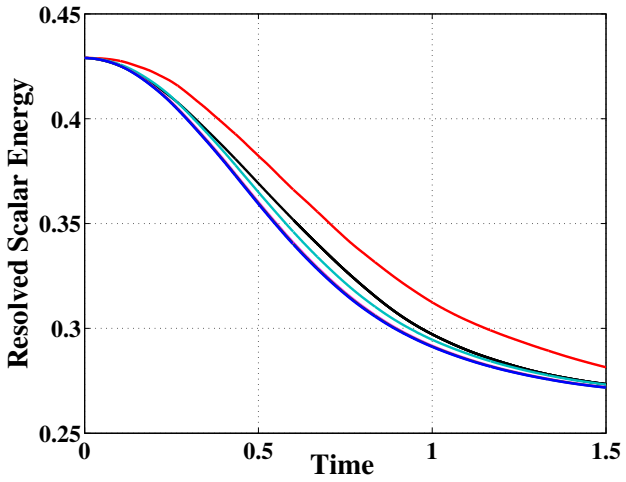

(a)

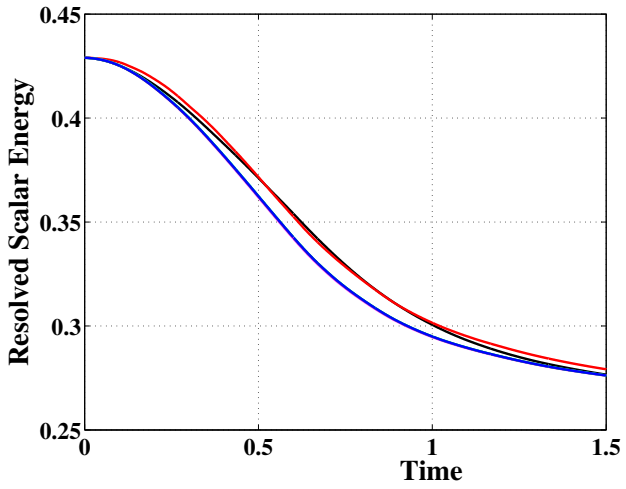

(b)

Figure 4.3: Evolution of resolved scalar energy $\langle \overline{Z}^2 \rangle$ using (**a**) second order and (**b**) fourth order schemes with filter-to-grid ratios of 1 ( ), 2 ( ), 4 ( ), 8 ( ) compared to spectral LES ( ) and filtered DNS ( ).

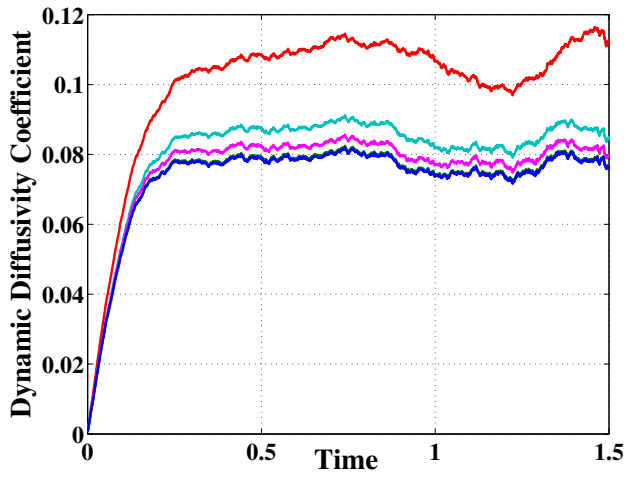

(a)

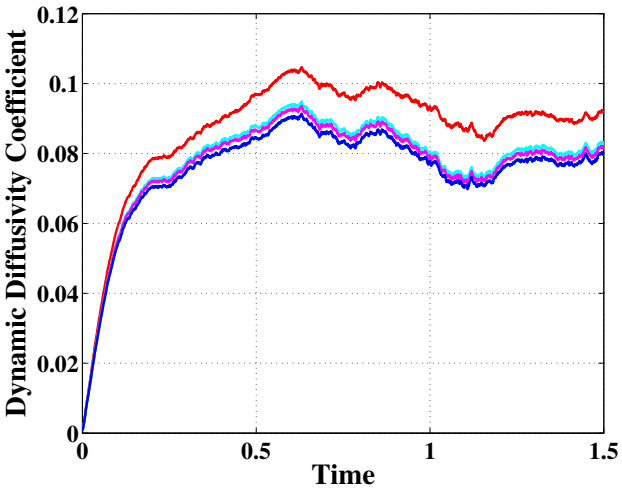

(b)

Figure 4.4: Model coefficient $\mathcal{C}_Z$ of dynamic eddy diffusivity model using (**a**) second order and (**b**) fourth order schemes with filter-to-grid ratios of 1 (——), 2 (——), 4 (——), 8 (——) compared to spectral LES (——).

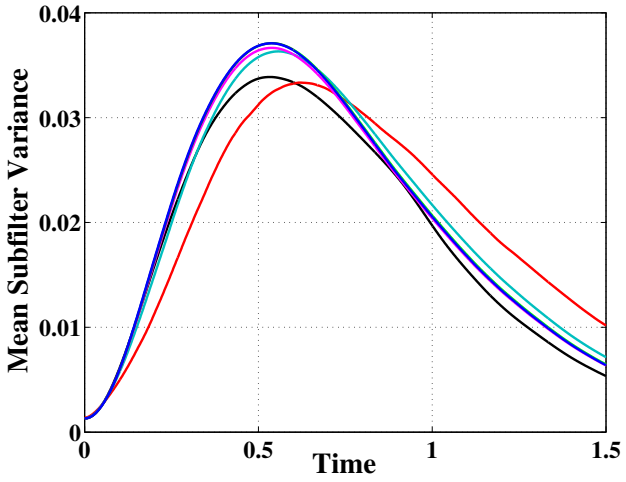

(a)

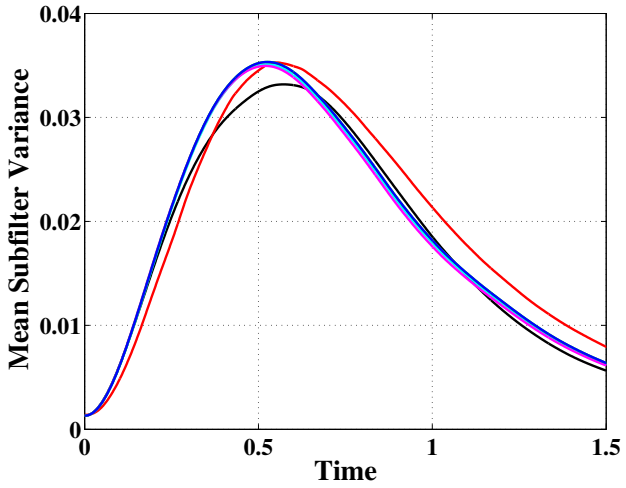

(b)

Figure 4.5: Evolution of mean subfilter scalar variance $\langle Z_v \rangle$ from exSTE using (**a**) second order and (**b**) fourth order schemes with filter-to-grid ratios of 1 (——), 2 (——), 4 (——), 8 (——) compared to spectral LES (——) and filtered DNS (——).

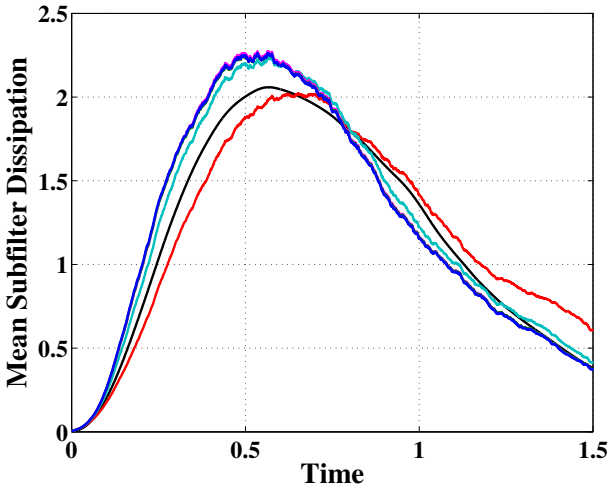

(a)

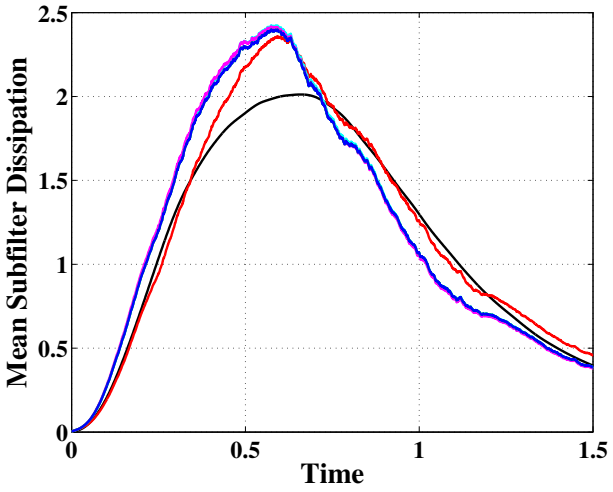

(b)

Figure 4.6: Evolution of mean subfilter scalar dissipation rate $\langle \bar{\epsilon}_Z \rangle$ from exSTE using (**a**) second order and (**b**) fourth order schemes with filter-to-grid ratios of 1 (—), 2 (—), 4 (—), 8 (—) compared to spectral LES (—) and filtered DNS (—).

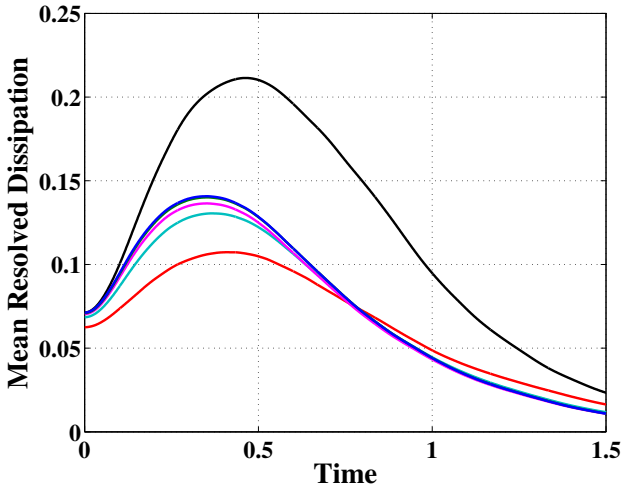

(a)

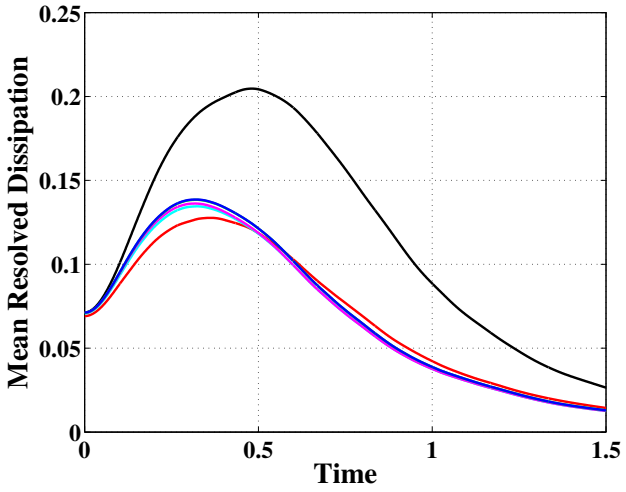

(b)

Figure 4.7: Evolution of mean resolved scalar dissipation rate using (**a**) second order and (**b**) fourth order schemes with filter-to-grid ratios of 1 (——), 2 (——), 4 (——), 8 (——) compared to spectral LES (——) and filtered DNS (——).

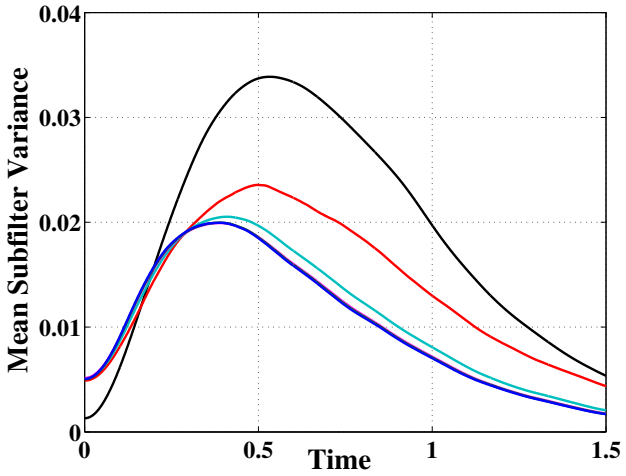

(a)

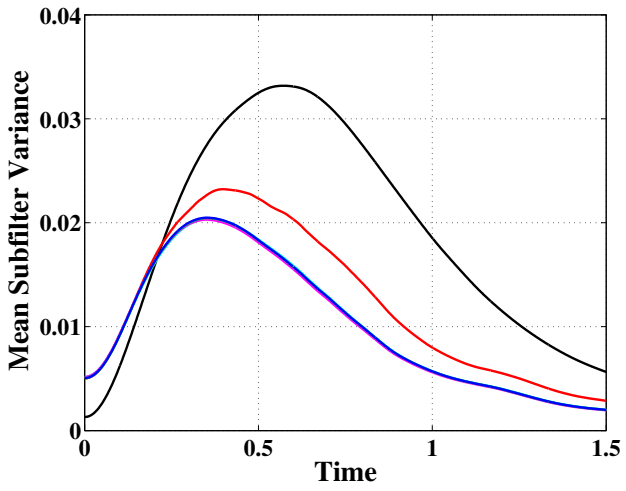

(b)

Figure 4.8: Evolution of mean subfilter scalar variance $\langle Z_v \rangle$ from dynamic model using (**a**) second order and (**b**) fourth order schemes with filter-to-grid ratios of 1 (—), 2 (—), 4 (—), 8 (—) compared to spectral LES (—) and filtered DNS (—).

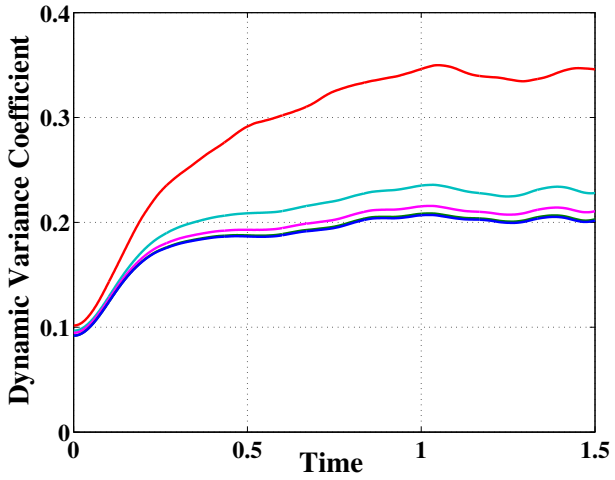

(a)

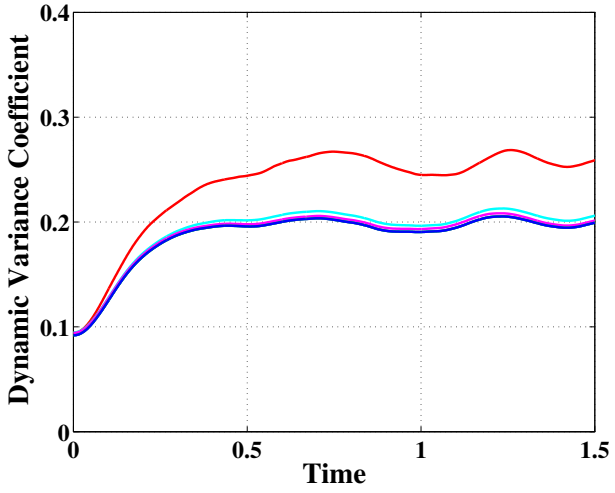

(b)

Figure 4.9: Model coefficient $\mathcal{C}_v$ of CDM dynamic variance model using second order schemes with filter-to-grid ratios of 1 (—), 2 (—), 4 (—), 8 (—) compared to spectral LES (—) and filtered DNS (—).

nique and modest filter-to-grid ratios. FGRs of 4 or greater yield variance predictions in excellent agreement with spectral accuracy results for second order schemes, while an FGR of 2 suffices in conjunction with fourth order schemes.

These results indicate that explicit filtering is a viable approach to limiting numerical error. However, the extension of explicit filtering methods to more complex flow configurations presents additional challenges. In particular, the kind of discrete commuting filter used here is not applicable to meshes defined in non-Cartesian coordinate systems. However, the geometries of many combustion systems are more naturally described in cylindrical coordinates, and development of explicit filtering approaches for such geometries will be pursued in future research.

Chapter 5

Development of a Dynamic Nonequilibrium Model for Subfilter Scalar Dissipation Rate

Modeling of scalar dissipation rate is critical to accurate simulation of turbulent combustion using LES. The role of the scalar dissipation rate in combustion modeling has been described in Chapter 1, and the importance of subfilter scalar dissipation rate modeling for scalar variance prediction was a major focus of Chapter 3. Nonequilibrium models for subfilter scalar dissipation rate, which take the form of Eq. 1.19, contain a timescale coefficient $\mathcal{C}_\tau$ that is generally unknown a priori and cannot be determined by conventional dynamic modeling procedures. In this chapter, an alternative dynamic procedure is formulated from the variance transport equation (VTE), Eq. 1.15. The modeling accuracy of the VTE-based dynamic model for $\mathcal{C}_\tau$ is assessed through a priori tests in homogeneous isotropic turbulence and in a planar jet flow. Implementation issues of the model are discussed and integration of the model with current modeling and computational methods is covered. The effects of various forms of averaging used for coefficient estimation are considered and a novel conditional averaging approach is presented. Finally, the coupled DNS-LES method is used to evaluate the effects of numerical error on the accuracy of the model's predictions.

Existing scalar dissipation rate modeling approaches are reviewed in the following section, re-emphasizing important points and elaborating on the coverage of Sec. 1.3. Note that these equations are written in the grid-based filtering framework for LES and do not use the explicit filtering techniques of Chapter 4.

5.1 Review of Scalar Dissipation Rate Modeling

The scalar dissipation rate χ_Z (Eq. 1.9) is a fundamental parameter in the study of nonpremixed flames. In such flames, species mass fractions and temperature can be related to the mixture fraction Z, a conserved scalar [2]. Reactions are assumed to occur in a thin zone around iso-surfaces of the stoichiometric mixture fraction value. The scalar dissipation rate quantifies the rate at which small scale mixing occurs and is related to the relaxation time of the diffusive layer surrounding the reaction zone. This picture of flame structure is embodied by flamelet modeling, in which local thermochemistry is determined by the values of Z and χ_Z [17].

The molecular mixing characterized by χ_Z is associated with flow length scales far smaller than those present in the filtered scalar field. As a consequence, the filtered scalar dissipation $\overline{\chi}_Z$ is dominated by its unclosed subfilter component

$$\overline{\epsilon}_Z = \overline{\chi}_Z - 2D\frac{\partial \overline{Z}}{\partial x_i}\frac{\partial \overline{Z}}{\partial x_i} \tag{5.1}$$

Since the second term in Eq. 5.1 can be computed directly from the LES filtered scalar solution, a model for either $\overline{\epsilon}_Z$ or $\overline{\chi}_Z$ provides closure for both

quantities. Here, models will be written for $\overline{\epsilon}_Z$.

The subfilter scalar dissipation rate also appears in the transport equation for the subfilter mixture fraction variance, Eq. 1.15, another key quantity in LES combustion modeling that characterizes the small scale fluctuations of Z. After closing subfilter flux terms using an eddy diffusivity D_T, the variance transport equation (VTE) is given by

$$\frac{\partial Z_v}{\partial t} + \frac{\partial \overline{u_i} Z_v}{\partial x_i} = \frac{\partial}{\partial x_i}\left[(D + D_T)\frac{\partial Z_v}{\partial x_i}\right] + \mathcal{P} - \overline{\epsilon}_Z \tag{1.15}$$

Commonly, both the subfilter scalar variance and subfilter scalar dissipation rate are modeled by algebraic closures that assume a local equilibrium between variance production $\mathcal{P}$ at resolved scales (modeled by Eq. 1.17) and dissipation at subfilter scales. This results in the model

$$\overline{\epsilon}_Z = 2D_T \frac{\partial \overline{Z}}{\partial x_i}\frac{\partial \overline{Z}}{\partial x_i} \tag{5.2}$$

Ref. 59 arrived at the same model by applying arguments from renormalization group theory.

However, variance can be predicted more accurately by using its modeled transport equation rather than an algebraic model [24, 41]. Eq. 5.2 is unsuitable for use with the variance transport equation since the final equation form would contain no source or sink terms, erroneously causing variance to be conserved in a closed system [24]. Instead, a common model [17] from Reynolds averaged simulations (RAS) is adapted to the LES context. This model can be written as

$$\overline{\epsilon}_Z = \mathcal{C}_\tau \frac{Z_v}{\tau_Z} \tag{1.19}$$

where $\mathcal{C}_\tau$ is a model coefficient and τ_Z is a mixing timescale, given by expressions such as [35–37]

$$\tau_Z = \frac{\Delta^2}{D + D_T} \tag{1.20}$$

As for any model in LES, Eq. 1.19 imperfectly captures the characteristics of the quantity it represents. A model of this type implicitly links production and dissipation by relying on a mixing timescale formed from filter scale variables and effectively assumes an energy cascade process [1, 60]. Despite the model's deficiencies, the fact remains that no alternative nonequilibrium model exists. Furthermore, from a practical standpoint, the most significant problem posed by the use of Eq. 1.19 is the determination of the model coefficient $\mathcal{C}_\tau$. The optimal value of this model coefficient is usually unknown a priori and depends on the flow under consideration and the chosen timescale expression. Furthermore, it must be recalled that in LES, unlike in RAS, $\mathcal{C}_\tau$ is a spatially and temporally varying quantity.

Dynamic procedures based on inertial range scaling arguments are often used to specify model coefficients in LES. These approaches infer the value of a subfilter scale quantity using information from the smallest filtered scales that is extracted by test filtering at a larger filterwidth $\widehat{\Delta}$. Dynamic procedures for estimating $\mathcal{C}_\tau$ have been put forth [61, 62]. However, dissipation is a predominantly small scale quantity that cannot be reliably predicted from its content in an inertial range test window. In fact, Ref. 34 specifically avoided such a dynamic scalar dissipation model when proposing a dynamic variance model. Another dynamic estimation scheme is based on a global equilibrium

assumption [10] and predicts a single time-varying value of $\mathcal{C}_\tau$ for the entire flow domain. The total subfilter variance in a periodic flow domain remains constant under this model, although mixing should reduce subfilter variance with time.

Here, we present an alternative dynamic formulation in which $\mathcal{C}_\tau$ is calibrated from the rate of scalar energy transfer between test and filter scales, which can be estimated using the VTE. A similar approach has been used to develop a model for the viscous dissipation rate of the subfilter turbulent kinetic energy [63]. However, the extreme importance of $\overline{\chi}_Z$ in combustion modeling should be recalled in addition to the function of $\overline{\epsilon}_Z$ as a sink term for scalar variance. The dual role of the scalar dissipation rate makes its modeling a unique challenge.

Four main aspects of the new dynamic scalar dissipation model (DSDM) are discussed here. First, the model is derived from the variance transport equation. Second, implementation issues of the model are presented. These issues include the selection of an averaging procedure, modeling of sub-test filter level quantities, and evaluation of the time derivative term T. The 512^3 DNS data of Chapter 2 is used to illustrate the various options. Third, the DSDM is incorporated into the coupled DNS-LES method that was introduced in Sec. 3.2 and the effects of numerical error on the model are evaluated. Fourth,the DSDM's modeling accuracy in an inhomogeneous flow is assessed through a priori analysis.

5.2 Derivation of the DSDM

The basis of the DSDM is the idea that the variance transport equation can be applied at any filter scale falling within the inertial range. On a physical level the model can be understood in terms of a mixing cascade. It should be recalled that the assumption of a mixing cascade is already implicit in the formulation of Eq. 1.19. The dynamic procedure merely makes this assumption explicit. Eq. 1.15 is the VTE written at the LES filter scale Δ. An analogous equation can be written at a test filter scale $\widehat{\Delta}$ as

$$\frac{\partial Z_t}{\partial t} + \frac{\partial \widehat{\overline{u_i}} Z_t}{\partial x_i} = \frac{\partial}{\partial x_i}\left[\left(D + D_T^t\right)\frac{\partial Z_t}{\partial x_i}\right] + \mathcal{P}^t - \mathcal{C}_\tau \frac{Z_t}{\tau_Z^t} \tag{5.3}$$

In Eq. 5.3, Z_t is the sub-test filter variance defined as $Z_t = \widehat{\overline{Z^2}} - \widehat{\overline{Z}}^2$. A superscript t indicates a model quantity evaluated at the test filter level, in contrast to a model quantity which has been test filtered. For example, the test filter level eddy diffusivity D_T^t is given by

$$D_T^t = \mathcal{C}_Z^t \widehat{\Delta}^2 |\widehat{\overline{S}}| \tag{5.4}$$

and the test filter level timescale model is

$$\tau_Z^t = \frac{\widehat{\Delta}^2}{D + D_T^t} \tag{5.5}$$

Test filtering Eq. 1.15 and subtracting it from Eq. 5.3 gives the relationship

$$\mathcal{C}_\tau X = Y = F + P - T \tag{5.6}$$

if it is assumed that $\mathcal{C}_\tau$ varies slowly in space and can be removed from the test filtering operation applied to Eq. 1.15. The quantity X on the left hand side of Eq. 5.6 is given by

$$X = \frac{Z_t}{\tau_Z^t} - \widehat{\left(\frac{Z_v}{\tau_Z}\right)} \tag{5.7}$$

The first two terms on the right hand side of Eq. 5.6 represent the differences in convective and diffusive fluxes

$$F = \frac{\partial}{\partial x_i}\left[\widehat{\overline{u_i}\overline{Z}_v} - \widehat{(D + D_T)}\frac{\partial Z_v}{\partial x_i} - \widehat{\overline{u}_i} Z_t + (D + D_T^t)\frac{\partial Z_t}{\partial x_i}\right] \tag{5.8}$$

and in production

$$P = \mathcal{P}^t - \widehat{\mathcal{P}} = 2D_T^t \frac{\partial \widehat{\overline{Z}}}{\partial x_i}\frac{\partial \widehat{\overline{Z}}}{\partial x_i} - 2\widehat{D_T \frac{\partial \overline{Z}}{\partial x_i}}\frac{\partial \overline{Z}}{\partial x_i} \tag{5.9}$$

of variance at the test and filter scale. The third term represents accumulation or loss of scalar energy between filter and test scales

$$T = \frac{\partial \mathcal{L}_v}{\partial t} \tag{5.10}$$

where $\mathcal{L}_v$ is the variance Leonard term given by

$$\mathcal{L}_v = \widehat{\overline{Z}^2} - \widehat{\overline{Z}}^2 \tag{1.24}$$

Note that $\mathcal{L}_v = Z_t - \widehat{Z_v}$. Since $\mathcal{L}_v$ can be computed directly from the resolved scalar fields, this relationship can be used to compute Z_t from the the known values of Z_v and $\overline{Z}$.

5.3 Implementation of the DSDM

Although Eq. 5.6 encapsulates the basic dynamic dissipation rate modeling idea, additional factors must be considered to put the model to use in simulations. Some choices made in model implementation can significantly affect predicted coefficient values, while others have negligible effect. Some of these options are explored here using the 512^3 DNS data of Chapter 2. beginning with selection of an appropriate averaging procedure.

5.3.1 Averaging Approaches

It has been widely recognized that estimating a dynamic model coefficient directly from an expression such as Eq. 5.6 is undesirable because the resulting coefficient values can exhibit rapid spatial variation. This violates the assumption made in removing the coefficient from test filtering operations and can negatively impact the stability of a simulation. Therefore, some form of spatial averaging is usually employed to evaluate a dynamic coefficient such as averaging over homogeneous directions of the flow [38], also referred to here as Germano averaging. By viewing points along a homogeneous direction as members of a statistical sample, this averaging can be associated with least squares line fitting [34]. Note that this differs from least squares fitting over the components of a vector expression [64], but the two ideas are often combined.

In HIT, all points in the flow are statistically equivalent. Under the Germano averaging approach, averages are taken over the entire flow domain and a single coefficient is predicted at each time step. This global averaging

approach has been used in the previous portions of this work for dynamic modeling of variance (Eq. 1.26) and eddy diffusivity. However, the relationship between $\overline{\epsilon}_Z$ and Z_v/τ_Z seems to be more complex than that expressed by a global linear fit. The quantity

$$\langle \overline{\epsilon}_Z | Z_v/\tau_Z \rangle \tag{5.11}$$

where $\overline{\epsilon}_Z$ is computed from a fully resolved scalar field using Eq. 5.1, is a valuable gauge of a dissipation rate model's accuracy. This is a specific case of the fact that the conditional mean of A conditioned on B, $\langle A|B\rangle$ is the minimum mean square error predictor of A given knowledge only of B [11]. In a priori analysis, the conditional mean, Eq. 5.11, allows the deterministic predictions of a subfilter model to be compared quantitatively to exact subfilter quantities, which are random with respect to the filtered field. Fig. 5.1 shows the conditional mean, Eq. 5.11, computed from 512^3 DNS data filtered at $\Delta = 16\eta$. Clearly, its curved shape cannot be replicated by a single value of $\mathcal{C}_\tau$. To emphasize this point, Fig. 5.1 also shows the least squares line fitted to the exact dissipation defined in Eq. 5.1,

$$\mathcal{C}_\tau^{\mathrm{LS}} = \frac{\langle \overline{\epsilon}_Z^{\mathrm{exact}} Z_v/\tau_Z \rangle}{\langle Z_v^2/\tau_Z^2 \rangle} \tag{5.12}$$

which is the ideal outcome of the dynamic model evaluated with Germano averaging in HIT.

Based on this observation, we propose an alternative averaging approach using conditional averaging on $\phi = Z_v/\tau_Z$. Additionally, we restrict

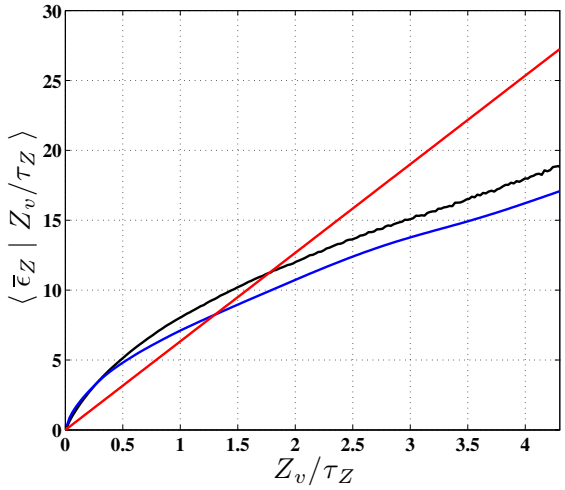

Figure 5.1: Conditional means of subfilter scalar dissipation from 512^3 DNS of homogeneous isotropic turbulence using exact dissipation, Eq. 5.1 (——); least squares linear fit to exact dissipation (——); DSDM plus Eq. 5.13 (——).

the average to those points for which $XY > 0$, i.e. points whose values of X and Y are consistent with a positive value of $\mathcal{C}_\tau$. Only those points which conform to the hypotheses of Eq. 5.6 are thus used to inform the prediction of $\mathcal{C}_\tau$. This conditional averaging approach can be written as

$$\mathcal{C}_\tau(\phi) = \frac{\langle XY | \phi = Z_v/\tau_Z, XY > 0 \rangle}{\langle XX | \phi = Z_v/\tau_Z, XY > 0 \rangle} \tag{5.13}$$

and predicts $\mathcal{C}_\tau$ as a function of $\phi = Z_v/\tau_Z$. A variety of methods exist for computing conditional averages such as those in Eq. 5.13, the simplest probably being the histogram approach in which data are grouped into bins and an average is computed over each bin. Fig. 5.1 shows the results of applying Eq. 5.13 in HIT. The agreement with the conditional mean of the exact dissipation is very good. The conditional coefficient evaluation used 50 bins

spaced at equal intervals in $\log(\phi)$. Regular spacing of the bins speeds and simplifies sorting of the data, while using $\log(\phi)$ rather than ϕ helps to capture the rapid change in the conditional mean dissipation and the long tail of ϕ values with a small number of bins. It was verified that doubling or halving the number of bins had minimal impact on predicted dissipation values. An interpolation scheme was used to account for the rapid variation of $\mathcal{C}_\tau$ over low values of ϕ. For this purpose, the $\mathcal{C}_\tau$ value in each bin is assigned to the mean value of $\log(\phi)$ in that bin and a piecewise cubic hermite interpolating polynomial (pchip) is constructed. The pchip approach is advantageous because it does not produce overshoots and has reduced oscillations for non-smooth data compared to spline interpolation [65].

5.3.2 Sub-Test Filter Modeling

With the conditional averaging approach in place, other aspects of DSDM implementation can be considered. An important issue is the modeling of sub-test filter quantities, especially the test filter level eddy diffusivity D_T^t. A related issue is the appropriate definition of the test filterwidth.

The results in Fig. 5.1 are from tests that sought to characterize the best case performance of the DSDM model. Instead of employing the usual dynamic procedure for estimating the eddy diffusivity model coefficient, the coefficient was determined by a least squares fit of the model

$$D_T = \mathcal{C}_Z \Delta^2 |\overline{S}| \tag{1.11}$$

to the subfilter scalar flux values extracted from the DNS data. This process

was repeated to find D_T^t using the sub-test filter flux. Additionally, the definition of the test filterwidth was modified. Elsewhere in this work, the value $\widehat{\Delta}$, which is the filterwidth of test filtering operation, has been used. Alternatively, we can consider the effective filterwidth of the combined LES and test filtering operations, $\widehat{\widehat{\Delta}}$. We can expect that the greatest impact of the combined filtering operation is on lower wavenumbers, over which the transfer functions of the box and Gaussian filter are close in shape [4]. Therefore, we approximate the effect of the combined filters as that of two Gaussian filtering operations at Δ and $\widehat{\Delta} = 2\Delta$. Writing out the corresponding transfer functions, with k denoting the wavenumber, it is easily seen that

$$\exp\left(-\frac{k^2\Delta^2}{24}\right)\exp\left(-\frac{k^2(2\Delta)^2}{24}\right) = \exp\left(-\frac{k^2\left(\sqrt{5}\Delta\right)^2}{24}\right) \tag{5.14}$$

implying $\widehat{\widehat{\Delta}} = \sqrt{5}\Delta$. This characteristic test filterwidth $\widehat{\widehat{\Delta}}$ replaced $\widehat{\Delta}$ in the definitions of D_T^t and τ_Z^t to obtain the results in Fig. 5.1. It should be recalled from Sec. 4.1 that outside the setting of an a priori test or explicitly filtered LES, the specification of the filterwidth Δ is only approximate. This leads to the viewpoint that the ratio of the test to LES filterwidths is a remaining tunable parameter in dynamic modeling procedures, however the operative test filterwidth is defined.

In an actual simulation, of course, $\mathcal{C}_Z$ must be found without reliance on DNS data and dynamic modeling is the preferred approach. If, at the LES filter level, $D_T = \mathcal{C}_Z\Delta^2|\overline{S}|$ is modeled dynamically [22] by assuming the model coefficient $\mathcal{C}_Z$ is scale invariant, it is then consistent with that assumption to

use $D_T^t = \mathcal{C}_Z \widehat{\Delta}^2 |\widehat{\overline{S}}|$, $\mathcal{C}_Z$ having the same value in both expressions. The magnitude of the strain rate tensor at the test filter level is already required by the dynamic eddy diffusivity modeling procedure, so modeling of D_T^t involves negligible additional expense. The assumption of scale invariance of $\mathcal{C}_Z$ is not particularly valid for the flow used in these apriori tests if we consider the values of $\mathcal{C}_Z$ obtained by least squares fit to DNS values of the subfilter and sub-test filter fluxes. However, when the dynamic model is applied at the LES filterwidth and test filterwidth (requiring a second test filtering operation) the two values of $\mathcal{C}_Z$ obtained show good agreement. Over a range of filterwidths, the two coefficient values differ by ten percent or less. The ratio of the coefficient values is minimally affected by the definition of the test filterwidth as either $\widehat{\Delta} = 2$ or $\widehat{\overline{\Delta}} = \sqrt{5}\Delta$, although the magnitude of the coefficients are reduced using the latter option.

Fig. 5.2 repeats the analysis of Fig. 5.1, except with D_T found using the dynamic model [22] and D_T^t obtained by assuming $\mathcal{C}_Z$ to be scale invariant. The test to LES filterwidth ratio in the dynamic models is defined as 2 in Fig. 5.2(a) and as $\sqrt{5}$ in Fig. 5.2(b). The predicted values of dissipation are higher than those seen in Fig. 5.1. The effect of the test filterwidth definition is most obvious at high values of Z_v/τ_Z, which occur less frequently. It should be noted that the higher modeled dissipation values do not necessarily imply that the variances predicted by the VTE will be too low. Because $\mathcal{C}_Z$ is higher using the dynamic model instead of the fitted value, the modeled production is also higher. The accuracy of the VTE depends on the net source term,

production minus dissipation.

A dynamic modeling approach for D_T is available that assumes scale similarity of $\mathcal{C}_Z$, rather than scale invariance [66]. It predicts both the model coefficient and a scale factor for extrapolation of the coefficient to other filterwidths. This modeling approach was considered for use with the DSDM, but was abandoned because it caused severe underprediction of D_T. It should also be remarked that this modeling approach is significantly more costly than the standard dynamic procedure, because an additional level of test filtering has to be carried out and the roots of a quintic polynomial found at intervals of a few timesteps.

These results suggest that modeling D_T^t using the same model coefficient estimated for D_T is a reasonable response to the sub-test filter modeling problem. It is consistent with other modeling assumptions and does not unduly compromise the accuracy of the dissipation prediction. Adjusting the characteristic test filterwidth to account for the combined effect of the LES and test filtering operations leads to a somewhat better match between the modeled dissipation and the conditional mean of the exact dissipation. However, this modification will not be used in the subsequent analysis to maintain consistency with the results of the previous chapters, in which the test filterwidth was defined as $\widehat{\Delta} = 2\Delta$.

Finally, it is worth re-emphasizing that the quantities needed for computing D_T^t are already available from the dynamic modeling procedure for D_T. Indeed, many of the terms appearing in the DSDM must be computed for the

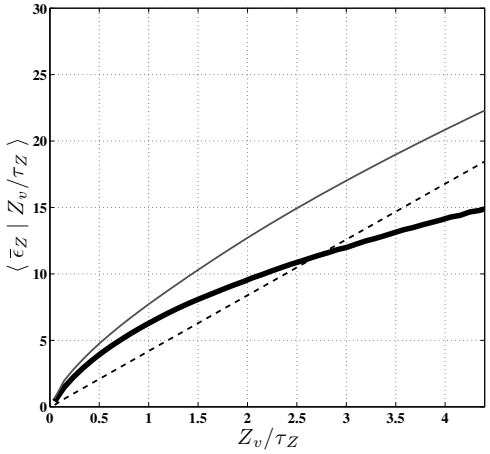

(a)

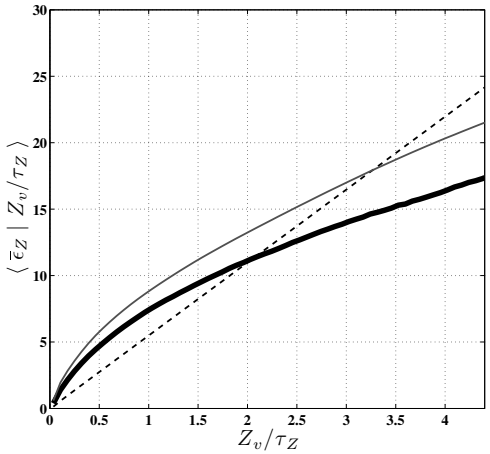

(b)

Figure 5.2: Conditional means of subfilter scalar dissipation from 512^3 DNS of homogeneous isotropic turbulence using exact dissipation, Eq. 5.1 (▬▬); least squares linear fit to exact dissipation (- - - -); DSDM plus Eq. 5.13 (——). Dynamic diffusivity coefficient $\mathcal{C}_Z$ is obtained assuming scale invariance and (**a**) $\widehat{\Delta} = 2\Delta$ (**b**) $\widehat{\overline{\Delta}} = \sqrt{5}\Delta$.

VTE anyway. While the details will depend on the particular code's structure, considerable reuse of quantities required by the VTE or other dynamic modeling procedures should be possible. Additionally, the grouping of terms used in Eq. 5.6 was chosen to highlight their phenomenological characteristics. However, other orderings may be more efficient from a computational standpoint, for example to reduce the number of test filtering operations performed or to limit the number of variables that must be stored. Therefore, while the DSDM is certainly more computationally burdensome than prescription of a single constant $\mathcal{C}_\tau$ value, its evaluation is not as difficult as may first appear from Eq. 5.6.

5.3.3 Temporal Discretization

The appearance of the time derivative term T (Eq. 5.10) is an unusual feature of the DSDM. For greatest compatibility with the discretized VTE, it would seem that the temporal discretization of $\mathcal{L}_v$ should mirror that of Z_v. However, such an approach is not practical for realistic solution methods that may involve multiple sub-iterations and it is desirable to use a simpler method for computing T. Additionally, the results in Figs. 5.1 and 5.2 use a timestep size appropriate for the DNS grid resolution. A larger timestep would typically be employed along with the coarsened LES mesh.

The influence of these factors is investigated in Fig. 5.3. The filterwidth of 16η is about 10 times the DNS grid spacing, so the LES timestep Δt_{LES} can be approximated as 10 times the DNS timestep Δt. The solid curve in

Fig. 5.3 indicates the $\mathcal{C}_\tau$ values obtained when T is set to zero. Clearly, this term cannot be neglected in the estimation of $\mathcal{C}_\tau$. The remaining four curves show the coefficients obtained when T is computed by:

- Case A: Forward Euler, $\Delta t_{\text{LES}} = \Delta t$.
- Case B: Forward Euler, $\Delta t_{\text{LES}} = 10\Delta t$.
- Case C: Forward Euler, $\Delta t_{\text{LES}} = 20\Delta t$.
- Case D: Backward Euler, $\Delta t_{\text{LES}} = 10\Delta t$.

The results show that although T is an important term in the model, the estimated coefficient values are not sensitive to the details of its computation. A backward Euler discretization of T is most straightforward for the majority of simulations. In this approach, T is found from the filtered scalar fields at the previous and current timestep. The other terms of the model, X, P, and F, can be computed from current timestep values. An assumed coefficient must be used for the first timestep. The conditional coefficient evaluation described in Sec. 5.3.1 gives $\mathcal{C}_\tau$ as a function of Z_v/τ_Z. Conceivably, values of $\mathcal{C}_\tau$ could be updated from the interpolating polynomial at each sub-iteration to account for the change in Z_v. However, it should be recalled that the relationship between $\mathcal{C}_\tau$ and Z_v/τ_Z is only an approximation whose level of accuracy does not justify such scrupulous adherence.

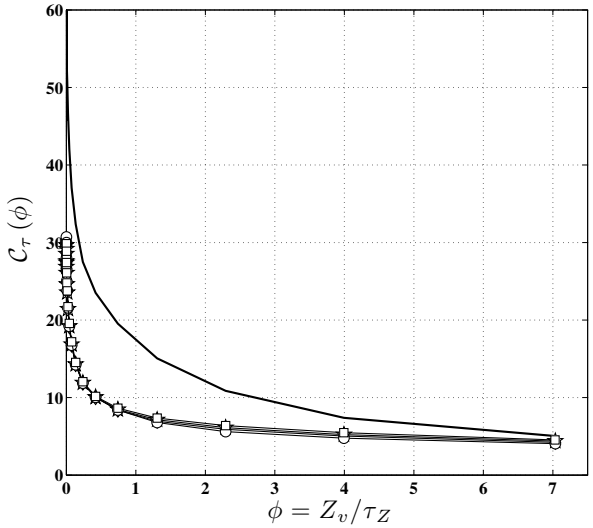

Figure 5.3: Effect of temporal discretization of prediction of $\mathcal{C}_\tau$ using the DSDM: $T = 0$ (———), Case A (star), Case B (diamond), Case C (circle), Case D (square).

5.4 A Posteriori Analysis of Numerical Error in Dynamic Scalar Dissipation Model

In Chapters 2 and 3, algebraic dynamic models for scalar variance were found to be sensitive to three types of numerical error. Numerical errors are encountered in the dynamic procedure for estimating the model coefficient $\mathcal{C}_v$ and in evaluating the gradient-squared quantity which $\mathcal{C}_v$ multiplies. A posteriori analysis revealed that the accumulated numerical error of the filtered scalar field is a third important source of error in the dynamic variance model. Interactions between errors can either magnify or diminish their effects, which can have surprising consequences for the accuracy of variance prediction.

While there are significant differences between the DSDM and algebraic dynamic variance models, these findings indicate that it is important to understand the effects of numerical error on the prediction of subfilter scalar dissipation rate using a dynamic procedure. The coupled DNS-LES method of Chapter 3 was employed for this purpose. Sec. 5.4.1 details the implementation of the model in the coupled DNS-LES algorithm and Sec. 5.4.2 presents the results of the analysis.

5.4.1 Integration of DSDM in the Coupled DNS-LES Method

The most significant modification to the coupled DNS-LES method was made so that the calculation of the time derivative term T of the DSDM could be computed in a manner that was deemed to be most consistent with the temporal discretization of the variance transport equation. Although the

analysis of Sec. 5.3.3 indicates that the model is not especially sensitive to the way in which T is computed, it is reported here for completeness. Other aspects of the method remained as described in Sec. 3.2, and for clarity we describe the procedure for a single filtered scalar field and single variance field. It should be understood that the procedure is repeated for the scalars corresponding to each of the four numerical schemes, which are, as before, spectral, second order central (C2), fourth order central (C4), and sixth order Padé (P6).

The pseudospectral algorithm uses a second order Runge-Kutta (RK2) method for time advancement of the momentum and scalar transport equations. Subfilter models are computed at the beginning of each time step and used for both steps in the RK2 method. Based on these two facts, it was determined to compute the model as

$$\mathcal{C}_\tau^{\mathrm{n}} X^{\mathrm{n}} = F^{\mathrm{n}} + P^{\mathrm{n}} - \frac{\mathcal{L}_v^{\mathrm{n}+1} - \mathcal{L}_v^{\mathrm{n}}}{\Delta t} \tag{5.15}$$

where superscript 'n' indicates a quantity computed at the current time step t^{n} and superscript 'n + 1' indicates a quantity computed after advancing the solution by the DNS timestep Δt to $t^{\mathrm{n}+1}$. This temporal discretization was possible because the filtered scalar evolution has no dependence on the variance model in an incompressible, constant property flow. Therefore, the following algorithm was used:

1. Beginning with all variables advanced to time level t^{n}, compute F^{n}, P^{n}, $\mathcal{L}_v^{\mathrm{n}}$, and X^{n}.

2. Perform first RK step with DNS variables and filtered scalar, bringing them to time $t^{n+1/2}$.

3. Store $\overline{\mathbf{u}}^{n}$ and $\overline{\mathbf{u}}^{n+1/2}$.

4. Perform second RK step with DNS variables and filtered scalar, bringing them to time t^{n+1}.

5. Compute $\mathcal{L}_v^{n+1}$ from $\overline{Z}^{n+1}$.

6. Evaluate DSDM for $\mathcal{C}_\tau(\phi)^{n}$.

7. Interpolate between values of $\mathcal{C}_\tau(\phi)^{n}$ and find $\bar{\epsilon}_Z^{n}$ for local ϕ^{n}.

8. Perform first RK step for variance using stored values of $\overline{\mathbf{u}}^{n}$.

9. Perform second RK step for variance using stored values of $\overline{\mathbf{u}}^{n+1/2}$, advancing variance to t^{n+1}.

Initial results showed that the $\mathcal{C}_\tau(\phi)$ curve varies fairly slowly between timesteps even though the scalar field is decaying and not in statistical steady state . To speed computations, the coefficient was estimated at intervals of 0.01τ, where τ is the eddy turn over time, or every 20 computational time steps. This is roughly equivalent to every fourth timestep for the LES mesh corresponding to the filterwidth used. At intermediate timesteps, the process simplifies to

1. Begin with all variables advanced to time level t^{n}.

2. Perform first RK step with DNS variables and filtered scalar, bringing them to time $t^{n+1/2}$.

3. Store $\overline{\mathbf{u}}^{n}$ and $\overline{\mathbf{u}}^{n+1/2}$.

4. Perform second RK step with DNS variables and filtered scalar, bringing them to time t^{n+1}.

5. Interpolate between last estimated values of $\mathcal{C}_\tau(\phi)$ and find $\overline{\epsilon}_Z^n$ for current local ϕ^n.

6. Perform first RK step for variance using stored values of $\overline{\mathbf{u}}^{n}$.

7. Perform second RK step for variance using stored values of $\overline{\mathbf{u}}^{n+1/2}$, advancing variance to t^{n+1}.

The conditional coefficient evaluation used 10 bins spaced at equal intervals in $\log(\phi)$. Interpolation is performed as described in Sec. 5.3.1.

5.4.2 Results

The results shown are for the same 256^3, $\mathrm{Re}_\lambda = 80$ DNS configuration discussed in Sec. 3.3. The LES filterwidth Δ is equal to 8 times the Kolmogorov scale η.

The mean subfilter variance predictions of the VTE plus DSDM, shown in Fig. 5.4, have two major features. First, all three finite difference schemes predict similar values of $\langle Z_v \rangle$. This is in contrast to results using a constant

value of $\mathcal{C}_\tau$. Fig. 5.6 shows the mean variance values obtained using $\mathcal{C}_\tau = 2$. These results, with $\Delta = 8\eta$, differ quantitatively from the $\mathcal{C}_\tau = 2$ results discussed in Sec. 3.3.3.1, where $\Delta = 16\eta$. Qualitatively, however, they manifest the same effects. In particular, finite difference error in computation of the production term causes lower order schemes to predict lower values of variance. In this flow, the evolution of the filtered scalar is independent of the variance evolution and introduction of the DSDM has no effect on the production model. Therefore, the DSDM must compensate for the differences in production values between the finite difference schemes. Fig. 5.5 confirms this inference. As illustrated by Fig. 5.5(a), the production model (Eq. 1.17) tends to overpredict the mean production relative to the true production term (Eq. 1.16), and the overprediction increases with numerical accuracy. The same trend is shown by the DSDM results for $\langle \overline{\epsilon}_Z \rangle$ in Fig. 5.5(b).

Second, the mean variance predicted by the VTE plus DSDM using spectral numerical accuracy shows overall good agreement with the variance computed from DNS. The accuracy of the model's predictions are best over the initial period of mixing until the subfilter variance reaches its peak around 0.5τ. At that time, the dissipation rate increases relatively more rapidly than the variance, with a small but distinct bump apparent in Fig. 5.5(b), causing the spectral variance to begin to decrease too rapidly. The bump in dissipation values occurs at the average value of the model denominator term X transitions from positive to negative values. For the finite difference schemes, the average value of X remains positive.

Fig. 5.7(a) shows the values of $\mathcal{C}_\tau$ estimated by the DSDM at $t = 0.5\tau$ and $t = 1.1\tau$. At both times, the highest coefficient values are predicted for the P6 scalar evolution. The predicted coefficient values decrease along with the order of finite difference scheme. However, the coefficients predicted for the spectral scalar evolution do not follow this pattern and are most comparable to the coefficients predicted for the C2 scalar evolution. Although the spectral $\mathcal{C}_\tau(\phi)$ curve lies closest to the C2 curve, the values of $\overline{\epsilon}_Z$ predicted are closest to the $P6$ dissipation prediction. This is a reminder that the value of $\overline{\epsilon}_Z$ depends on Z_v and τ_Z as well as $\mathcal{C}_\tau$, and that all three of these quantities are affected by numerical error.

To understand the effects of numerical error on $\mathcal{C}_\tau$, it is helpful to consider each term of the model. This is done here by plotting the conditional mean of each term at 0.5τ. When examining such plots, it should be recalled that low values of Z_v/τ_Z predominate. The conditional means of model terms X (Eq. 5.7) and P (Eq. 5.9) show the same trends whether they are singly conditioned on Z_v/τ_Z or doubly conditioned (as in Eq. 5.13) on Z_v/τ_Z and positive XY. The values of the conditional means are slightly lower in the doubly conditioned case, but qualitatively the plots appear very similar. In contrast, the effects of numerical error on the terms F (Eq. 5.8) and T (Eq. 5.10) are clear only in the doubly conditioned case.

Values of X are lowest for the spectral case and increase as numerical accuracy decreases. Three effects reinforce to create this clear trend in X. First, Sec. 3.3.1 reported that values of $\mathcal{L}_v$ are higher for lower order schemes.

This means that the difference between Z_v and Z_t is greater. Second, the magnitude of the dynamic coefficient $\mathcal{C}_Z$ in the model for D_T increases as numerical accuracy decreases. Also related to the eddy diffusivity model, there is more severe underprediction of the magnitude of the filtered strain rate tensor $|\overline{S}|$ relative to the test filtered strain rate tensor $|\widehat{\overline{S}}|$ as the order of finite difference scheme is decreased.

Like X, P (Fig. 5.8(b)) is lowest for the spectral case. The finite difference results lack a clear trend, but all are higher than the spectral result. Again, finite difference error in the evaluation of the strain rate plays a role, because this increases the difference between D_T^t and D_T. Error in the computation of the magnitudes of the filtered and test filtered scalar gradients is also very important, and was previously discussed in Sec. 3.3.2 in the context of dynamic algebraic variance models. Finite difference methods lead to significant underprediction of gradients, but this is partially compensated for by the error of the filtered scalar evolution. Furthermore, because the test filtered scalar field is smoother than the filtered scalar field, its gradients can be computed with lower numerical error. This increases the difference between the test and filter level production terms. Since spectral methods incur no underprediction of gradients, the difference between the two filter levels is less and P is reduced.

The conditional mean flux term is shown in Fig. 5.9(a). It is positive at low values of Z_v/τ_Z but becomes negative at high values. Thus, the contribution of F tends to increase the value of $\mathcal{C}_\tau$ at low values of Z_v/τ_Z and to

decrease it at high values of Z_v/τ_Z.

The time derivative term T changes sign as the scalar field decays. It is positive at most values of Z_v/τ_Z at earlier times and negative at later times after the variance peaks. At the intermediate stage shown, $\langle T|Z_v/\tau_Z\rangle$ tends to be positive at low Z_v/τ_Z values and negative at high values. However, the conditional means shown in Fig. 5.9(b) are also conditioned on the requirement $XY > 0$. This constraint shifts the conditional mean to negative values because $Y = F + P - T$. A larger shift occurs for the finite difference schemes, because a higher percentage of the X values are positive than for the spectral case. The direct source of numerical error in the term T is the filtered scalar evolution, which determines the evolution of $\mathcal{L}_v$. For the conditional coefficient evaluation, however, the more significant error is that in X because that error partly determines which data points are used in the computation.

5.5 A Priori Analysis of DSDM in a Jet Flow

In this section, the dynamic scalar dissipation model is evaluated through a priori tests on DNS of a piloted planar jet with Reynolds number (based on jet width H and average jet-to-coflow velocity difference) of 6000. The computational domain extends $20H$ in the streamwise direction x, $15H$ in the stream-normal direction y, and $2.56H$ in the periodic spanwise direction z. It is discretized by $768 \times 512 \times 128$ in the x, y, and z directions, respectively. The data was filtered by applying a box filter in each direction with a filterwidth of 8 times the local grid spacing.

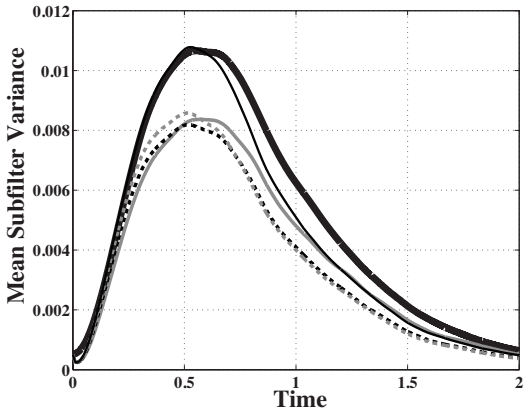

Figure 5.4: Time evolution of mean variance $\langle Z_v \rangle$ for VTE plus DSDM using spectral (——), C2 (——), C4 (▪▪▪▪▪), and P6 (▪▪▪▪▪) schemes compared to exact values from DNS (——).

The focus of this analysis is on the effect of the averaging approach. As in Sec. 5.3.1, the new conditional averaging approach is compared to the conventional Germano averaging approach. In contrast to homogeneous isotropic turbulence, where Germano averaging yields a single coefficient value at each timestep, the planar jet is homogeneous only in the spanwise direction. Therefore, the Germano averaging approach yields $\mathcal{C}_\tau$ as

$$\mathcal{C}_\tau(x,y) = \frac{\langle XY \rangle_z}{\langle XX \rangle_z} \tag{5.16}$$

where $\langle \cdot \rangle_z$ indicates an average taken over the homogeneous z direction of the flow.

Fig. 5.10 shows values of $\mathcal{C}_\tau$ predicted for the planar jet case using Germano averaging, Eq. 5.16. The model coefficient shows rapid fluctuations between high and low values. Points along a spanwise averaging line are sta-

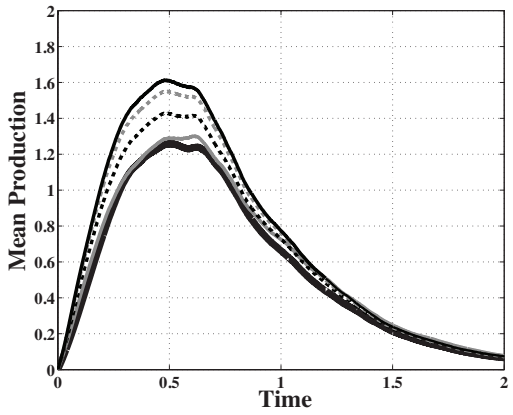

(a)

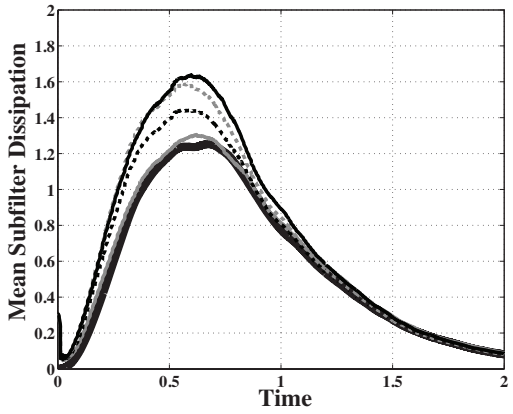

(b)

Figure 5.5: Time evolution of mean quantities (**a**) production (**b**) subfilter dissipation rate for VTE plus DSDM using spectral (———), C2 (———), C4 (▪▪▪▪▪▪), and P6 (▪▪▪▪▪▪) schemes compared to exact values from DNS (———).

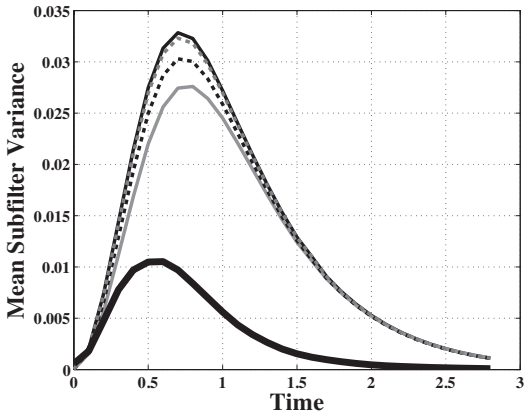

Figure 5.6: Time evolution of mean variance for VTE with constant $\mathcal{C}_\tau = 2$ using spectral (———), C2 (———), C4 (▪▪▪▪▪▪), and P6 (▪▪▪▪▪▪) schemes compared to exact values from DNS (———).

tistically equivalent in the sense of long time averages. At any given time step, however, these points can represent quite different flow conditions as the instantaneous locations of turbulent structures vary. The dynamic dissipation rate model also inherits the fluctuations of the dynamic eddy diffusivity model, whose coefficient $\mathcal{C}_Z$ is obtained using the same kind of spanwise averaging.

The predictions of the dynamic model using Germano averaging are compared to exact $\overline{\epsilon}_Z$ values in Fig. 5.12. While there is some level of qualitative agreement, the dissipation rate is overpredicted near the inflow boundary. Additionally, the structures of the modeled dissipation rate are more fragmentary than those of the exact quantity.

Exact and modeled dissipation values from the same time shown in Fig. 5.12 are plotted as a scatter plot in Fig. 5.13. Symbol size is proportional

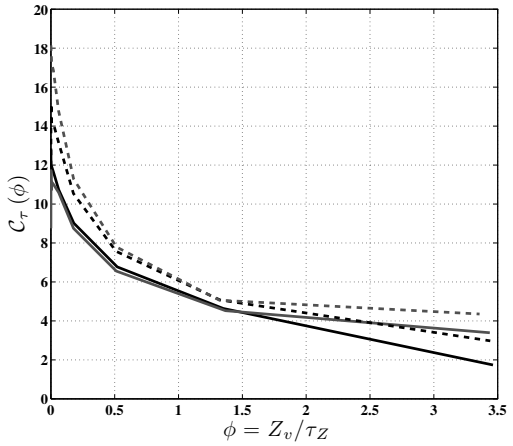

(a)

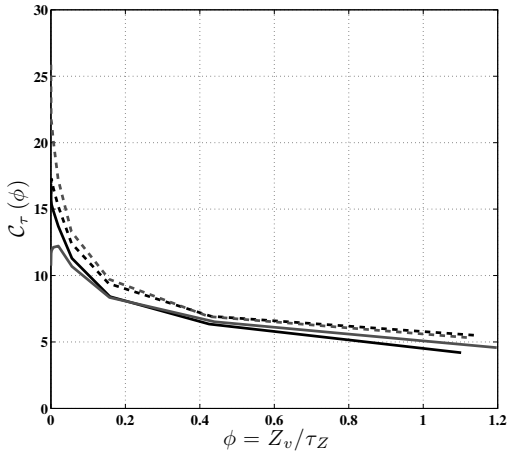

(b)

Figure 5.7: DSDM predictions of $\mathcal{C}_\tau$ for variance evolutions using spectral (——), C2 (——), C4 (▪▪▪▪▪▪), and P6 (▪▪▪▪▪▪) schemes at times (**a**) 0.5τ (**b**) 1.1τ.

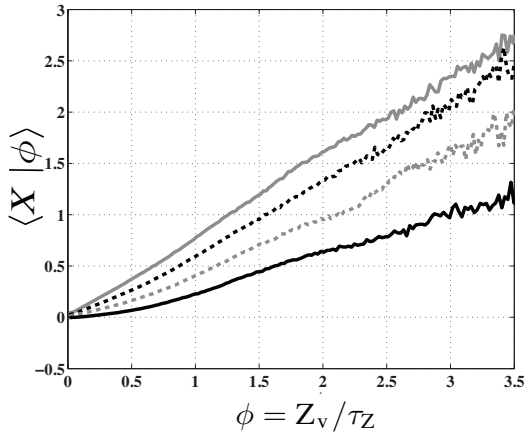

(a)

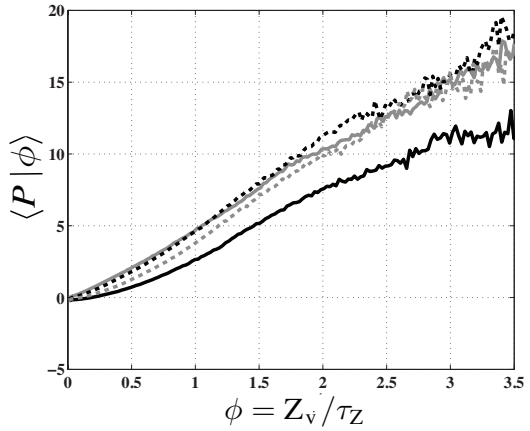

(b)

Figure 5.8: Conditional means, conditioned on $\phi = Z_v/\tau_Z$, of (**a**) X term (**b**) P term of dynamic model for spectral (———), C2 (———), C4 (▪▪▪▪▪▪), and P6 (▪▪▪▪▪▪).

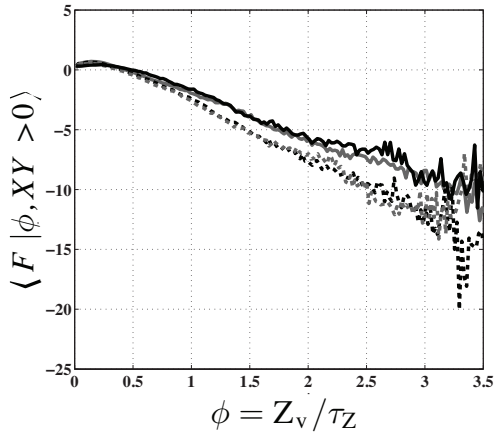

(a)

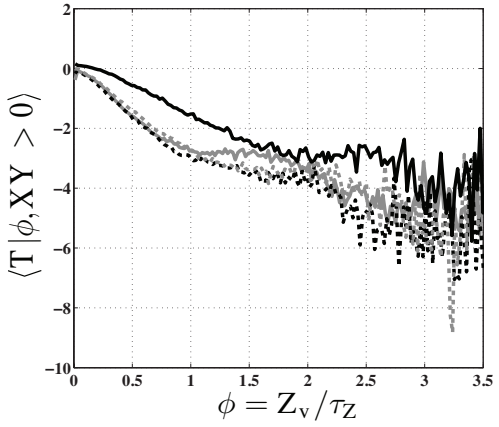

(b)

Figure 5.9: Conditional means, conditioned on $\phi = Z_v/\tau_Z$ and $XY > 0$, of (**a**) F term (**b**) T term of dynamic model (**c**) for spectral (———), C2 (———), C4 (▪▪▪▪▪▪), and P6 (▫▫▫▫▫▫).

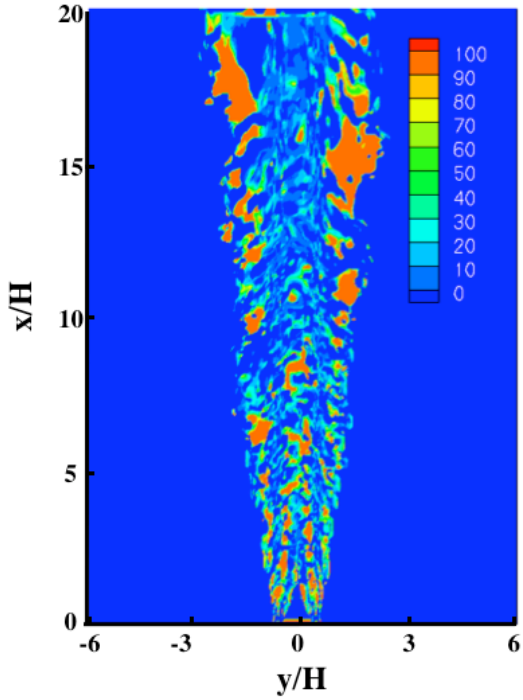

(a)

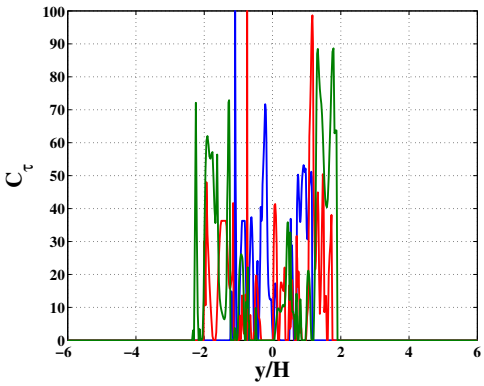

(b)

Figure 5.10: Prediction of $\mathcal{C}_\tau$ using Eq. 5.16. (a) Contours of $\mathcal{C}_\tau$ in xy-plane. (b) Instantaneous profiles of $\mathcal{C}_\tau$ at streamwise locations x/H of 3.33 (——), 6.67 (——), and 13.33 (——).

to the local value of scalar variance. The scatter of exact versus modeled dissipation values using conditional averaging appears more random and lacks an obvious bias. In contrast, the dissipation values predicted using Germano averaging show a strong tendency to be larger than the exact dissipation value. This tendency is manifested across the whole range of scalar variance values, as indicated by the variation in marker size. Such a finding is reasonable, because the model coefficients $\mathcal{C}_\tau$ and $\mathcal{C}_Z$ (which is used in the mixing timescale τ_Z) are determined by averaging along spanwise lines that pass through a range of flow conditions. In contrast, the results using conditional averaging show a stronger relationship between the magnitude of the modeled subfilter scalar dissipation and of the scalar variance.

The conditional averaging approach can be applied to the planar jet configuration, but some reinterpretation is necessary. Because all points in the flow are not statistically equivalent, the notion of a conditional average must be construed somewhat loosely. Conditional averaging could be carried out over homogeneous flow directions only, resulting in $\mathcal{C}_\tau$ values that are explicitly dependent on spatial location as well as on the conditioning variable Z_v/τ_Z. However, this can severely limit the sample size for estimating coefficients. Rather, we argue that it is reasonable for the conditional coefficient calculation to amalgamate points over the entire flow domain, regardless of the flow geometry. A basic principle of LES modeling is that geometry-specific features of the flow are captured by the resolved fields while subfilter scale motions are not directly dependent on the large scales. From this viewpoint, a subfilter

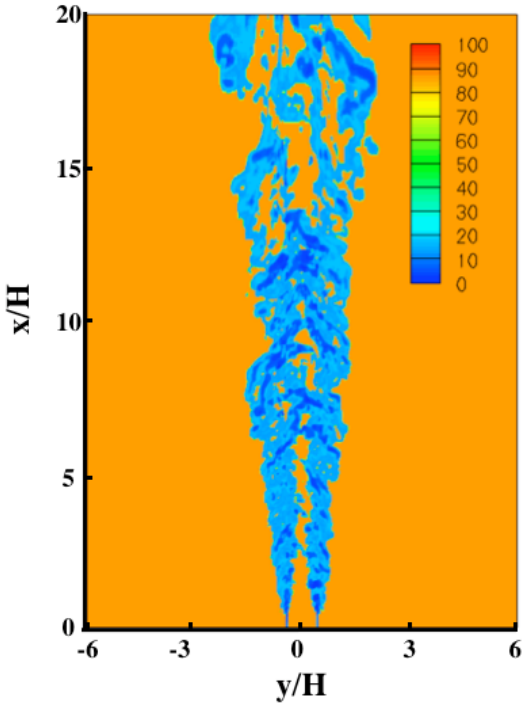

(a)

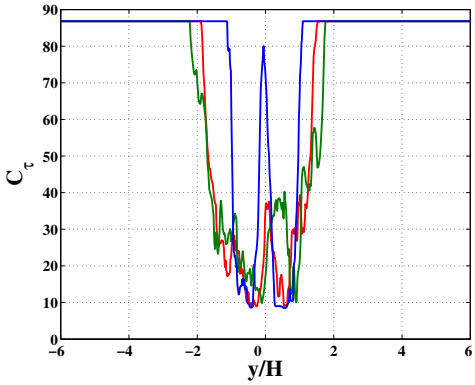

(b)

Figure 5.11: Prediction of $\mathcal{C}_\tau$ using Eq. 5.13. (a) Contours of $\mathcal{C}_\tau$ in a representative xy-plane. (b) Instantaneous profiles of $\mathcal{C}_\tau$ at streamwise locations x/H of 3.33 (——), 6.67 (——), and 13.33 ((——).

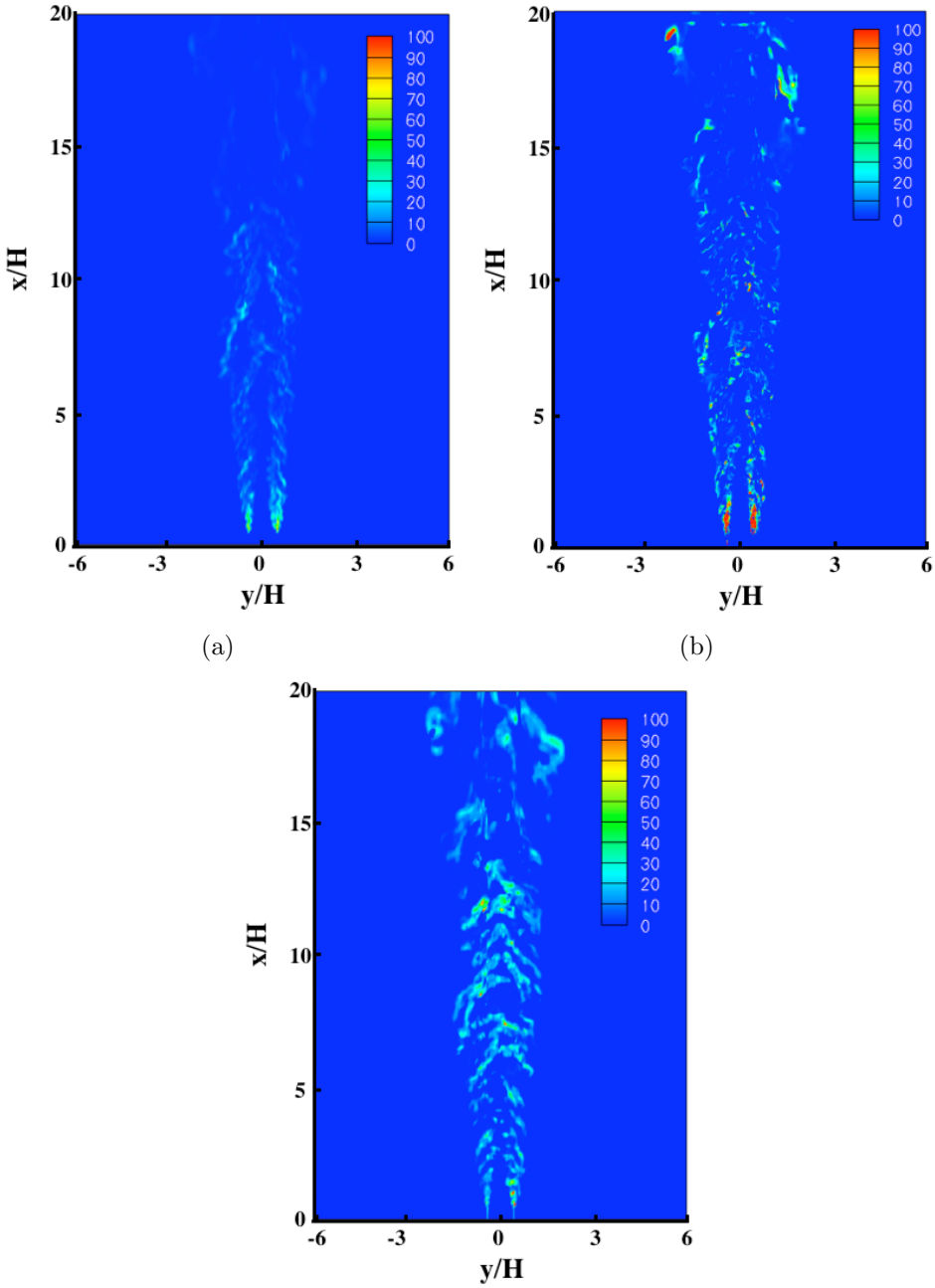

Figure 5.12: Contours of $\overline{\epsilon}_Z$: (**a**) exact, Eq. 5.1 (**b**) dynamic model plus Eq. 5.16 (**c**) dynamic model plus Eq. 5.13.

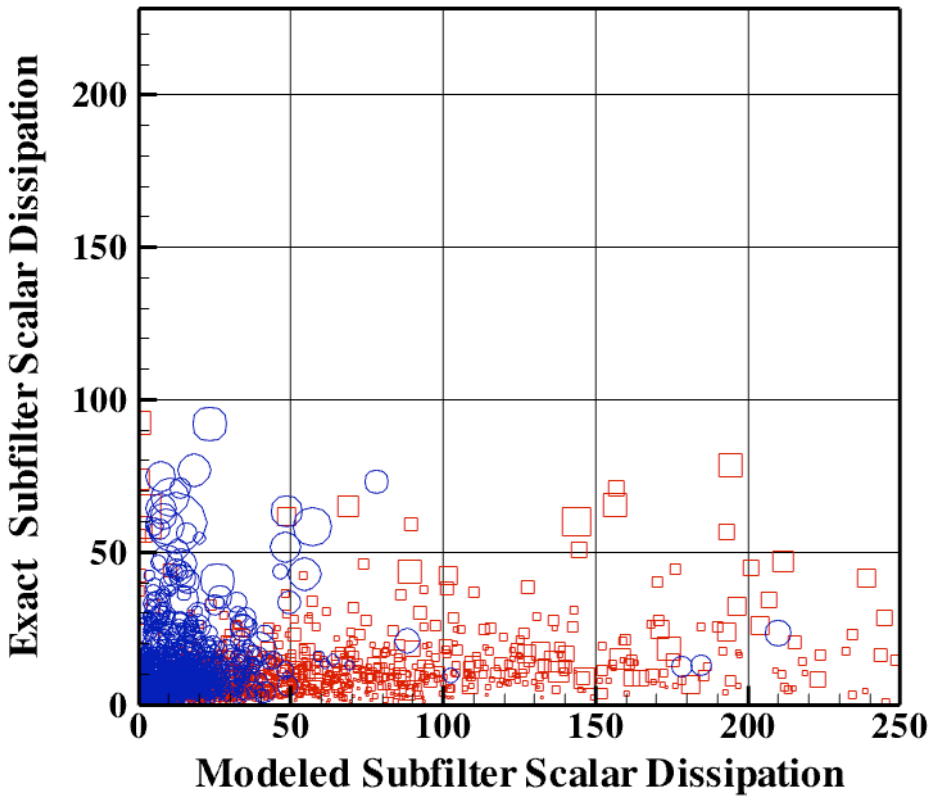

Figure 5.13: Scatter plot of instantaneous values of exact subfilter scalar dissipation versus modeled dissipation using conditional (blue circles) and Germano (red squares) averaging. Symbol size is proportional to the value of Z_v.

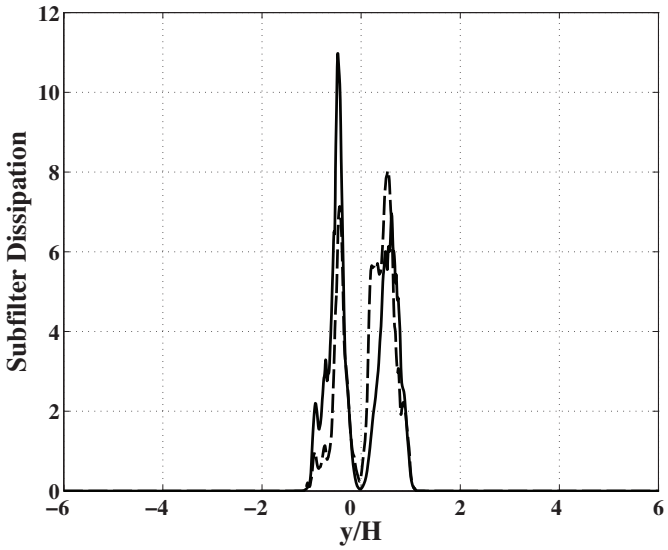

Figure 5.14: Instantaneous profiles of $\bar{\epsilon}_Z$ at streamwise location $x/H = 3.33$: exact dissipation, Eq. 5.1 (———) and dynamic model plus Eq. 5.13 (- - - -).

model coefficient should not require explicit geometrical dependence if local flow conditions are adequately accounted for by the choice of conditioning variable.

Predictions of $\mathcal{C}_\tau$ using Eq. 5.13 are shown in Fig. 5.11. The nonzero coefficient value predicted in laminar regions is an artifact of the binning method, which did not distinguish between very small and zero values of Z_v/τ_Z. However, because Z_v/τ_Z is zero in those areas the model, Eq. 1.19, still properly predicts zero dissipation. Twenty logarithmically spaced bins were used in the computation of $\mathcal{C}_\tau$. The dynamic eddy viscosity coefficient $\mathcal{C}_Z$ was found using a local averaging procedure over test filter volumes. This approach was used to eliminate any effect, even indirect, of averaging over homogeneous directions

from the prediction of $\mathcal{C}_\tau$. As discussed in Sec. 5.3.2, $\mathcal{C}_Z$ is assumed to be the same at test and filter scales. The utility of a conditional averaging method for $\mathcal{C}_Z$ remains open to investigation.

Fig. 5.11 shows the spatial distribution of $\mathcal{C}_\tau$ predicted using conditional averaging, Eq. 5.13. The variation is smoother than that seen in Fig. 5.10 and more clearly related to the turbulent structure of the jet. The subfilter dissipation rate values obtained using this model implementation are plotted in Fig. 5.12. The conditional averaging approach gives a good approximation to the exact dissipation near the jet inflow (Fig. 5.14). Dissipation is overpredicted downstream. However, the accuracy of the dynamic dissipation rate model is contingent on the accuracy of other closures of the VTE, such as the variance production term. In unclosed form, the production term is given by the product of the subfilter scalar flux and the filtered scalar gradient and can be positive or negative. The closed form of the production term, Eq. 1.17, follows from substitution of an eddy diffusion model for the subfilter scalar flux. The production model underpredicts the magnitude of the true production when it is positive and cannot capture regions of negative production. Production modeling errors are actually larger than dissipation modeling errors at these locations. Note that the term P, Eq. 5.9, in the dynamic model is the change in production between the test and filter scales. Therefore, if the model behaves consistently at the two scales it remains possible to predict the value of this difference more accurately than the actual magnitude of production.

5.6 Summary

A dynamic approach for nonequilibrium modeling of subfilter scalar dissipation rate, referred to as the dynamic scalar dissipation model or DSDM, was developed by applying the variance transport equation at two scales. A priori analysis was used to guide model implementation procedures. Particular attention was given to the implications of different averaging procedures for estimation of the model coefficient. Germano averaging over homogeneous flow directions was compared with a novel conditional averaging approach in homogeneous isotropic turbulence and in a planar jet configuration. The choice of averaging procedure had significant impact on dynamic modeling outcomes and affected the spatial patterning of the predicted dissipation fields as well as the magnitude of the modeled dissipation values. In the planar jet case, the conditional averaging approach yielded good agreement with exact dissipation values upstream but showed lower accuracy downstream. However, the dissipation rate modeling errors were smaller than errors in the production term at these locations. Similarly, the best results of the DSDM in HIT were obtained when the eddy diffusivity was estimated directly from the subfilter fluxes. The accuracy decreased when a dynamically modeled eddy diffusivity was substituted.

The effects of numerical error on the model were studied using the coupled DNS-LES method for a posteriori analysis. The results using finite difference methods showed clear trends, with the predicted model coefficients and dissipation values increasing as higher order numerical schemes were used.

The variation in $\overline{\epsilon}_Z$ values among the schemes was largely canceled by the differences in their production values, so the mean variance values of the C2, C4, and P6 evolutions were all quite comparable. This finding highlights the challenges posed by the dual role of the dissipation model as a term of the VTE and as a combustion model parameter. The results of the spectral accuracy scalar evolution fall outside the pattern of the finite difference results because only spectral methods resolve gradients at the smallest filtered flow scales. The spectral variance evolution is the closest match to the DNS variance. This occurs despite the fact that the spectral scheme has the greatest overprediction of the subfilter dissipation compared to the values of $\overline{\epsilon}_Z$ computed from DNS because variance production is similarly overpredicted.

Chapter 6

Conclusions

Errors in the modeling of subfilter scalar variance limit the predictive accuracy of large eddy simulations of turbulent combustion using conserved scalar methods. While LES has already proven itself as a valuable approach to turbulent combustion simulation, it lacks the accuracy needed to reliably and realistically address current issues such as emissions reduction and alternative fuel use. This dissertation presents detailed analysis of numerical and physical errors in variance modeling, develops a novel technique for studying scalar modeling error, applies explicit filtering methods to the LES scalar equations, and proposes a new model for the subfilter scalar dissipation rate. Because this work identifies the key problems in variance modeling and offers solutions to these problems, it makes a clear contribution to the current knowledge and practice of combustion LES.

A priori analysis was used in Chapter 2 to gain initial insight into the effects of numerical error on variance modeling. It was found that some model formulations are more sensitive to numerical error than others and that the interactions of various errors can lead to surprising outcomes. A novel coupled DNS-LES method for a posteriori analysis was used to investigate variance

modeling error more deeply in Chapter 3. This new technique overcomes the limitations of a priori analysis while retaining some of its advantages. Using the coupled DNS-LES method, it was determined that algebraic dynamic models for the variance are highly sensitive to error in the filtered scalar evolution and tend to underpredict the variance. Transport equation models offer more accurate variance prediction, but only if the model coefficient in the subfilter scalar dissipation rate model is specified properly. Numerical error effects were secondary to the dissipation rate modeling issue for transport equation models.

The results of Chapter 3 indicated two main areas that must be addressed to increase variance modeling accuracy. One of these is the numerical error inherent in LES approaches using grid-based filtering. Therefore, explicit filtering was applied to the LES scalar equations in Chapter 4 so that the numerical error of the LES solution could be controlled through grid refinement. The introduction of explicit filtering necessitated some modification of the subfilter model formulations. In particular, a variance transport equation could not be written and only the scalar second moment transport equation remained available as transport equation-based model for the subfilter scalar variance. Numerical convergence of the mean variance prediction was demonstrated for second and fourth order finite difference schemes by increasing the computational mesh resolution for a fixed filterwidth.

The other area of need identified in Chapter 3 is subfilter scalar dissipation rate modeling. A nonequilibrium dynamic scalar dissipation model (DSDM), suitable for use with transport equation models for variance, was

developed in Chapter 5. The accuracy of the new model was found to be enhanced by a novel conditional averaging approach to evaluating the model coefficient in both homogeneous isotropic turbulence and in a planar jet configuration. The DSDM was integrated with the coupled DNS-LES method for a posteriori assessment of its accuracy. The new model was found to compensate for other modeling and numerical errors in the variance evolution so that predicted variance values differed relatively little between implementations using second, fourth, and sixth order accurate finite difference schemes.

Appendices

Appendix A

Appendix A: Quantile-Quantile Plots

A quantile-quantile (q-q) plot compares the inverse cumulative probability density functions of two random variables (say, A and B). The p-th quantile of A, denoted a_p, satisfies

$$a_p = F_A^{-1}(p) \tag{A.1}$$

where F_A^{-1} is the inverse cumulative distribution function of A. Quantile values a_p can be computed exactly if F_A^{-1} is known or determined empirically from data. A q-q plot is a graph of a_p versus b_p for a range of p values between 0 and 1, where b_p are the quantiles of B defined analogously to Eq. A.1.

The form of the q-q plot provides information on how the distributions of A and B differ. Clearly, when A and B have identical distributions, their q-q plot forms a 45 degree line. If the distributions have the same shape but differ in mean (or, more precisely, in location parameter), the q-q plot is translated vertically. Similarly, a difference in variance (scale parameter) rotates the q-q plot. A non-linear q-q plot indicates that the distributions have more general differences in shape.

To make these ideas more definite, Fig. A.1 presents q-q plots formed by sampling from normal and beta distributions. Fig. A.1(c) depicts quantiles of

normal random variables with different combinations of parameters, showing that changes in mean μ cause translation of the q-q plots while changes in variance σ^2 cause rotation. Fig. A.1(d) illustrates that non-linear q-q plots result when the random variables being compared have differently shaped pdfs, even if their parameters are identical.

In the q-q plot figures, the locations of markers indicate the values of particular quantiles. The values of p shown here and throughout this paper are 0.01, 0.025, 0.05, 0.1 to 0.9 in increments of 0.1, 0.95, 0.975, and 0.99.

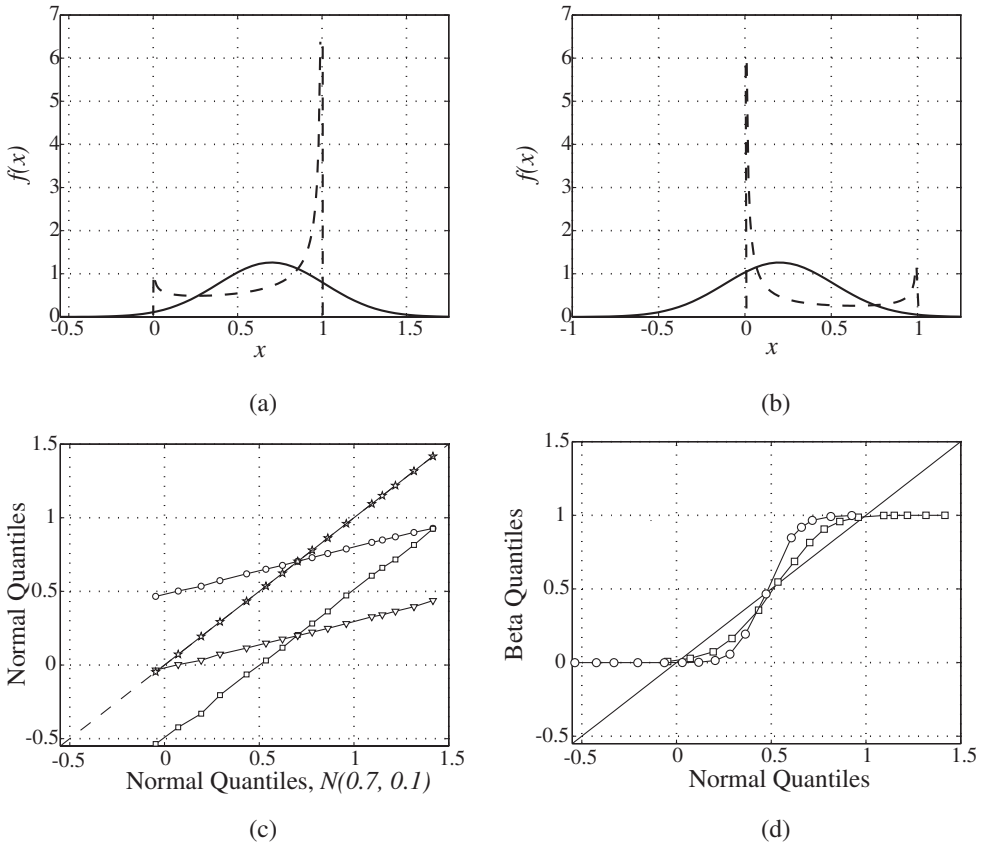

Figure A.1: Analytical pdfs for normal (———) and beta (- - - -) distributions with (**a**) $\mu = 0.7$, $\sigma^2 = 0.1$ and (**b**) $\mu = 0.2$, $\sigma^2 = 0.1$. (**c**) Quantiles of normal variables with parameters (μ, σ^2) of (0.7, 0.1) (star), (0.7, 0.01) (circle), (0.2, 0.1) (square), (0.2, 0.01) (triangle) plotted against (0.7, 0.1) normal quantiles (**d**) Quantiles of beta random variables versus normal random variables with $\mu = 0.7$, $\sigma^2 = 0.1$ (square) and $\mu = 0.2$, $\sigma^2 = 0.1$ (circle).

Appendix B

Appendix B: Filter Weights

Below are listed the filter weights of the discrete commuting filters used in Ch. 4.

$\Delta/h = 2$

$$w_0 = 0.499810627473336, \quad w_{\pm 1} = 0.281547876084500$$
$$w_{\pm 2} = -0.000306166461202, \quad w_{\pm 3} = -0.031147023359966$$

$\Delta/h = 4$

$$w_0 = 0.249587568913233, \quad w_{\pm 1} = 0.218054776930263$$
$$w_{\pm 2} = 0.140721555240010, \quad w_{\pm 3} = 0.056691871791558$$
$$w_{\pm 4} = -0.000116182276671, \quad w_{\pm 5} = -0.019944142404690$$
$$w_{\pm 6} = -0.015321242742068, \quad w_{\pm 7} = -0.004880420995018$$

$\Delta/h = 8$

$$w_0 = 0.125145855967900, \quad w_{\pm1} = 0.121006358306345$$
$$w_{\pm2} = 0.109200952039886, \quad w_{\pm3} = 0.091444459006622$$
$$w_{\pm4} = 0.070210413272970, \quad w_{\pm5} = 0.048252005498249$$
$$w_{\pm6} = 0.028099329476380, \quad w_{\pm7} = 0.011645109052256$$
$$w_{\pm8} = -0.000097723521976, \quad w_{\pm9} = -0.007031323499353$$
$$w_{\pm10} = -0.009818915154734, \quad w_{\pm11} = -0.009602602257042$$
$$w_{\pm12} = -0.007676925202929, \quad w_{\pm13} = -0.005200319063492$$
$$w_{\pm14} = -0.003003745937133$$

$\Delta/h = 16$

$$w_0 = 0.062132158655467, \quad w_{\pm1} = 0.061632477135385$$
$$w_{\pm2} = 0.060151132548449, \quad w_{\pm3} = 0.057740372798194$$
$$w_{\pm4} = 0.054484486775205, \quad w_{\pm5} = 0.050495786611924$$
$$w_{\pm6} = 0.045909308925949, \quad w_{\pm7} = 0.040876535657565$$
$$w_{\pm8} = 0.035558486622899, \quad w_{\pm9} = 0.030118565025776$$
$$w_{\pm10} = 0.024715542364870, \quad w_{\pm11} = 0.019497050551820$$
$$w_{\pm12} = 0.014593908349691, \quad w_{\pm13} = 0.010115549642308$$
$$w_{\pm14} = 0.006146746954403, \quad w_{\pm15} = 0.002745740330027$$
$$w_{\pm16} = -0.000056205114761, \quad w_{\pm17} = -0.002253874123955$$
$$w_{\pm18} = -0.003865946601448, \quad w_{\pm19} = -0.004931815436495$$
$$w_{\pm20} = -0.005507627184806, \quad w_{\pm21} = -0.005661825618649$$
$$w_{\pm22} = -0.005470488354536, \quad w_{\pm23} = -0.005012737874445$$
$$w_{\pm24} = -0.004366481984251, \quad w_{\pm25} = -0.003604697931517$$
$$w_{\pm26} = -0.002792422725497, \quad w_{\pm27} = -0.001984553903736$$
$$w_{\pm28} = -0.001224504518280, \quad w_{\pm29} = -0.000543697785651$$
$$w_{\pm30} = 0.000038165467523, \quad w_{\pm31} = 0.000512176553964$$
$$w_{\pm32} = 0.000878767514340$$

Bibliography

[1] H. Pitsch. Large-eddy simulation of turbulent combustion. *Annual Review of Fluid Mechanics*, 38:453–482, 2006.

[2] R. W. Bilger. Turbulent flows with non-premixed reactants. In *Turbulent Reacting Flows*, pages 65–113. Springer, Berlin, 1980.

[3] A. Leonard. Energy cascade in large eddy simulation of turbulent fluid flow. *Advances in Geophysics*, 18A:237–248, 1974.

[4] S. B. Pope. *Turbulent Flows*. Cambridge University Press, 2000.

[5] J. A. Langford and R. D. Moser. Optimal LES formulations for isotropic turbulence. *Journal of Fluid Mechanics*, 398:321, 1999.

[6] S. B. Pope. Ten questions concerning the large-eddy simulation of turbulent flows. *New Journal of Physics*, 6(35), 2004.

[7] S. B. Pope. Self-conditioned fields for large-eddy simulations of turbulent flows. *Journal of Fluid Mechanics*, 652:139–169, 2010.

[8] A. Moreau, O. Teytaud, and J. P. Bertoglio. Optimal estimation for large-eddy simulation of turbulence and application to the analysis of subgrid models. *Physics of fluids*, 18:105101, 2006.

[9] G. Balarac, H. Pitsch, and V. Raman. Development of a dynamic model for the subfilter scalar variance using the concept of optimal estimators. *Physics of Fluids*, 20:035114, 2008.

[10] G. Balarac, H. Pitsch, and V. Raman. Modeling of the subfilter scalar dissipation rate using the concept of optimal estimators. *Physics of Fluids*, 20:091701, 2008.

[11] R. Deutsch. *Estimation Theory*. Prentice-Hall, 1965.

[12] S. Ghosal. An analysis of numerical errors in large-eddy simulations of turbulence. *Journal of Computational Physics*, 125(1):187–206, 1996.

[13] A. G. Kravchenko and P. Moin. On the effect of numerical errors in large eddy simulations of turbulent flows. *Journal of Computational Physics*, 131:310–322, 1997.

[14] F. K. Chow and P. Moin. A further study of numerical errors in large-eddy simulations. *Journal of Computational Physics*, 184:366–380, 2003.

[15] P. Moin. *Fundamentals of engineering numerical analysis*. Cambridge University Press, 2001.

[16] R. W. Bilger. The structure of diffusion flames. *Combustion Science and Technology*, 13:155–170, 1976.

[17] N. Peters. *Turbulent Combustion*. Cambridge University Press, 2000.

[18] R. W. Bilger. Turbulent diffusion flames. *Annual Reviews of Fluid Mechanics*, 21:101–135, 1989.

[19] P. Sripakagorn, S. Mitarai, G. Kosály, and H. Pitsch. Extinction and reignition in a diffusion flame: a direct numerical simulation study. *Journal of Fluid Mechanics*, 518:231–259, 2004.

[20] N. Peters. Local quenching due to flame stretch and nonpremixed turbulent combustion. *Combustion Science and Technology*, 30:1–17, 1983.

[21] N. Peters. Laminar diffusion flamelet models in non-premixed turbulent combustion. *Progress in Energy and Combustion Science*, 10:319–339, 1984.

[22] P. Moin, K. Squires, W. Cabot, and S. Lee. A dynamic subgrid-scale model for compressible turbulence and scalar transport. *Physics of Fluids A*, 3:2746–2757, 1991.

[23] S. B. Pope. Computations of turbulent combustion: Progress and challenges. In *Proceedings of the 23rd Symposium (International) on Combustion*, pages 591–612. The Combustion Institute, Pittsburgh, 1990.

[24] C. Jimenez, F. Ducros, B. Cuenot, and B. Bedat. Subgrid scale variance and dissipation of a scalar field in large eddy simulations. *Physics of Fluids*, 13:1748, 2001.

[25] A. W. Cook, J. J. Riley, and G. Kosály. A laminar flamelet approach to subgrid-scale chemistry in turbulent flows. *Combustion and Flame*, 109:332–341, 1997.

[26] H. Pitsch. Improved pollutant predictions in large-eddy simulations of turbulent non-premixed combustion by considering scalar dissipation rate fluctuations. *Proceedings of the Combustion Institute*, 29:1971–1978, 2002.

[27] C. Tong. Measurements of conserved scalar filtered density function in a turbulent jet. *Physics of Fluids*, 13:2923–2937, 2001.

[28] C. Wall, B. J. Boersma, and P. Moin. An evaluation of the assumed beta probability density function subgrid-scale model for large eddy simulation of nonpremixed, turbulent combustion with heat release. *Physics of Fluids*, 12(10):2522–2529, 2000.

[29] V. Raman and H. Pitsch. Large-eddy simulation of bluff-body stabilized non-premixed flame using a recursive-refinement procedure. *Combustion and Flame*, 142(4):329–347, 2005.

[30] A. W. Cook and J. J. Riley. A subgrid model for equilibrium chemistry in turbulent flows. *Physics of Fluids*, 6:2868–2870, 1994.

[31] A. W. Cook and J. J. Riley. Subgrid-scale modeling for turbulent reacting flows. *Combustion and Flame*, 112:593–606, 1998.

[32] S. M. de Bruyn Kops, J. J. Riley, G. Kosály, and A. W. Cook. Investigation of modeling for non-premixed turbulent combustion. *Flow, Turbulence and Combustion*, 60:105–122, 1998.

[33] P. E. DesJardin and S. H. Frankel. Large eddy simulation of a non-premixed reacting jet: Application and assessment of subgrid-scale combustion models. *Physics of Fluids*, 10:2298–2314, 1998.

[34] C. D. Pierce and P. Moin. A dynamic model for subgrid-scale variance and dissipation rate of a conserved scalar. *Physics of Fluids*, 10:3041–3044, 1998.

[35] P. J. Colucci, F. A. Jaberi, and P. Givi. Filtered density function for large eddy simulation of turbulent reacting flows. *Physics of Fluids*, 10(2):499–515, 1998.

[36] F. A. Jaberi, P. J. Colucci, S. James, P. Givi, and S. B. Pope. Filtered mass density function for large-eddy simulation of turbulent reacting flows. *Journal of Fluid Mechanics*, 401:85–121, 1999.

[37] V. Raman and H. Pitsch. A consistent LES/filtered-density function formulation for the simulation of turbulent flames with detailed chemistry. *Proceedings of the Combustion Institute*, 31:1711–1719, 2006.

[38] M. Germano, U. Piomelli, P. Moin, and W. H. Cabot. A dynamic subgrid-scale eddy viscosity model. *Physics of Fluids*, 7:1760–1765, 1991.

[39] C. M. Kaul, V. Raman, G. Balarac, and H. Pitsch. Numerical errors in the computation of subfilter scalar variance in large eddy simulations. *Physics of Fluids*, 21:055102, 2009.

[40] N. A. C. Cressie. *Statistics for Spatial Data*. John Wiley & Sons, Inc., New York, 1993.

[41] C. M. Kaul and V. Raman. A posteriori analysis of numerical errors in subfilter scalar variance modeling for large eddy simulation. *Physics of Fluids*, 23(3):035102, 2011.

[42] J. Jimenez, A. Linan, M. M. Rogers, and F. J. Higuera. *A priori* testing of subgrid models for chemically reacting non-premixed turbulent flows. *Journal of Fluid Mechanics*, 349:149–171, 1997.

[43] J. P. Mellado, S. Sarkar, and C. Pantano. Reconstruction subgrid models for nonpremixed combustion. *Physics of Fluids*, 15(11):3280–3307, November 2003.

[44] V. Eswaran and S. B. Pope. Direct numerical simulations of the turbulent mixing of a passive scalar. *The Physics of Fluids*, 31:506–520, 1988.

[45] M. M. Rogers and R. D. Moser. Direct numerical simulation of a self-similar turbulent mixing layer. *Physics of Fluids*, 6:903–923, 1994.

[46] K. Alvelius. Random forcing of three-dimensional homogeneous turbulence. *Physics of Fluids*, 11(7):1880–1889, 1999.

[47] R. A. Clark, J. H. Ferziger, and W. C. Reynolds. Evaluation of subgrid-scale models using an accurately simulated turbulent flow. *Journal of Fluid Mechanics*, 91(1):1–16, 1979.

[48] R. J. Adrian. Stochastic estimation of sub-grid scale motions. *Applied Mechanics Reviews*, 43:214–218, 1990.

[49] M. Herrmann, G. Blanquart, and V. Raman. A bounded quick scheme for preserving scalar bounds in large-eddy simulations. *AIAA Journal*, 44(12):2879–2880, 2006.

[50] S. Ghosal and P. Moin. The basic equations for the les of turbulent flows in complex geometry. *Journal of Computational Physics*, 118:24–37, 1995.

[51] R. S. Rogallo and P. Moin. Numerical simulation of turbulent flows. *Annual Reviews of Fluid Mechanics*, 16:99–137, 1984.

[52] O. V. Vasilyev, T. S. Lund, and P. Moin. A general class of commutative filters for les in complex geometries. *Journal of Computational Physics*, 146(1):82–104, 1998.

[53] T. S. Lund. The use of explicit filters in large eddy simulation. *Computers and Mathematics with Applications*, 46(4):603–616, 2003.

[54] G. S. Jiang and C. W. Shu. Efficient implementation of weighted eno schemes. *Journal of Computational Physics*, 126:202–228, 1996.

[55] S. T. Bose, P. Moin, and D. You. Grid-independent large-eddy simulation using explicit filtering. *Physics of Fluids*, 22(10):105103, 2010.

[56] D. Carati, G. S. Winckelmans, and H. Jeanmart. On the modelling of the subgrid-scale and filtered-scale stress tensors in large-eddy simulation. *Journal of Fluid Mechanics*, 441:119–138, 2001.

[57] S. Stolz and N. A. Adams. An approximate deconvolution procedure for large-eddy simulation. *Physics of Fluids*, 11:1699–1701, 1999.

[58] M. Frigo and S. G. Johnson. The design and implementation of fftw3. *Proceedings of the IEEE*, 93(2):216–231, 2005.

[59] S. S. Girimaji and Y. Zhou. Analysis and modeling of subgrid scalar mixing using numerical data. *Physics of Fluids*, 8:1224–1236, 1996.

[60] R. O. Fox. *Computational Models for Turbulent Reacting Flows*. Cambridge University Press, 2003.

[61] C. Pera, J. Reveillon, L. Vervisch, and P. Domingo. Modeling subgrid scale mixture fraction variance in les of evaporating spray. *Combustion and Flame*, 146:635–648, 2006.

[62] S. Chumakov and C. J. Rutland. Dynamic structure models for scalar flux and dissipation in large eddy simulation. *AIAA Journal*, 42:1132–1138, 2004.

[63] S. Ghosal, T. S. Lund, P. Moin, and K. Akselvoll. A dynamic localization model for large-eddy simulation of turbulent flows. *Journal of Fluid Mechanics*, 286:229–255, 1995.

[64] D. K. Lilly. A proposed modification of the Germano subgrid-scale closure method. *Physics of Fluids A*, 4:633–635, 1992.

[65] F. N. Fritsch and R. E. Carlson. Monotone piecewise cubic interpolation. *SIAM Journal on Numerical Analysis*, 17(2):238–246, 1980.

[66] F. Porté-Agel, C. Meneveau, and M. B. Parlange. Scale-dependent dynamic model for large-eddy simulation: application to a neutral atmospheric boundary layer. *Journal of Fluid Mechanics*, 415:261–284, 2000.